STUDIES ON THE STRUCTURE AND INTERACTIONS OF SYNAPTOTAGMIN-1 AND SNARE PROTEINS IN NEUROTRANSMITTER RELEASE

APPROVED BY SUPERVISORY COMMITTEE

Josep Rizo, Ph.D., Advisor

Michael Rosen, Ph.D., Committee Chair

Hongtao Yu, Ph.D.

Youxing Jiang, Ph.D.

DEDICATION

This work is dedicated to Daniel John Brewer, Judy Carol Freeze Brewer, Josep Rizo, and Wen-Huang Ko, who selflessly gave their time and energy without reserve.

STUDIES ON THE STRUCTURE AND INTERACTIONS OF SYNAPTOTAGMIN-1 AND SNARE PROTEINS IN NEUROTRANSMITTER RELEASE

by

KYLE DANIEL BREWER

DISSERTATION

Presented to the Faculty of the Graduate School of Biomedical Sciences

The University of Texas Southwestern Medical Center at Dallas

In Partial Fulfillment of the Requirements

For the Degree of

DOCTOR OF PHILOSOPHY

The University of Texas Southwestern Medical Center at Dallas

Dallas, Texas

December, 2014

STUDIES ON THE STRUCTURE AND INTERACTIONS OF SYNAPTOTAGMIN-1 AND SNARE PROTEINS IN NEUROTRANSMITTER RELEASE

Publication No. _____

Kyle Daniel Brewer, Ph.D.

The University of Texas Southwestern Medical Center at Dallas, Graduation Year

Supervising Professor: Josep Rizo, Ph.D.

The SNARE complex and synaptotagmin-1 are essential for Ca^{2+}-evoked neurotransmitter release, yet the mechanism of how these proteins work together in membrane fusion is unclear. Dozens of studies performed over two decades have described different types of synaptotagmin-1/SNARE interactions and reported the individual structures of the SNAREs, the SNARE complex, and the C_2 domains that form most of the cytoplasmic region of synaptotagmin-1.

However, a high-resolution structure of a synaptotagmin-1/SNARE complex, which is crucial to understand the mechanism of release, has not been reported. In this work, we explore methods to examine the biophysical properties of synaptotagmin-1 and the SNAREs, primarily using NMR. We first examine the conformation of synaptobrevin on nanodisc bilayers and find that that the N-terminal portion of the SNARE domain has a high propensity to remain unfolded on membranes. We next look at the conformation of synaptotagmin-1 on nanodiscs and demonstrate that although both C_2 domains primarily bind to the same membrane, a small population of antiparallel conformers also exist. Finally and most importantly, we look at the structure of synaptotagmin-1/SNARE complex. After overcoming many obstacles and failed approaches, we were able to obtain intermolecular restraints for this 66 kDa machinery by introducing lanthanide tags for measurement of pseudocontact shifts (PCSs). Computational analyses incorporating these restraints show that a static structure cannot fully explain all the PCS measurements, but the data can be fit with a dynamic ensemble of structures whereby a polybasic region of the synaptotagmin-1 C_2B domain binds to a polyacidic region formed by the syntaxin-1 and SNAP-25 SNARE motifs. The orientation of the synaptotagmin-1 C_2B domain with respect to the SNARE complex within the ensemble is expected to allow quick, simultaneous interaction with lipids on both membranes upon Ca^{2+} binding to bring the membranes together. Distinct mutations in the C_2B domain polybasic region caused differential disruptions of SNARE complex-binding that correlate with the impairment of neurotransmitter release caused by these mutations. Overall, these results and the architecture of the synaptagmin-1/SNARE complex revealed by our NMR data support the hypothesis that synaptotagmin-1 cooperates with the SNAREs by bringing membranes together to trigger fast fusion upon Ca^{2+} influx.

TABLE OF CONTENTS

PRIOR PUBLICATIONS

Brewer, K.D., Li, W., Horne, B.E., and Rizo, J. (2011). Reluctance to membrane binding enables accessibility of the synaptobrevin SNARE motif for SNARE complex formation. Proc Natl Acad Sci U S A *108*, 12723-12728.

Zhou, A., Brewer, K.D., and Rizo, J. (2013). Analysis of SNARE complex/synaptotagmin-1 interactions by one-dimensional NMR spectroscopy. Biochemistry *52*, 3446-3456.

Seven, A.B., Brewer, K.D., Shi, L., Jiang, Q.X., and Rizo, J. (2013). Prevalent mechanism of membrane bridging by synaptotagmin-1. Proc Natl Acad Sci U S A *110*, E3243-3252.

Xu, J., Brewer, K.D., Perez-Castillejos, R., and Rizo, J. (2013). Subtle Interplay between synaptotagmin and complexin binding to the SNARE complex. J Mol Biol *425*, 3461-3475.

LIST OF FIGURES

Chapter 1 General Introduction

1.1 The Synaptic Vesicle Cycle

The neuron is the fundamental unit of information processing in the brain (Figure 1.1). The human brain is composed of approximately 100 billion neurons (Azevedo et al., 2009; Herculano-Houzel, 2012), most making >500 synaptic connections (Sudhof, 2004). With this degree of complexity, precise regulation of the network is necessary, which largely takes place in the synapse where the control of communication between neurons is managed. The communication at the synapse between neurons is governed by the fusion of synaptic vesicles to release neurotransmitters into the synaptic cleft.

Synaptic vesicles are formed through budding from the early endosome [(Sudhof, 2004); Figure 1.2A], and neurotransmitters are loaded into synaptic vesicles with transporters activated by an electrochemical gradient created in the vesicle via a proton ATPase (Fykse and Fonnum, 1996; Stadler and Tsukita, 1984). The vesicles then dock at the active zone of the synapse where neurotransmitters are released into the synaptic cleft (Satzler et al., 2002; Schikorski and Stevens, 2001). After docking, the vesicles are primed for fusion by an ATP dependent process (Klenchin and Martin, 2000), and upon an action potential reaching the terminal synapse in a neuron, voltage-gated calcium channels open, allowing the influx of calcium into the presynaptic terminal (Catterall, 2011; Dietrich et al., 2003). Calcium influx triggers membrane fusion, occurring on a short time scale from 100 microseconds to 1 millisecond after the arrival of the action potential (Meinrenken et al., 2002; Sabatini and Regehr, 1996).

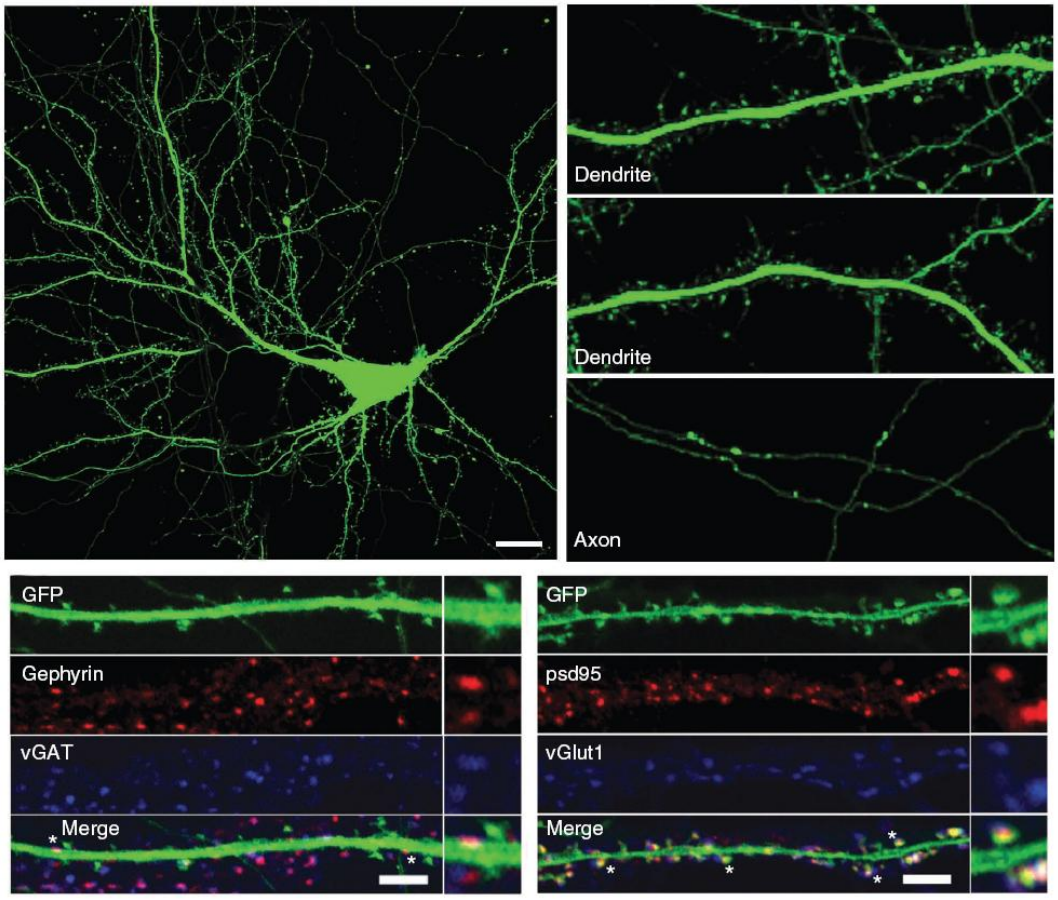

Figure 1.1 Morphology of a neuron. A pyramidal neuron from the hippocampus is shown illuminated with GFP. Axons (thinner lines) and dendrites (thicker lines) with dendritic spines are clearly visible. Top scale bar: 20 µm. vGAT and vGlut1 (blue) label inhibitory and excitatory presynapses, respectively. Gephyrin and psd95 (red) label inhibitory and excitatory postsynapses, respectively. Bottom scale bars: 5 µm. Asterisks (*) mark synapses on dendritic shafts (left) and spine heads (right), showing inhibitory and excitatory synapses have distinguishing morphology (Beaudoin et al., 2012).

Neurotransmitters are released into the synaptic cleft and diffuse across a 20 nanometer distance to postsynaptic receptors that bind to the neurotransmitters (Ribrault et al., 2011), modulating the activity of the postsynaptic neuron. After fusion, synaptic vesicles are recycled back into the neuron via endocytosis (Galli and Haucke, 2004; Slepnev and De Camilli, 2000). The synaptic vesicles are either reloaded with neurotramistters or fuse back into the early endosome (Sudhof, 2004).

The membrane fusion step itself can be divided into several substeps (Figure 1.2B). To begin membrane fusion, a synaptic vesicle and the presynaptic plasma membrane must be positioned close in space to each other. As membrane fusion requires large amounts of energy, the membranes coming into proximity is not enough to drive the process (Chernomordik and Kozlov, 2003; Cohen and Melikyan, 2004). The apposed membranes are first perturbed to form "nipples" where the membranes buckle toward each other (Kuzmin et al., 2001; Rizo et al., 2006), and the proximal leaflets of the membranes fuse into a stalk intermediate. The distal leaflets can then form a flat bilayer in a state called hemifusion that has been observed as a stable intermediate in some studies (Lu et al., 2005; Xu et al., 2011; Yoon et al., 2006), although this state has also been hypothesized to be a dead end for fusion. The distal leaflets fully fuse to form a fusion pore and then expand further either after hemifusion or directly from the stalk intermediate.

A

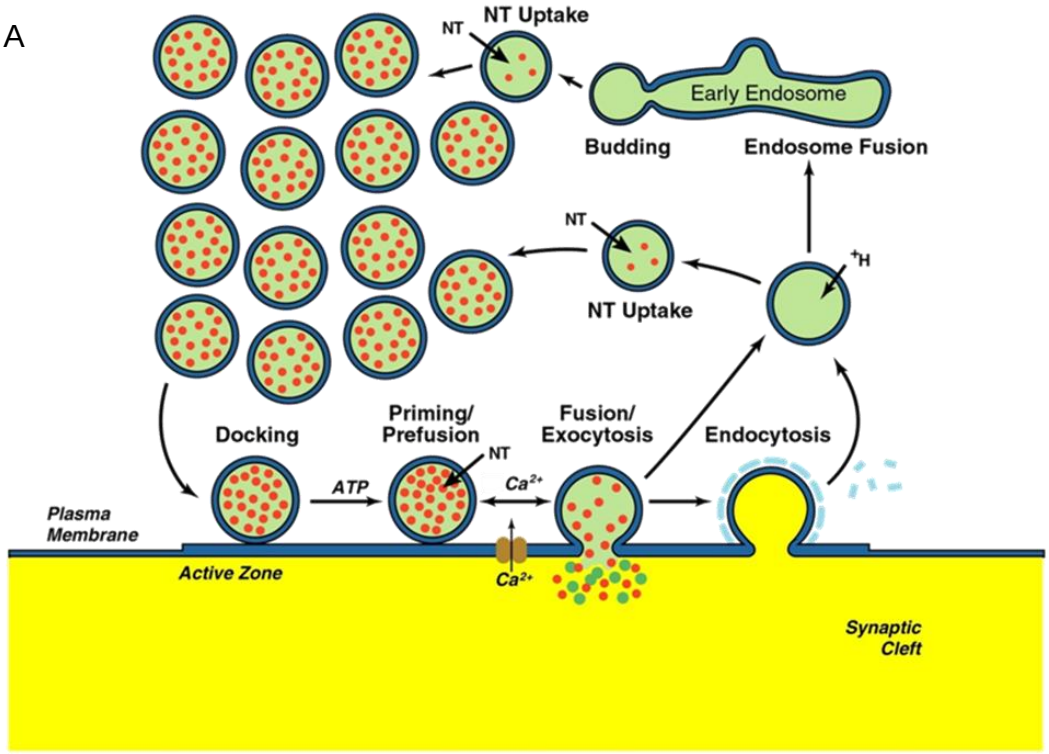
NT
NT Uptake
Early Endosome
Budding
Endosome Fusion
NT
NT Uptake
+H
Docking
Priming/
Prefusion
Fusion/
Exocytosis
Endocytosis
NT
ATP
Ca2+
Plasma
Membrane
Active Zone
Ca2+
Synaptic
Cleft

B

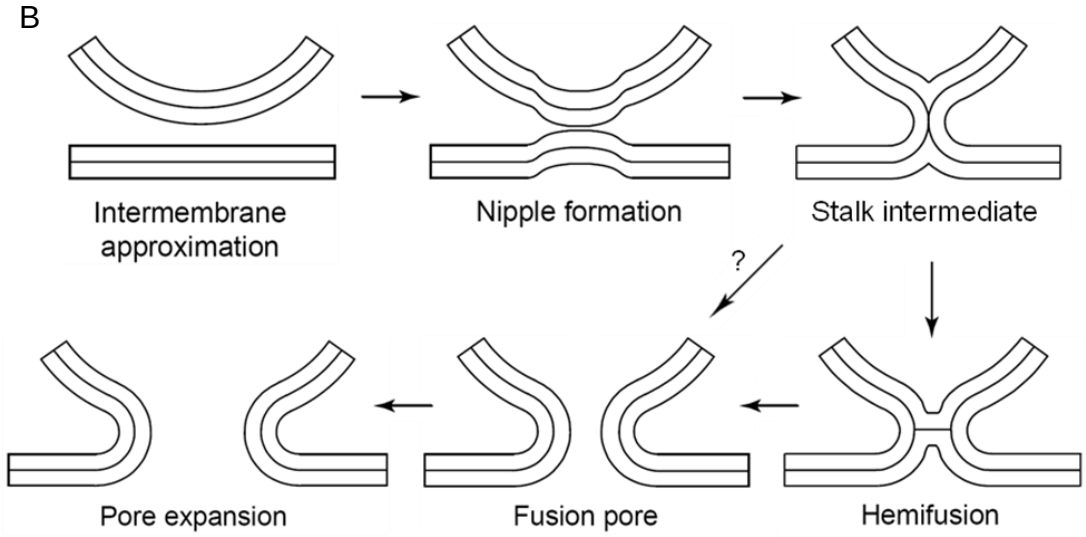
Intermembrane
approximation
Nipple formation
Stalk intermediate
?
Pore expansion
Fusion pore
Hemifusion

Figure 1.2 The synaptic vesicle cycle and membrane fusion. (A) Synaptic vesicles bud from the early endosome and take up neurotransmitters. Vesicles from the synaptic vesicle pool dock at the active zone of the synapse, prime for release, and exocytose upon Ca^{2+} influx. The fused vesicles then endocytose and either are refilled for another round of fusion or return to the endosome (Sudhof, 2004). (B) Upon perturbation, membranes in close approximation create a nipple leading to the formation of a stalk to merge the outer leaflets. The membranes may then enter a metastable state of hemifusion or proceed forward towards full fusion and pore expansion (Rizo et al., 2006).

1.2 Calcium Triggered Neurotransmitter Release

In neurons, tight control of synaptic vesicle exocytosis is necessary to ensure that communication between neurons occurs correctly. Main concerns in the regulation of this process include preventing aberrant neurotransmitter release, ensuring fast release upon signaling from the action potential, and maintaining the synaptic vesicle pool primed for release before stimulation (Sudhof, 2004). The ten thousand fold difference between intracellular and extracellular calcium concentrations allow these factors to be precisely regulated through calcium triggering of neurotransmitter release, especially because the concentration of intracellular calcium is tightly controlled (Thayer et al., 2002).

Upon the firing of an action potential, voltage gated calcium channels are opened, allowing the extracellular calcium to enter a neuron (Catterall, 2011; Dietrich et al., 2003). These channels are linked via protein-protein interactions to the precise site of membrane fusion so that the local concentration of calcium is high enough to trigger fusion (Sheng et al., 1994). This precise localization allows calcium triggering to occur rapidly and to minimize changes to the overall calcium ion concentration within the neuron so that other cellular processes are not disturbed.

1.2.1 SNAREs

Many proteins are necessary for intercellular neuron communication. Central among these proteins are the soluble SNAREs (soluble N-ethylmaleimide sensitive factor attachment protein receptors). The SNAREs include the proteins synaptobrevin,

syntaxin, and SNAP-25 [(Rizo and Rosenmund, 2008); Figure 1.3]. Synaptobrevin and syntaxin both have a single SNARE motif and are localized to synaptic vesicles and the plasma membrane, respectively, through a C-terminal transmembrane domain. Syntaxin also contains an N-terminal H_{ABC} domain that can form a four helix bundle with the SNARE motif to inhibit SNARE complex formation. SNAP-25 has N- and C-terminal SNARE motifs and is attached to the plasma membrane by four palmitoylated cysteines in the long linker region in between them.

The SNARE motifs are unfolded in solution, but can associate with each other to form a tight four-helix bundle heterotetramer that can bring the vesicle and plasma membrane together [(Poirier et al., 1998; Sutton et al., 1998) Figure 1.4A]. The complex begins forming from the distal N-termini of all SNARE domains, which zipper towards the C-termini. After formation of the SNARE complex *in vitro*, it requires SDS-containing buffer at temperatures of 90°C to be disassembled (Fasshauer et al., 1997), demonstrating the high stability of the complex. The SNARE complex is hypothesized to zipper only partially prior to fusion, with synaptobrevin remaining unassembled in the SNARE domain C-terminus (Gao et al., 2012). This partial assembly is maintained by various protein factors to inhibit fusion while still allowing fusion to occur quickly upon calcium triggering since coil to helix transitions can occur on a nanosecond timescale. During fusion, the SNARE complex may zipper past the SNARE domains with the juxtamembrane and transmembrane regions of synaptobrevin and syntaxin forming a two-helix bundle that extends into the fully fused membranes (Stein et al., 2009). However, the functional importance of this structure is questionable as helix-breaking

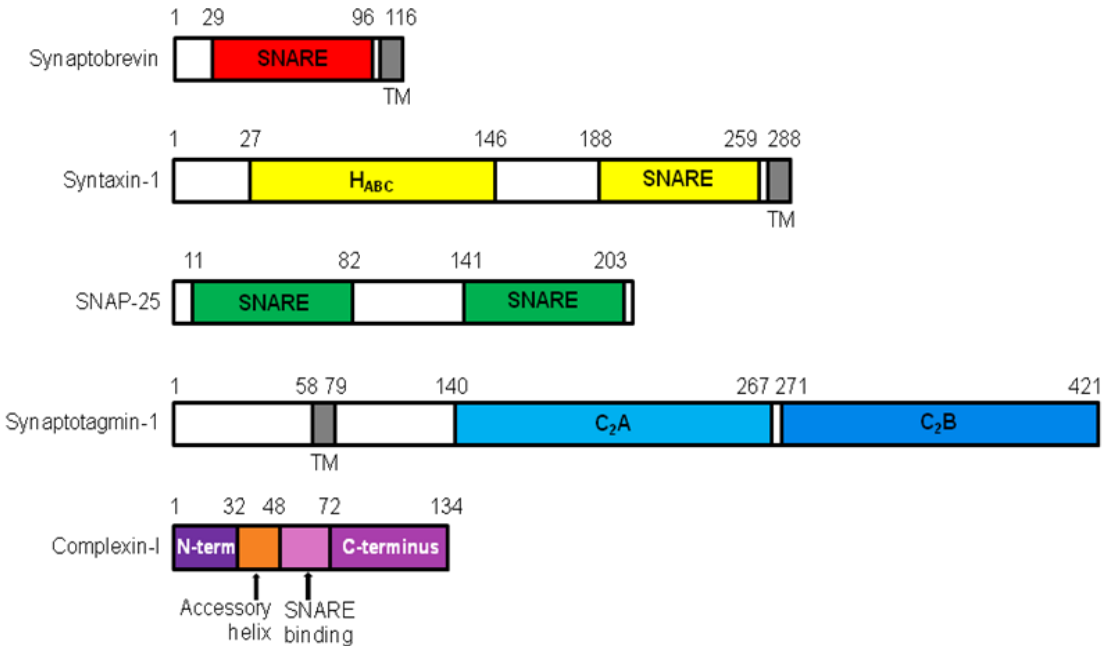

Figure 1.3 Domain structure of the SNAREs, Syntaptotagmin-1, and Complexin-I. Synaptobrevin is linked to synaptic vesicles via a transmembrane region and has a single SNARE motif composing most of the sequence. Syntaxin-1 is composed of an N-terminal H_{ABC} domain that inhibits SNARE complex formation, a C-terminal SNARE motif, and a transmembrane region that links it to the plasma membrane. SNAP-25 has N-terminal and C-terminal SNARE motifs joined by a long linker that associates with the plasma membrane through palmitoylated cysteines. Synaptotagmin-1 is localized to synaptic vesicles via an N-terminal transmembrane region, while two C-terminal C_2 domains can bind Ca^{2+}, lipids, and SNAREs. Complexin-I is composed of a N-terminal SNARE binding sequence, an accessory helix that associates with the SNARE complex indirectly via a SNARE binding helix, and a C-terminal domain that may link it with synaptic vesicles (adapted from Rizo and Rosenmund, 2008).

proline residues in the juxtamembrane region of synaptobrevin do not affect neurotransmitter release (Kesavan et al., 2007). In addition, lipid-anchored SNAREs lacking transmembrane regions retain spontaneous release and either fully retain evoked released if only syntaxin or synaptobrevin have the lipid-anchor replacement or partially retain evoked releace if both syntaxin and synaptobrevin have the lipid-anchor replacement (Zhou et al., 2013b).

Prior to vesicle docking, syntaxin and SNAP-25 can form a heterodimeric 2:1 complex. This complex is a physiological dead end as synaptobrevin cannot enter to form the SNARE complex necessary for membrane fusion (Fasshauer and Margittai, 2004; Weninger et al., 2008). This syntaxin-SNAP-25 complex is broken apart by NSF-α-SNAP to prevent this dead end from occurring (Ma et al., 2013). To keep the complex from reforming in absence of synaptobrevin, Munc18 sequesters syntaxin in a closed conformation that limits accessibility to its SNARE domain (Burkhardt et al., 2008; Misura et al., 2000). Through interaction with the SNARE domain, Munc13 opens the closed conformation of syntaxin, templating the correct SNARE complex to form with synaptobrevin (Ma et al., 2011).

Despite extensive studies performed on the SNAREs, their importance and role in membrane fusion is still unclear. The main evidence for the importance of SNAREs comes from either top-down or bottom-up approaches of knockout or reconstitution studies, respectively. Mice deficient of synaptobrevin exhibit severely impaired neurotransmitter release, but not complete loss of release, especially spontaneous release, indicating that synaptobrevin is required, although not absolutely essential (Schoch et al.,

2001). SNAP-25 knockouts exhibit an even more severe phenotype with evoked neurotransmitter release abolished and loss of most spontaneous release (Bronk et al., 2007). Syntaxin 1A knockouts have normal release compared to wild type neurons (Fujiwara et al., 2006), but syntaxin 1A/1B knockouts do exhibit deficiencies in asynchronous evoked release and spontaneous release (Mishima et al., 2014). The moderate effect of syntaxin removal is likely due to compensation from other syntaxin proteins. Overall, these knockout studies point to the SNAREs being absolutely critical for calcium triggered neurotransmitter release, although they might not be completely necessary for release such as the case with synaptobrevin and syntaxin.

Reconstitution studies have mostly focused on neuronal SNAREs reconstituted into liposomes. Under certain conditions such as high curvature stress, large protein to lipid ratios, and the possible presence of detergent, efficient lipid mixing between these proteoliposomes could be achieved with SNAREs alone (Weber et al., 1998). Use of more reasonable liposome reconstitutions with larger liposomes, smaller protein to lipid ratios, less harsh use of detergents, and overall more homogeneous samples yielded little or no lipid mixing with SNAREs alone (Chen et al., 2006). As these studies only measured lipid mixing, disruption of liposomes via bursting or mechanisms other than true fusion where content leaking occurs could be responsible for any positive result. Later studies with other synaptic proteins thought to be directly necessary for fusion including synaptotagmin, complexin, Munc18, and Munc13 were able to achieve efficient lipid mixing with more reasonable proteoliposome preparations (Boswell et al., 2012; Ma et al., 2013; Shen et al., 2007; Xue et al., 2008). However, these

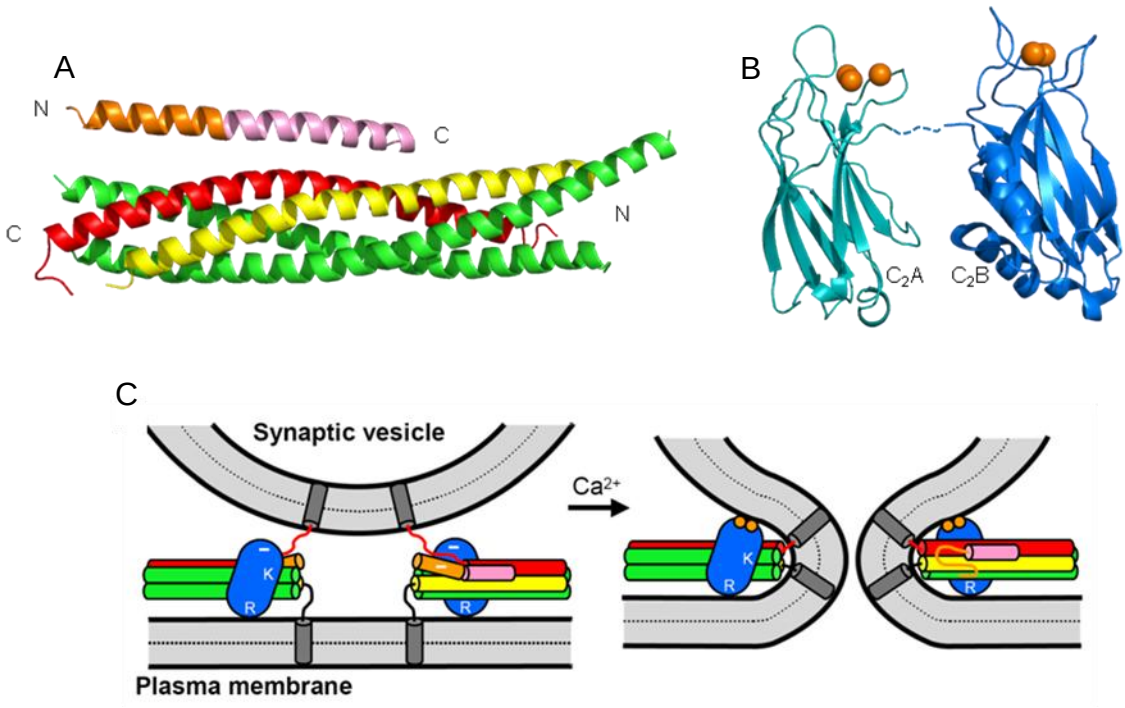

Figure 1.4 Protein machinery of Ca^{2+}-dependent synaptic vesicle fusion. (A) Crystal structure of the complexin/SNARE complex. Synaptobrevin (red), syntaxin-1 (yellow), and SNAP-25 (green) form the SNARE complex four helix bundle with the complexin SNARE binding region (pink) attached directly, alongside the accessory helix (orange) attached indirectly. (B) Structures of the C_2A (cyan) and C_2B (blue) of synaptotagmin-1 bound to Ca^{2+} (orange). (C) In the working model of Ca^{2+}-dependent synaptic vesicle fusion prior to release, SNARE complex formation brings together the synaptic vesicle and plasma membranes, but complexin and the Syt1 C_2B domain inhibit synaptobrevin from fully assembling by repelling the negatively charged synaptic vesicle. Syt1 C_2B interacts with the SNARE complex through its polybasic region (K) and with one membrane through R398 and R399 (R). Upon Ca^{2+} influx, the Ca^{2+} binding loops of the

C_2B domain bind to the synaptic vesicle, causing unfolding of the complexin accessory helix and allowing for full SNARE complex assembly. This mechanism removes both sources of membrane fusion inhibition and stimulates fast neurotransmitter release.

reconstitutions did require the SNAREs, as the single proteins alone have not been shown to induce lipid mixing under native conditions (Xu et al., 2011). Overall, reconstitution studies of synaptic proteins indicate that that SNAREs are necessary, but not sufficient for membrane fusion.

With the role of SNAREs in membrane fusion being widely studied, the mechanism behind SNAREs contributing to membrane fusion is still mostly unknown. The leading hypothesis is that the zippering of SNAREs provides a large portion of energy necessary for fusion. The stabilization energy of a single SNARE complex was found to be 35 to 65 k_BT (Gao et al., 2012; Li et al., 2007), close to the energy necessary to reach hemifusion (Cohen and Melikyan, 2004). This result is also consistent with other studies that demonstrated one to three SNARE complexes are necessary for fusion (Mohrmann et al., 2010; van den Bogaart et al., 2010). A large caveat still exists for these results in that the SNARE complex is zippered partially prior to the actual fusion event (Gao et al., 2012), so a large amount of the folding energy hypothesized to be used for fusion is actually lost completely. After vesicle docking and priming, the SNARE complex should be at least half folded, as the N-terminal half of the SNARE complex can fold independently (Trimbuch et al., 2014), and the t-SNAREs can zipper along their entire SNARE domains without synaptobrevin (Weninger et al., 2008). However, at least some energy of SNARE complex folding should contribute to membrane fusion, as studies where the linker was lengthened between the SNARE motif and transmembrane domain showed at least some impaired membrane fusion or neurotransmitter release (Kesavan et al., 2007; McNew et al., 1999), but the energy contributed by SNARE

folding used for fusion remains unknown. Numerous studies examining and perturbing SNARE function over the years have revealed that while the SNARE complex is absolutely critical for membrane fusion and neurotransmitter release, it cannot be considered a minimal fusion machine. Other proteins involved directly in membrane fusion must be included to understand the mechanism synaptic vesicle exocytosis.

1.2.2 Synaptotagmin

Synaptotagmins are composed of a transmembrane region, a linker, and two C_2 domains composed of a β-sandwich [(Fernandez et al., 2001; Sutton et al., 1995); Figure 1.3]. Seventeen mammalian isoforms of synaptotagmin are currently known. Synaptotagmin-1 can bind a total of five calcium ions through the loops at the top of each domain, three Ca^{2+} ions through the C_2A domain and two Ca^{2+} ions through the C_2B domain [(Fernandez et al., 2001; Ubach et al., 1998); Figure 1.4B]. The calcium affinities for the C_2A domain are 54 μM, 530 μM, and >20 mM (Fernandez-Chacon et al., 2001), and the calcium affinities for the C_2B domain are 300-400 μM and 500-600 μM (Fernandez et al., 2001). Both domains can bind membranes through the calcium binding loops, but only in the presence of calcium. The affinity for calcium of the C_2 domains is also increased in the presence of membranes as negatively charged lipids allow the complete coordination of calcium that is only partially coordinated by the synaptotagmin calcium binding loops alone (Zhang et al., 1998).

Knockout of synaptotagmin-1 abolishes fast synchronous neurotransmitter release, while the slower but still fast asynchronous release is unaffected (Geppert et al.,

1994). Synaptotagmin knockouts also exhibit increased spontaneous release indicating that synaptotagmin can also inhibit neurotransmitter release as a membrane fusion clamp (Xu et al., 2009). The binding of calcium to synaptotagmin-1 and loss of synchronous release in synaptotagmin-1 knockouts hinted at synaptotagmin-1 being the calcium sensor for fusion. To show this definitively, mutations were made to decrease or increase the apparent calcium affinity in the calcium-dependent phospholipid binding of synaptotagmin-1. The effect of these mutations on phospholipid binding paralleled changes in the calcium sensitivity of release in neurons, strongly confirming the role of synaptotagmin-1 as the putative calcium sensor for neurotransmitter release (Fernandez-Chacon et al., 2001; Rhee et al., 2005).

Despite all synaptotagmins containing two C_2 domains, the C_2A and C_2B domains do differ strongly in importance. Mutations in the C_2B calcium binding loops impair neurotransmitter much more strongly than corresponding C_2A mutations, demonstrating that C_2B calcium binding is more critical for release (Mackler et al., 2002; Nishiki and Augustine, 2004). The C_2B domain can also bridge to two membranes simultaneously by binding to lipids through its top calcium binding loops and bottom non-Ca^{2+} binding loops using arginines R398 and R399 (Figure 1.4C), while C_2A can only bind one membrane (Arac et al., 2006; Xue et al., 2008). However, this mechanism of membrane bridging is calcium dependent, as the negative aspartates used to bind calcium in the C_2B domain upper loops repel negatively charged lipids in membranes when free of calcium. This negative to positive switch is another way membranes can be brought together, similar to how SNAREs tie membranes together in space.

The C_2 domains of synaptotagmin appear to be largely independent of each other. The two dimensional ^{1}H-^{15}N heteronuclear single quantum coherence (HSQC) spectra of the individual C_2 domains obtained separately overlap completely with the spectrum of the domains expressed as a single construct (Arac et al., 2006). This result indicates that the two domains experience the same chemical environment whether alone or in tandem and thus do not interact. This contrasts with some other proteins with tandem C_2 domains that do have interdomain interactions important to their function (Xu et al., 2014).

Synaptotagmin also has interactions with SNAREs. Early studies showed that syntaxin can interact with the calcium binding loops of synaptotagmin-1 C_2A upon binding calcium (Chapman et al., 1995; Li et al., 1995). This result is likely an *in vitro* artifact, as upon binding calcium *in vivo* the synaptotagmin calcium binding loops should bind membranes, and syntaxin would already be integrated into the SNARE complex. However, this finding did give some insight into relevant interactions as the highly negatively charged SNAREs mediate binding to the highly positively charged synaptotagmin at sites other than the calcium binding loops (Sutton et al., 1999). Later studies found interactions of synaptotagmin with the SNARE complex that were compatible with membrane binding reflecting the charged nature of these proteins (Rickman et al., 2004; Rickman et al., 2006; Zhang et al., 2002). This simultaneous binding results in a quaternary SNARE-synaptotagmin-Ca^{2+}-phospholipid (SSCAP) complex (Dai et al., 2007). Again, the C_2B domain seems to dominate the interaction of synaptotagmin with the SNARE complex through binding of a polybasic region on C_2B

to the acidic SNAREs (Figure 1.4C), further supporting its more critical role in membrane fusion over the C_2A domain.

1.2.3 Complexin

Like the SNAREs, complexin is unfolded in solution. The middle of complexin can tightly associate with the SNARE complex four helix bundle, forming an alpha helical structure antiparallel to the SNARE complex [(Chen et al., 2002); Figure 1.4A]. The central helix of complexin-1 (residues 48-70) binds directly to the middle of the SNARE complex through synaptobrevin and syntaxin interactions. The accessory helix of complexin-1 (residues 32-48) continues from the central helix, but does not directly contact the SNARE complex. The N-terminus of complexin can also bind to the C-terminus of the SNARE complex after a short linker from the accessory helix (Xue et al., 2010). The C-terminus of complexin senses membrane curvature, likely to facilitate the association of complexin with synaptic vesicles (Snead et al., 2014).

Prior to fusion, complexin acts as a clamp on neurotransmitter release (Giraudo et al., 2006; Schaub et al., 2006; Tang et al., 2006). This clamping is largely a function of the central and accessory helix of complexin. The SNARE binding helix of complexin interacts with the middle of the SNARE complex, and the accessory helix is hypothesized to prevent the C-terminus of the synaptobrevin SNARE motif from zippering to fully form the SNARE complex. The accessory helix was initially proposed to either insert in the place of synaptobrevin at the C-terminus of the SNARE complex or bind to

synaptobrevin directly to inhibit full assembly (Giraudo et al., 2009; Krishnakumar et al., 2011; Rizo and Rosenmund, 2008; Trimbuch et al., 2014), but evidence now supports a model by which the negatively charged accessory helix simply repels the negatively charged lipids in synaptic vesicles to clamp fusion by preventing synaptobrevin zippering [(Trimbuch et al., 2014); Figure 1.4C].

Synaptotagmin and complexin are functionally coupled in neurotransmitter release. Complexin may be physically displaced at least partially from SNARE complex association upon synaptotagmin binding Ca^{2+} and membranes, providing a mechanism to relieve clamping to allow for fast neurotransmitter release (Tang et al., 2006; Xu et al., 2013). However, complexin also functions as an activator in membrane fusion as complexin I/II knockout mice have severely impaired release (Xue et al., 2007). Complexin likely holds the SNARE complex in a metastable state prior to fusion, which is removed by synaptotagmin to allow for fast neurotransmitter release.

The interplay between synaptotagmin and complexin involves the accessory helix and central helix of complexin. However, the N-terminal portion of complexin is important for function as complexin-1 with residues 1-26 deleted cannot rescue neurotransmitter release in complexin I/II knockouts(Xue et al., 2007). The action of the complexin N-terminus in neurotransmitter release remains undetermined, but if the central helix of complexin is displaced from the SNARE complex, complexin can still remain associated with the site of membrane fusion either through its N-terminal interaction with the SNARE complex, C-terminal interaction with membranes, or both (Xu et al., 2013).

Combined, these results suggest that synaptotagmin and complexin cooperate to achieve efficient membrane fusion. The overall picture is that complexin along with synaptotagmin both initially clamp fusion in the absence of calcium. Upon calcium influx, synaptotagmin releases the inhibition by binding to phospholipids and causing displacement of the central region of complexin bound to the SNARE complex to allow neurotransmitter release to occur [(Trimbuch et al., 2014; Xu et al., 2013); Figure 1.4C]. In addition, synaptotagmin and the N-terminus of complexin function as activators of membrane fusion for triggering fast neurotransmitter release after this displacement (Xue et al., 2008; Xue et al., 2007).

Chapter 2 Reluctance to Membrane Binding Enables Accessibility of the Synaptobrevin SNARE Motif for SNARE Complex Formation

2.1 Introduction

Conserved families of proteins that govern traffic at most eukaryotic membrane compartments underlie a universal intracellular membrane fusion mechanism (Wickner and Schekman, 2008). The SNARE family, characterized by SNARE motifs with sequences of 60-70 aminio acids that often precede C-terminal transmembrane (TM) regions, are particularly important among these proteins (Bowen et al., 2005; Jahn and Scheller, 2006; Rizo and Rosenmund, 2008; Sudhof and Rothman, 2009). The SNAREs form a tight four-helix bundle called the SNARE complex from two apposed membranes through these motifs (Poirier et al., 1998; Sutton et al., 1998), bringing the two membranes together, which is proposed to provide the membrane fusion energy (Hanson et al., 1997). Although other universal factors such as Sec1/Munc18 proteins (Carr and Rizo, 2010; Dulubova et al., 2007; Shen et al., 2007), and synaptotagmin-1 in the specialized case of synaptic vesicle exocytosis (Chicka et al., 2008; Lee et al., 2010; Xue et al., 2008), are critical to fusion, and the mechanism of fusion is still unclear (Rizo et al., 2006), the central role SNAREs play in membrane fusion has little doubt.

The structure of the SNARE four-helix bundle representing the post fusion state either with or without the adjacent TM regions has been determined by crystallography (Stein et al., 2009; Sutton et al., 1998), but only limited structural information on the isolated SNARE motifs attached to their adjacent TM regions is available. The soluble

fragments spanning the SNARE motive were shown to be unstructured in early studies of synaptobrevin, syntaxin-1, and SNAP-25 (Dulubova et al., 1999; Fasshauer et al., 1997; Fiebig et al., 1999; Hazzard et al., 1999; Nicholson et al., 1998), the SNAREs that mediate synaptic vesicle fusion (Brunger, 2005; Rizo and Rosenmund, 2008; Sudhof and Rothman, 2009), and of the yeast plasma membrane SNAREs, although depending on conditions the syntaxin-1 SNARE motif can be unstructured or helical due to oligomerization (Chen et al., 2008; Dulubova et al., 1999; Fasshauer et al., 1997; Misura et al., 2001). Conflicting results have been obtained from analyses of the synaptobrevin SNARE motif in the context of the full-length protein. According to CD data in detergent (Bowen and Brunger, 2006) and EPR results on lipid vesicles (Kweon et al., 2003), the synaptobrevin SNARE motif is largely unstructured save a small portion near the C-terminus that is α-helical and extends into the juxtamembrane region (between the SNARE motif and the TM sequence; see Fig 2.1A). The abundance of basic and aromatic residues and tendency to form a helix in solution, as observed by NMR spectroscopy (Hazzard et al., 1999), allows the juxtamembrane region to associate with membranes (Kweon et al., 2003). On the other hand, NMR studies in dodecylphophocholine (DPC) micelles indicated that residues 36-54 of synaptobrevin, much of the N-terminal half of the SNARE motif, bind to micelles forming an α-helix (Ellena et al., 2009).

The amphipathicity and proximity of SNARE motifs to membranes could strongly favor membrane binding. This distinction is important because membrane binding might compete with and therefore hinder SNARE complex assembly, which is especially

important for the N-terminal halves of the SNARE motifs that are critical to initiate SNARE complex assembly (Pobbati et al., 2006; Sorensen et al., 2006). Thus, to fundamentally elucidate the mechanism of intracellular membrane fusion, it is critical to understand the intrinsic features of the SNARE proteins and their biochemical properties by characterizing in detail the conformational behavior of the membrane-anchored synaptobrevin SNARE motif and membrane-anchored SNARE motif in general. To do so, we have analyzed synaptobrevin reconstituted into nanodiscs, disc-like phospholipid bilayers surrounded by a scaffolding protein (Denisov et al., 2004), or into phospholipid vesicles by NMR spectroscopy,. Our results show conclusively that most of the SNARE motif of reconstituted synaptobrevin does not interact with phospholipid bilayers and remains unstructured under a variety of conditions, remaining highly accessible for SNARE complex assembly. The N-terminal sequences of the SNARE motifs appear to be optimized to avoid membrane interactions according to the data, retaining the ability to bind to other SNAREs or other fusion machinery components. The data also illustrate how misleading results can be obtained by using detergents in place of membranes, while nanodiscs more favorably capture the function of membrane proteins as they occur natively.

2.2 Material and Methods

2.2.1 Expression and Purification of Proteins

The full-length construct used to express rat synaptobrevin-2 from a pGEX-KG (Guan and Dixon, 1991) vector was previously described (Chen et al., 2006). The full-

length construct was used to prepare a separate construct by standard recombinant DNA techniques to express rat synaptobrevin-2 (1-96), the soluble fragment, also in the pGEX-KG vector. *Escherichia coli* BL21(DE3) cells were used to express the proteins. Minimal media with sole nitrogen and carbon sources of $^{15}NH_4Cl$ and $^{13}C_6$-glucose was used to prepare ^{13}C, ^{15}N labeled protein (Chen et al., 2006; Hazzard et al., 1999). Human apolipoprotein A1 residues 68-267 (ApoA1) was expressed from a pET-28a vector (Novagen), made using standard recombinant DNA techniques with cDNA obtained from ATCC. ApoA1 was expressed in LB broth with *E. coli* BL21(DE3) cells and purified as described previously (Banerjee et al., 2008).

2.2.2 Synaptobrevin Reconstitution into Vesicles and Nanodiscs

Full-length synaptobrevin was incorporated into liposomes preformed to 100-nm diameter with the desired lipid composition by detergent-assisted insertion in 20 mM 4-(2-hydroxyethyl)-1-piperazineethanesulfonic acid (HEPES) pH 7.0, 100 mM KCl, 0.3 mM tris(2-carboxyethyl)phosphine (TCEP) (reconstitution buffer), as previously described (Chen et al., 2006). The final concentrations of synaptobrevin and lipid were 10 μM and 5 mM, respectively, with a 1:500 protein-to-lipid ratio. Full-length synaptobrevin was incorporated into nanodiscs, similar to as previously described for rhodopsin (Banerjee et al., 2008). In brief, ^{13}C, ^{15}N syb 1-116 was combined with a mixture of lipid, ApoA1, sodium cholate, and n-octyl-β-D-glucopyranoside (β-OG). The lipid:ApoA1:syb ratio was 120:2:1, prepared from stock concentrations of 13 mM, 200 μM, and 110 μM, respectively, while the sodium cholate and β-OG were added to a 1%

final concentration from 10% stocks. After vortexing the mixture, it was left at room temperature for 30 minutes without disturbance. The mixture was passed over Extracti-Gel D resin (Pierce) in a 4-cm-high column to remove the detergent and form the nanodiscs. A Superdex-200 Hiload 16⁄60 column (GE Healthcare) in reconstitution buffer was used to remove any liposomes and further purify the nanodiscs. The sample was then concentrated to the desired concentration using a 30-kDa molecular weight cutoff filter.

2.2.3 NMR Spectroscopy

Varian INOVA spectrometers operating at 500, 600, or 800 MHz were used to perform all NMR experiments at 15°C. The samples were dissolved in reconstitution buffer with 5% D_2O added, except for the experiments from Figure 2.4A and B, which were at pH 6.0 but otherwise under the same conditions. The transverse relaxation and ^{1}H-^{15}N HSQC samples used approximately 10 μM protein. A ^{1}H-^{15}N HSQC-based pulse sequence incorporating a Carr–Purcell–Meiboom –Gill (CPMG) train applied to ^{15}N was used to obtain ^{15}N transverse relaxation measurements (Farrow et al., 1994). The ^{1}H transverse relaxation rates were obtained with a CPMG train applied to ^{1}H in a similar sequence. 90 μM synaptobrevin-nanodisc was used for backbone assignments, obtained with gradient-enhanced 3D CBCA(CO)NH and HNCACB experiments (Muhandiram and Kay, 1994). NMRpipe (Delaglio et al., 1995) was used to process data, and NMRView (Johnson and Blevins, 1994) was used to analyze data.

2.3 Results

2.3.1 Synaptobrevin SNARE Motif Flexibility on Nanodiscs

The very large size of phospholipid vesicles hinders the study of the structure of membrane proteins reconstituted into the vesicles by solution NMR methods. Reconstituting a protein leads to broadening beyond detection of resonances from structured parts of the protein as the size of vesicles range effectively from megadaltons to gigadaltons depending on their radii. The use of membrane proteins incorporated into nanodiscs can alleviate this problem (Gluck et al., 2009; Raschle et al., 2009; Shenkarev et al., 2009), as the effective molecular weights are in the 150-400 kDa range, but protein perdeuteration is necessary to obtain NMR data of sufficient quality for structured regions. We focused on determining which regions of the synaptobrevin sequence remained flexible reconstituted into a phospholipid bilayer in this study and thus made no attempt to observe signals from structured regions. As long as there are fast internal motions and no or minimal interactions with a larger species, resonances of a flexible polypeptide attached to a large macromolecule can remain observable, so our experiments were able to determine the flexible regions of synaptobrevin attached to a phospholipid bilayer. This principle can be illustrated by anchoring a peptide to 50-μm cross-linked polystyrene beads, where sharp signals from the peptide can still be observed (Giralt et al., 1984).

Nanodiscs with a lipid composition consisting of 85% 1-palmitoyl-2-oleoyl-sn-glycero-3-phosphocholine (POPC) and 15% 1,2-dioleoyl-sn-glycero-3-phospho-L-serine (DOPS), widely used in reconstitutions of SNARE proteins

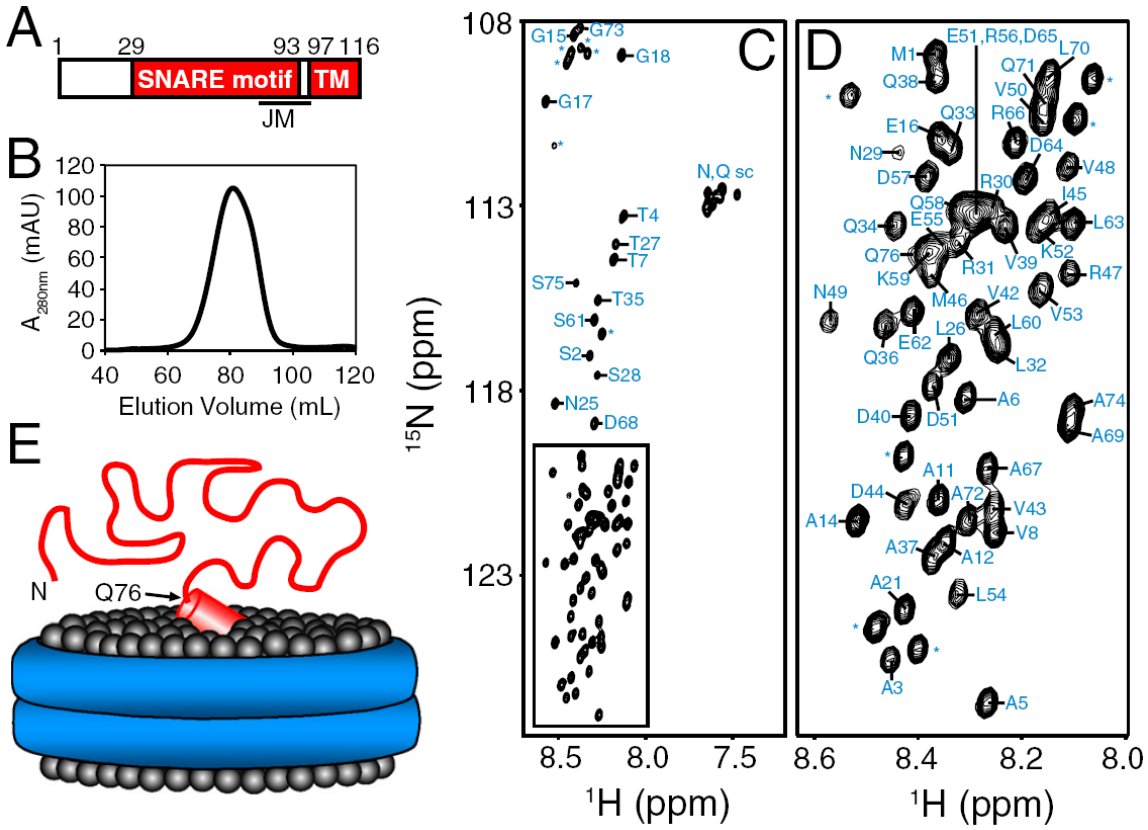

Figure 2.1 Analysis of synaptobrevin in nanodiscs by NMR. (A) Domain structure of synaptobrevin. The SNARE motif and TM region are indicated. The approximate juxtamembrane (JM) position that includes the SNARE motif C-terminus and linker joining it to the TM region is also shown. (B) Superdex200 gel filtration of synaptobrevin in nanodiscs after removing detergent and before concentration for NMR experiments. (C,D) A ^{1}H-^{15}N HSQC spectrum of ^{15}N-synaptobrevin in nanodiscs is shown with assignments (* indicates N-terminal residues from the expression vector). The box in C is expanded in D. (E) Cartoon representation of the structure of synaptobrevin (red) in nanodiscs with lipid headgroups (gray spheres) and double ApoA1 scaffold (blue rings) shown. Residues 1-76 are shown to be highly flexible, while the

tilted cylinder represents the juxtamembrane region, a helix bound in a tilted orientation to the nanodiscs based on EPR data (Kweon et al., 2003).

(Weber et al., 1998), were first used to analyze full-length synaptobrevin (residues 1–116) incorporated into a bilayer. The ratio of lipids to synaptobrevin and scaffolding protein were carefully adjusted to obtain homogenous preparations of nanodiscs as judged by gel filtration (Figure 2.1B). The nanodiscs were concentrated to 90 μM and used to obtain high-quality triple resonance data of sufficient quality to assign the backbone resonances for flexible regions. The resonances for the corresponding cross-peak assignments (Figure 2.1C and D) from the ^{1}H-^{15}N heteronuclear single quantum coherence (HSQC) spectrum are observable for residues 1-76, but not for the remaining C-terminus of the protein. These results are consistent with our model where residues 1-76, including most of the SNARE motif, are unstructured and flexible, while the sequences near the juxtamembrane to transmembrane region are structured and bound to the nanodiscs (Figure 2.1E).

The ^{1}H-^{15}N HSQC spectrum of the synaptobrevin cytoplasmic region (residues 1-96) in solution further support this model, where the assignments were previously published (Hazzard et al., 1999). Comparing the soluble fragment to the full length synaptobrevin in nanodiscs, the cross-peaks for residues 77-96 are clearly missing (Figure 2.2A and B) for the latter spectrum. The cross-peaks for residues 1-76 are nearly identical for both spectra, and these residues are unstructured for the soluble synaptobrevin 1-96 fragment. As amide chemical shifts are highly sensitive to even small changes in chemical environment, the spectra indicated that residues 1-76 in the nanodisc-anchored synaptobrevin are also unstructured, with similar conformational ensembles to the soluble fragment. In addition, the cross-peak intensity and transverse

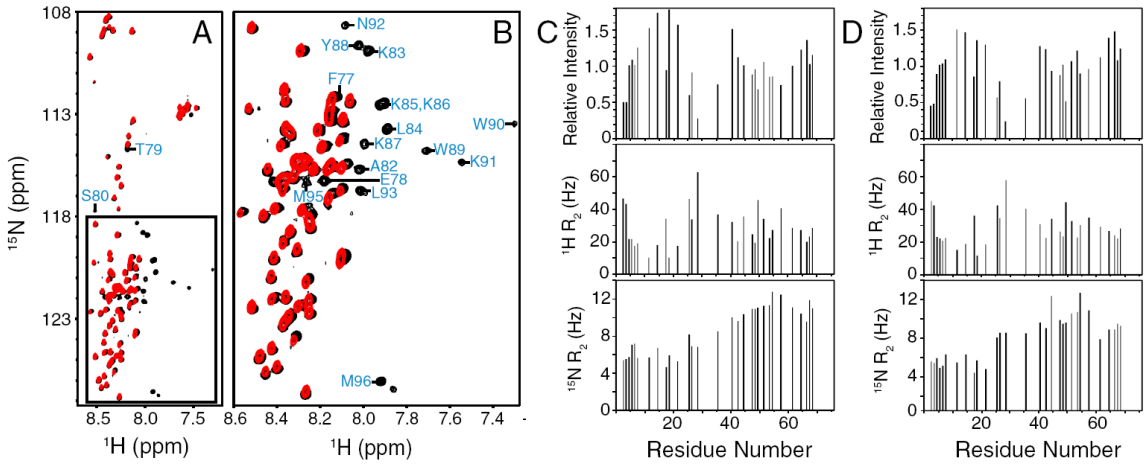

Figure 2.2 Synaptobrevin residues 1-74 have similar conformations in solution and on nanodiscs. (A,B) ^{1}H-^{15}N HSQC spectra of the soluble synaptobrevin (1-96) fragment (black contours) and full length synaptobrevin (1-116) in 85:15 POPC:DOPS nanodiscs (red contours) are superimposed. The box in A is expanded in B. The assignments for cross-peaks are indicated for soluble synaptobrevin (1-96) fragment residues not seen on nanodiscs. (C,D) Relative intensities of cross-peaks (top) and transverse relaxation rates (R_2) of ^{1}H (middle) and ^{15}N (bottom) from residue 1-74 backbone nuclei of the soluble synaptobrevin (1-96) fragment (C) or full length synaptobrevin (1-116) in nanodiscs (D). Only well-resolved cross-peaks were quantified. Relative intensities were determined by dividing the intensity of a cross-peak by the average intensity over all cross-peaks (Xue et al., 2010).

relaxation rate patterns for the residue 1-76 ^{1}H and ^{15}N backbone nuclei are very similar for the nanodisc-anchored full-length synaptobrevin and the soluble synaptobrevin (Figure 2.2C and D). These results show that the residues 1-76 of synaptobrevin do not interact with nanodisc membranes and that this segment is largely uncoupled in its conformational behavior regardless whether the juxtamembane region is free or bound to a membrane.

2.3.2 Membrane Binding Reluctance of the SNARE Motif of Reconstituted

Synaptobrevin nanodiscs are believed to be reliable models of phospholipid bilayers, but there are few demonstrations to conclude this fully. Also, *cis* interactions of the N-terminal half of the synaptobrevin SNARE motif with the nanodiscs membrane may plausibly be hindered by the limited size, being 10 nm in diameter (Denisov et al., 2004). We used vesicles to reconstitute synaptobrevin to study its properties in a much more extensively used phospholipid bilayer model. We reconstituted synaptobrevin by detergent-assisted insertion (Rigaud et al., 1995), a method that yields highly homogenous proteoliposomes (Chen et al., 2006), into preformed 100 nm vesicles composed of 85:15 POPC:DOPS. In order to limit the likelihood of crowding that would hinder *cis* interactions of the synaptobrevin SNARE with the vesicles surface, we used a protein-to-lipid ratio of 1:500, well below what is found in synaptic vesicles (Takamori et al., 2006). The reconstituted synaptobrevin in these vesicles readily formed SNARE complexes with the SNAP-25 and syntaxin-1 SNARE motifs in control experiments to show it remains functional (Figure 2.3). We were able to obtain high-quality ^{1}H-^{15}N

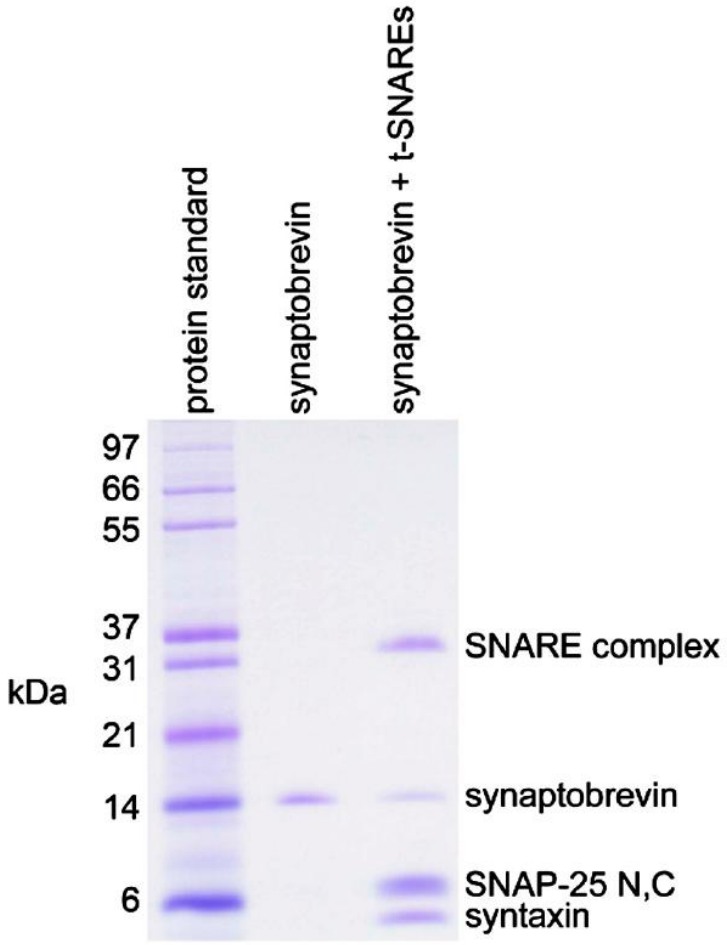

Figure 2.3 Synaptobrevin reconstituted into proteoliposomes can form SNARE complexes. Synaptobrevin in 85:15 POPC:DOPS proteoliposomes (10 μM protein, 5 mM lipid) was analyzed by SDS-PAGE before and after incubating overnight with the excess t-SNAREs syntaxin-1 (residues 191-253), SNAP-25 N-terminal SNARE domain (residues 11-82, SNAP-25 N), and SNAP-25 C-terminal domain (residues 141-203, SNAP-25 C). The SNARE complex appears on the gel due to being SDS-resistant. The unreacted synaptobrevin corresponds to the SNARE domain that is within the vesicle lumen and not accessible to the t-SNAREs.

HSQC spectra for the cross-peaks from residues 1-74 of synaptobrevin (Figure 2.4A, red contours) despite the fact the protein concentration was only 9 μM. Furthermore, the patterns of cross-peak intensities, cross-peak positions, and the ^{1}H and ^{15}N transverse relaxation rates of synaptobrevin anchored in vesicles (Figure 2.4) are remarkably similar to synaptobrevin in nanodiscs and the soluble synaptobrevin 1-96 fragment (Figures 2.1, 2.2, and 2.4A). As in nanodiscs or in solution, residues 1-74 or synaptobrevin are shown to be highly flexible and unstructured for vesicle-anchored synaptobrevin by these results.

The cytoplasmic leaflets of synaptic vesicles are negatively charged, so we included DOPS in the prior experiments. However, the synaptobrevin SNARE motif also has abundant negative charges, so we examined the possibility that synaptobrevin interactions with the membrane may be hindered by repulsion due to the negatively charged DOPS head groups. We acquired additional ^{1}H-^{15}N HSQC spectra of synaptobrevin reconstituted into 85:15 POPC:DOPS vesicles using buffer containing 1 mM Mg^{2+} and reconstituted into 100:0 POPC:DOPS vesicles. Both spectra were similar to the original spectra obtained with 85:15 POPC:DOPS vesicles without Mg^{2+} (Figure 2.5A and B). Synaptobrevin reconstituted into vesicles containing 45:20:15:20 POPC:1,2-dipalmitoyl-sn-glycero-3-phosphoethanolamine:DOPS:cholesterol, a lipid composition similar to membranes of vesicles, was also used to obtain analogous ^{1}H-^{15}N HSQC spectra [(Takamori et al., 2006); Figure 2.5C]. Again, the spectra remain similar to the other conditions. These results demonstrate that conformational behavior of residues 1-74 of synaptobrevin are not influenced by lipid composition.

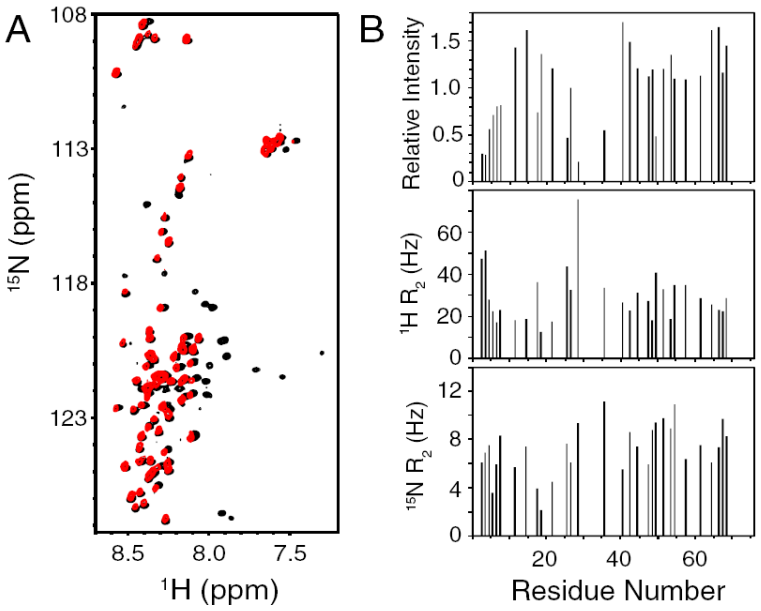

Figure 2.4 Synaptobrevin residues 1-74 have similar conformations in solution and on liposomes. (A) ^{1}H-^{15}N HSQC spectra the soluble synaptobrevin (1-96) fragment (black contours) and full length synaptobrevin (1-116) in 85:15 POPC:DOPS liposomes (red contours) are superimposed. (B) Relative intensities of cross-peaks (top) and transverse relaxation rates (R_2) of ^{1}H (middle) and ^{15}N (bottom) from residue 1-74 backbone nuclei of full length synaptobrevin (1-116) in liposomes. The analysis was the same as in Figure 2.2 C and D.

Despite these results agreeing with previous EPR and CD studies of reconstituted synaptobrevin (Bowen and Brunger, 2006; Kweon et al., 2003), our data contrast with those from an NMR study of synaptobrevin in DPC micelles that demonstrated residues 36-54 from the N-terminal portion of the SNARE motif bound to the micelles to form an alpha helix (Ellena et al., 2009). Our data suggest this region of synaptobrevin does not have affinity for membranes to any significant degree. Even if the affinity of residues of 36-54 for membranes was very weak, as might be suggested by our data where only a small population of reconstituted synaptobrevin at the most could be bound to membranes, the transverse relaxation for this region for that population would be extremely fast. As vesicles have effective sizes larger than 100 MDa for NMR purposes, the transverse relaxation rate for bound synaptobrevin would be orders of magnitude faster than the unbound state. Chemical exchange would transfer this fast relaxation to unbound protein, resulting in substantial increases in the observed relaxation rates and, therefore, large decreases in the intensity of observed resonances. For instance, the binding of a peptide to the 800 kDa GroEL tetradecamer even at a 400:1 ratio led to strong resonance broadening on the peptide in a previous study (Landry and Gierasch, 1991). We did not observe any decrease in intensity or increase in relaxation for residues 36-54 of synaptobrevin (Figures 2.2C and D and 2.4B), so the population of synaptobrevin with this region bound to membranes is essentially nonexistent. Residues 1-74 also similarly do not have any apparent affinity for membranes. Due to membrane anchoring, the local concentration of lipid should favor interaction with synaptobrevin, so residues 1-74 actually have a remarkably high reluctance to bind membranes.

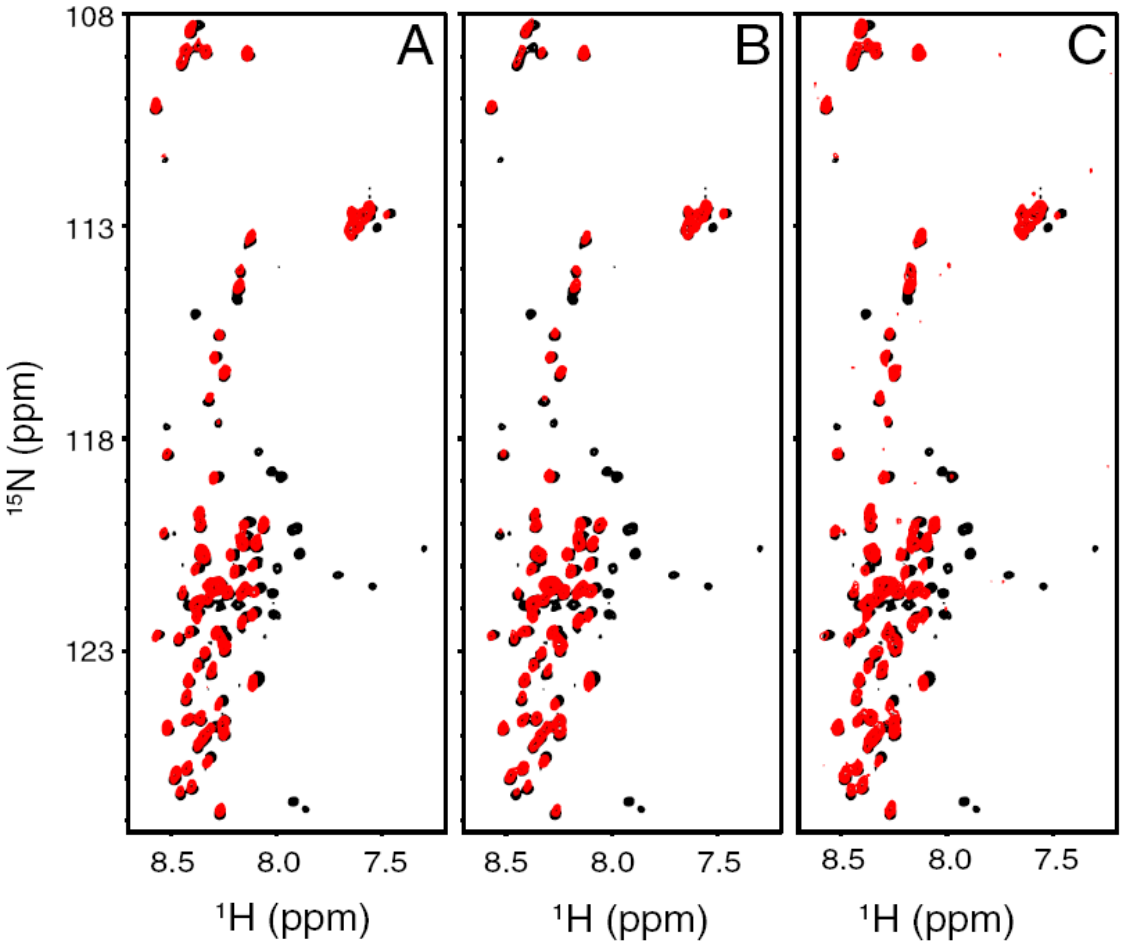

Figure 2.5 Synaptobrevin residues 1-74 have similar conformations in solution and on liposomes with Mg^{2+} or varied lipid compositions. ^{1}H-^{15}N HSQC spectra the soluble synaptobrevin (1-96) fragment (black contours) and full length synaptobrevin (1-116) in 85:15 POPC:DOPS liposomes (red contours) are superimposed as in 2.4A, but with 1 mM Mg^{2+} (A). Liposomes of 100% POPC (B) or 45:20:15:20 POPC:POPE:DOPS:cholesterol (C) are similarly shown.

2.3.3 Synaptobrevin SNARE Motif in Solution Binds to DPC Micelles but not to Liposomes

Since in all experiments our results obtained by using lipids in nanodiscs and liposomes conflicted with those obtained with DPC micelles (Ellena et al., 2009), we attempted to reproduce the latter results with synaptobrevin. Indeed, soluble synaptobrevin (1-96) in the presence of 300 mM DPC yielded a ^{1}H-^{15}N HSQC spectrum at pH 6.0 that has dramatically different changes compared with our other spectra, including the loss of cross-peaks from residues 36-54 and of C-terminal residues, as well as the appearance of new cross-peaks corresponding to residues of synaptobrevin bound to micelles (Figure 2.6A). However, the same spectra obtained with synaptobrevin 1-96 with POPC liposomes (50 mM total lipid) either at pH 6.0 or 7.0 resulted in much smaller changes, with only cross-peaks disappearing in the very C-terminus of the fragment (Figure 2.6B and C). This result further supports the conclusion that N-terminal residues 36-54 of the synaptobrevin SNARE motif do not bind to membranes and that DPC micelles are not a good membrane model to study synaptobrevin.

2.4 Discussion

By forming SNARE complexes to bring membranes together into close proximity (Hanson et al., 1997), SNARE proteins play a central role in intracellular membrane fusion. To achieve this role, the basic features of most SNARE proteins are simple: a SNARE domain followed by C-terminal transmembrane region connected together with a

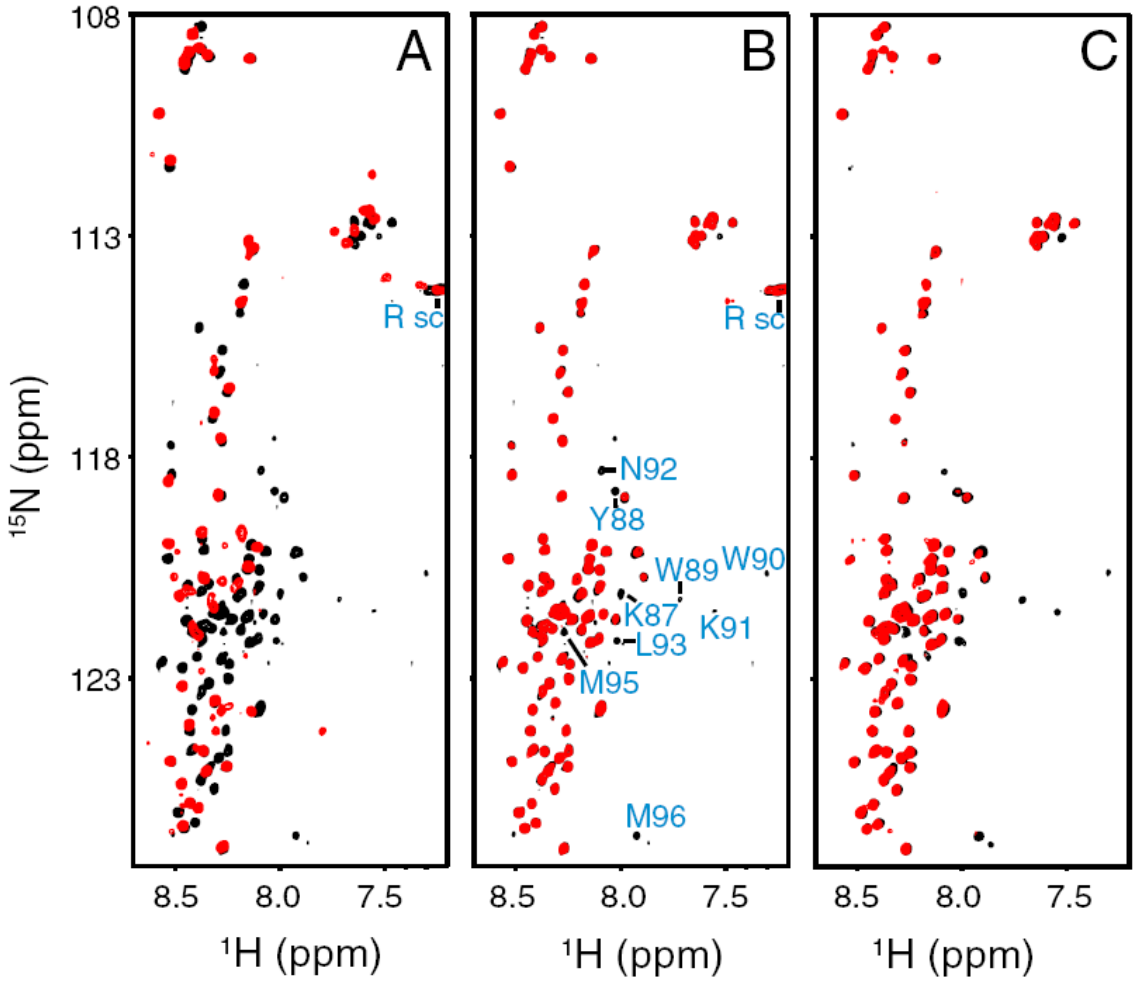

Figure 2.6 The synaptobrevin SNARE motif N-terminal half binds to DPC micelles but not liposomes. ^{1}H-^{15}N HSQC spectra the soluble synaptobrevin (1-96) fragment (black contours) alone or with (red contours) 300 mM DPC at pH 6.0 (A), 100% POPC liposomes (50 mM lipid) at pH 6.0 (B), or 100% POPC liposomes (50 mM lipid) at pH 7.0 are superimposed. The cross-peaks that disappear upon liposome addition are labeled in B (Arg side chains visible at pH 6.0 but not pH 7.0 are labeled Rsc). In A, there are less visible cross-peaks in DPC than seen previously (Ellena et al., 2009) as we used much less protein concentration, but the data are in full agreement.

short linker [with the exception of regulatory domains such as the H_{abc} domain of syntaxin-1 (Fernandez et al., 1998)]. The SNARE motif is able to form an amphipathic helix in order to integrate into the SNARE complex. This feature could be problematic as the SNARE motif prior to SNARE complex formation is in close proximity to a membrane which would favor a hydrophobic interaction. It had been suggested that this interaction could help SNARE complex formation by nucleating the helical structure (Ellena et al., 2009), but helix-to-coil transitions can occur on the nanosecond timescale and should not limit fusion which can only occur as fast as 100 μsec. In fact, with the hydrophobic side of the SNARE motif sequestered, it seems more likely a membrane interaction would hinder interactions with SNAREs or other fusion machinery and inhibit SNARE complex assembly. The N-terminal portions of SNARE motifs are particularly critical in this respect as they are believed to be important for initiation of SNARE complex assembly (Walter et al., 2010). Proteins such as Munc13s may also form scaffolds for SNARE complex formation through binding to the N-terminal SNARE motifs (Basu et al., 2005; Guan et al., 2008; Weninger et al., 2008). Our data show that a majority of the SNARE motif for reconstituted synaptobrevin does not bind membranes and actually appears to be remarkably reluctant to bind membranes considering its amphipathicity. We speculate that the disinclination to bind membranes may be a general property of SNARE motifs as part of their intrinsic anatomy, which may be fundamental for them to function properly in intracellular membrane fusion.

The SNARE motif of synaptobrevin has an abundance of acidic residues aside from its basic C-terminus. The highly negative charge is a shared feature of many

SNARE domains including syntaxin-1 (Fasshauer et al., 1998), which should allow SNAREs to repel the negative surface of membranes, leading to reluctance to bind membranes in even a small degree. This feature of SNAREs can also be contradictory to their function, as it imposes an addiction energy barrier to bringing membranes together in close proximity, but can provide a mechanism of regulation as well. The energy of SNARE complex formation and interactions of the positively charged C-termini of SNARE domains with the membranes may compensate for the repulsive forces between membranes and SNAREs and between the two membranes themselves. By combining the attractive and repulsive forces, the SNAREs may be able to create leverage in order to bend the membranes and initiate membrane fusion. Electrostatic potential calculations have supported this notion, and other proteins binding to different regions of the SNARE complex (Chen et al., 2002; Dai et al., 2007; Xu et al., 2010; Xue et al., 2010) and one or both membranes can assist and/or regulate this process (Arac et al., 2006; Dai et al., 2007; Guo et al., 2010; Xue et al., 2008).

Aside from how the negative charges of SNARE motifs may play a role in membrane fusion, our results clearly demonstrate that the synaptobrevin SNARE motif does not bind to membranes, even when all negative lipids are removed (Figures 2.5B and 2.6B and C). Therefore, electrostatic repulsion does not fully explain the reluctance of membrane binding of the SNARE motifs, which may be a more intrinsic, fundamental property instead. As evolution has selected SNARE motifs that form four helix bundles rather than three- or two-helix bundles, the number of hydrophobic residues in the helices may be too low to establish hydrophobic contacts on the membrane with enough energy

to overcome lipid bilayer insertion. SNARE motif sequences may be therefore optimized to have enough hydrophobicity to allow highly stable SNARE complexes to form while avoiding membrane insertion.

Despite the inability of the N-terminal half of the synaptobrevin SNARE motif to bind membranes, it interestingly does bind to DPC micelles [(Ellena et al., 2009); Figure 2.6A]. The reason for this difference is not certain, but micelles may plausibly be more adaptable and dynamic that phospholipids bilayers, allowing sequences of limited hydrophobicity to interact more easily. However, the discrepancy between earlier studies that suggested the SNARE motif of reconstituted synaptobrevin is flexible (Bowen and Brunger, 2006; Kweon et al., 2003) and the NMR study that showed the same SNARE motif binds to micelles (Ellena et al., 2009) is not a true contradiction, as the behavior of the protein differs between the two systems. DPC micelles are highly different physically than native membranes and appear to not be a good bilayer model for synaptobrevin. Bicelles have also been examined as a model for this system, with the N-terminal region of the synaptobrevin SNARE motif interacting with the bicelle slightly (<10% population) to form a helix (Liang et al., 2014). The small helical population is possibly due to interactions of synaptobrevin with the micelle-like assembly encapsulating the membrane bilayer. Our results reveal that synaptobrevin has very similar properties when using either nanodiscs or liposomes, showing that nanodiscs can be an appropriate membrane model for SNAREs. The NMR experiments presented here focus on the flexible regions of synaptobrevin, but fusion assays have also shown that synaptobrevin in nanodiscs can function similarly to synaptobrevin in phospholipid vesicles in SNARE-

mediated fusion assays (Shi et al., 2012). In addition, structured regions of membrane proteins in nanodiscs can yield good-quality NMR data in some studies (Gluck et al., 2009; Raschle et al., 2009; Shenkarev et al., 2009). Nanodiscs are therefore a promising avenue to explore the structure and function of membrane proteins, such as the SNAREs and their associated proteins, in a highly native environment.

Chapter 3 Conformation of Synaptotagmin-1 on Nanodiscs

3.1 Introduction

Ca^{2+} influx into the presynaptic terminal triggers neurotransmitter release, a key process in interneuronal communication (Rizo and Sudhof, 2012). The Ca^{2+} sensor for fast neurotransmitter release is the synaptic vesicle protein synaptotagmin-1, functioning primarily though the two C_2 domains (C_2A and C_2B) that comprise the majority of its sequence (Brunger et al., 2009; Chapman, 2008; Fernandez-Chacon et al., 2001; Jahn and Fasshauer, 2012). Synaptotagmin-1 couples its function to membrane fusion through SNARE proteins (Bhalla et al., 2006; Xue et al., 2008), which form SNARE complexes to tether together the vesicle and plasma membranes in synapses (Brunger et al., 2009; Jahn and Fasshauer, 2012). Synaptotagmin-1 function is also tightly coupled with complexins (Giraudo et al., 2006; Schaub et al., 2006; Tang et al., 2006), along with other key membrane fusion proteins (Ma et al., 2013; Parisotto et al., 2012). The C_2A and C_2B domains of synaptotagmin-1 are β-sandwich structures that bind three and two Ca^{2+} ions respectively, through loops at the top of each domain (Fernandez et al., 2001; Sutton et al., 1995; Ubach et al., 1998). Ca^{2+}-dependent phospholipid binding is also mediated by these top loops (Chapman and Davis, 1998; Fernandez et al., 2001; Zhang et al., 1998), which is central to the function of synaptotagmin-1(Fernandez-Chacon et al., 2001; Rhee et al., 2005). Liposomes and chromaffin granules are clustered by the cytoplasmic region of synaptotagmin-1 (Damer and Creutz, 1994). A fragment containing both C_2 domains was able to simultaneously bind two membranes and bring them into close proximity (~4

nm), as seen by cryo-EM (Arac et al., 2006). The C_2B domain alone can surprisingly cluster membranes as well (Arac et al., 2006), but not the C_2A domain, consistent with the stronger role the C_2B domain plays in neurotransmitter release (Mackler et al., 2002; Robinson et al., 2002). By mutating two arginines (R398 and R399) at the bottom of the C_2B domain, neurotransmitter release is impaired, along with the ability of the C_2B domain to cluster liposomes and stimulate SNARE-mediated lipid mixing (Arac et al., 2006; Xue et al., 2008). These results together suggested that the C_2B domain of synaptotagmin-1, cooperating with the SNAREs, bridges two membranes via interactions through the top Ca^{2+} binding loops and the bottom arginine residues in order to induce membrane fusion (Arac et al., 2006; Dai et al., 2007; Xue et al., 2008).

Despite the fact that the C_2B domain can bridge membranes, the role of the C_2A domain is still in question. The C_2A domain may assist in bridging membranes in a Ca^{2+} dependent manner by cooperating with the C_2B domain to bind adjacent membranes to bring them together. The C_2A domain might also bind to the same membrane as the C_2B domain and perform another function in neurotransmitter release. A previous EPR study found that the most likely orientation of the two C_2 domains was an antiparallel orientation allowing the domains to bind to different membranes through the Ca^{2+} binding loops, although the domains do adopt a wide range of relative conformations (Herrick et al., 2009). To address this issue further, we examined the relative orientation of a C_2AB construct of synaptotagmin-1 on small lipid bilayer nanodiscs. Through paramagnetic broadening using the nitroxide radical MTSL, we show that some, but not all synaptotagmin molecules bind to apposed membranes. With this result in mind, we

propose a model where the C_2 domains of synaptotagmin can bind both apposed membranes or the same membrane either near the site of fusion where the membranes are close in space or further away from the site of fusion where the membranes are separated.

3.2 Material and Methods

3.2.1 Expression and Purification of Proteins

The expression rat synaptotagmin-1 C_2AB (residues 140-421) from a pGEX-KG vector was previously described (Arac et al., 2006; Ubach et al., 2001). ^{2}H-ILV-$^{13}CH_3$-C_2AB was produced by growing the protein in M9 minimal expression media with 99.9% D_2O and ^{2}H,^{12}C-glucose as the sole carbon source (3 g/L). Methyl-labeling was achieved by adding [3,3-$^{2}H_2$] ^{13}C-methyl alpha-ketobutyric acid (80 mg/L) and [3-^{2}H] ^{13}C-dimethyl alpha-ketoisovaleric acid (80 mg/L) (Cambridge Isotope Laboratories) to the deuterated protein cultures 30 minutes prior to Isopropyl β-D-1-thiogalactopyranoside (IPTG) induction. Human apolipoprotein A1 residues 68-267 (ApoA1) was expressed from a pET-28a vector (Novagen), made using cDNA obtain from ATCC with standard recombinant DNA techniques. ApoA1 was expressed in LB broth with *E. coli* BL21(DE3) cells and purified as described previously (Banerjee et al., 2008; Brewer et al., 2011).

3.2.2 Preparation of Nanodiscs

Nanodiscs were prepared similar to as previously described (Banerjee et al., 2008; Brewer et al., 2011). In brief, lipid (85:15 POPC:DOPS), ApoA1, sodium cholate, and n-

octyl-β-D-glucopyranoside (β-OG) were first mixed. The lipid:ApoA1 ratio was 130:2, prepared from stock concentrations of 13 mM and 200 μM respectively, while the sodium cholate and β-OG were added to a 1% final concentration from 10% stocks. After vortexing the mixture, it was left at room temperature for 30 minutes without disturbance. The mixture was passed over Extracti-Gel D resin (Pierce) in a 4-cm-high column to remove the detergent and form the nanodiscs. A Superdex-200 Hiload 16⁄60 column (GE Healthcare) in reconstitution buffer was used to remove any liposomes and further purify the nanodiscs in 25 mM Tris-HCl pH 7.4, 125 mM NaCl, 1 mM $CaCl_2$. The sample was then exchanged to the same buffer in 100% D_2O using a 30-kDa molecular weight cutoff filter and then concentrated.

3.2.3 Synaptotagmin Spin Labeling

^{2}H-ILV-$^{13}CH_3$-C_2AB N248C or V304C were treated with 10 mM DTT that was subsequently removed by cation exchange chromatography using Source S media. The buffer composition after the ion exchange was 50 mM sodium acetate pH 6.2, ~400 mM NaCl, and 5 mM $CaCl_2$. The protein was concentrated to 40-60 μM and incubated overnight at 4°C while rotating with a 10-fold molar excess of (1-oxyl-2,2,5,5-tetramethyl-2,5-dihydro-1H-pyrrol-3-yl)methyl methanesulfonothioate (MTSL) from a 40 mM stock in dimethyl sulfoxide. The excess MTSL was removed by buffer exchange into 25 mM Tris-HCl pH 7.4, 125 mM NaCl, 1 mM $CaCl_2$, then exchanged to the same buffer in 100% D_2O. To remove the paramagnetic activity of MTSL, the samples were reduced with 1 mM ascorbic acid and 1 mM sodium dithionite from a 100 mM stock

adjusted to pH 7.4. The reducing agent stock was prepared immediately before use (within 30 minutes) due to the high instability of dithionite.

3.2.4 NMR Spectroscopy

Varian INOVA spectrometers operating at 600 or 800 MHz were used to perform all NMR experiments at 25°C. ^{1}H-^{13}C heteronuclear multiple-quantum coherence (HMQC) spectra were acquired for 2-12 hours with 100% D_2O as the solvent. NMRpipe (Delaglio et al., 1995) was used to process data, and NMRView (Johnson and Blevins, 1994) was used to analyze data.

3.3 Results

3.3.1 A Substantial Population of the Two Synaptotagmin C_2 Domains Adopt an Antiparallel Orientations on Nanodiscs

Because the C_2A Ca^{2+}-binding loops bind to membranes for the majority of C_2AB molecules, and NBD fluorescence data shows that a smaller population of C_2B molecules bind to membranes through the bottom arginines (R398 and R399), a population of C_2AB molecules in an antiparallel orientation should exist (Seven et al., 2013). An EPR study that measured the distance between nitroxide radicals similarly concluded the domains were preferentially arranged in an antiparallel orientation in solution and on membranes (Herrick et al., 2009). Both EPR and NMR studies revealed no apparent interaction between the C_2A and C_2B domains despite this preferred orientation. However, no measurements were obtained from the top of one domain to the bottom of the other

domain in any EPR or NMR study. To determine the proximity of the opposite ends of the C_2A and C_2B domains directly, we used NMR spectroscopy to analyze the C_2AB construct bound to nanodiscs, disk-like phospholipid bilayers surrounded by the scaffolding protein ApoA1 (Denisov et al., 2004). Due to the large size of this system when C_2AB is bound to nanodiscs, we required high sensitivity for these experiments, so we used the approach of methyl transverse relaxation-optimized spectroscopy (TROSY). We produced perdeuterated C_2AB with $^{1}H,^{13}C$-labeled methyl groups for Ile, Leu, and Val residues (^{2}H-ILV-$^{13}CH_3$-C_2AB) and acquired ^{1}H-^{13}C HMQC spectra that have strong signal intensity at moderate protein concentrations for even large protein complexes (Ruschak and Kay, 2010).

Compared to the cross-peaks for Ca^{2+}-free ^{2}H-ILV-$^{13}CH_3$-C_2AB for a ^{1}H-^{13}C HMQC spectrum, the resonances of ^{2}H-ILV-$^{13}CH_3$-C_2AB bound to nanodiscs containing 15% DOPS in the presence of 1 mM $CaCl_2$ are much broader (Figure 3.1A and B), although the signals can still be seen due to the high sensitivity. In the absence of nanodiscs, progressive changes can be seen for the methyl group cross-peaks in the Ca^{2+} binding loops of ^{2}H-ILV-$^{13}CH_3$-C_2AB as Ca^{2+} is added at 0, 1, and 20 mM concentrations, similar to the behavior of amide groups (Ubach et al., 1998). Additional cross-peak movements in the ^{1}H-^{13}C HMQC spectra of ^{2}H-ILV-$^{13}CH_3$-C_2AB with nanodiscs and 1 mM $CaCl_2$ are also seen (Figure 3.1C). The protein should be fully bound with Ca^{2+} at this lower concentration when the nanodiscs are included as the lipids help to coordinate the calcium. Indeed, our results show that ^{2}H-ILV-$^{13}CH_3$-C_2AB is fully bound to nanodiscs with 1 mM Ca^{2+} and that there are no cross-peaks present from

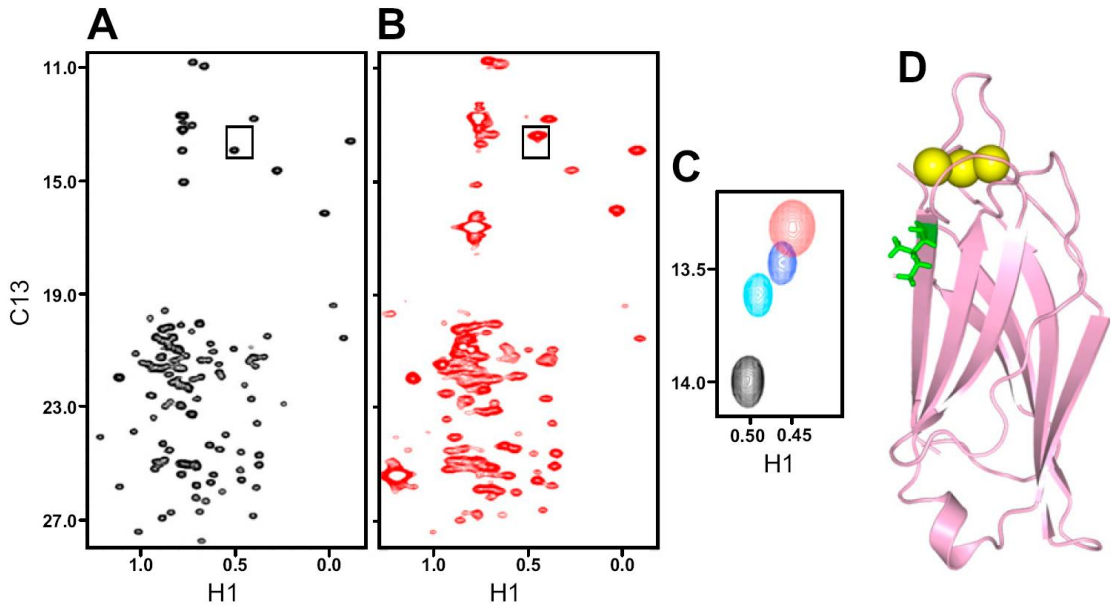

Figure 3.1 Analysis of C_2AB on nanodiscs by NMR. (A and B) ^{1}H-^{13}C HMQC spectra of 50 µM ^{2}H-ILV-$^{13}CH_3$-C_2AB with 1 mM EDTA (A) or with 1 mM Ca^{2+} and 60 µM nanodiscs (B). (C) Expansion of the cross-peak from Ile239 (rectangle from A and B) for 50 µM ^{2}H-ILV-$^{13}CH_3$-C_2AB with 1 mM EDTA (black), 1 mM Ca^{2+} (cyan), 20 mM Ca^{2+} (blue), or 1 mM Ca^{2+} and 60 µM nanodiscs (red). (D) Synaptotagmin-1 C_2A ribbon diagram showing the I239 location (green sticks) and Ca^{2+} ions (yellow spheres).

even a small population of unbound protein. Dynamic light scattering (DLS) experiments showed that C_2AB does not cluster nanodiscs and that even nanodiscs bridging does not occur under these experimental conditions, so the NMR spectra acquired should represent the distribution of C_2AB conformers bound to a single membrane.

To examine the orientation of the C_2A and C_2B domain relative to each other in a C_2AB construct, we prepared mutants of ^{2}H-ILV-$^{13}CH_3$-C_2AB of either N248C, at the bottom of the C_2A domain, or V304C, at the top of the C_2B domain, and labeled the cysteines with the paramagnetic probe MTSL. We obtained ^{1}H-^{13}C HMQC spectra for both mutants of ^{2}H-ILV-$^{13}CH_3$-C_2AB fully bound to nanodiscs before (oxidized) and after (reduced) removing the paramagnetic activity of MTSL by reduction. Comparing the two spectra allows us to determine paramagnetic broadening effects (PBEs), defined here as the ratio of the intensities of the cross-peaks in oxidized and reduced spectra (Clore and Iwahara, 2009). NMR active nuclei unaffected by the MTSL because they are far away from the probe should have a PBE of ~1.0, while nuclei very close to the MTSL would have a PBE of ~0.0. The intradomain PBEs of the C_2A domain for the N248C mutant and the C_2B domain for the V304C mutant observed from the ^{1}H-^{13}C HMQC cross-peaks (Figure 3.2) followed the expected $1/r^6$ dependence (r=distance between the methyl group and MTSL), determined by the known structures of the individual domains (Fernandez et al., 2001; Shao et al., 1998; Sutton et al., 1995).

We observed interdomain PBEs in several regions of the C_2B domain for the N248C mutant and the C_2A domain for the V304C mutant, consistent with previous

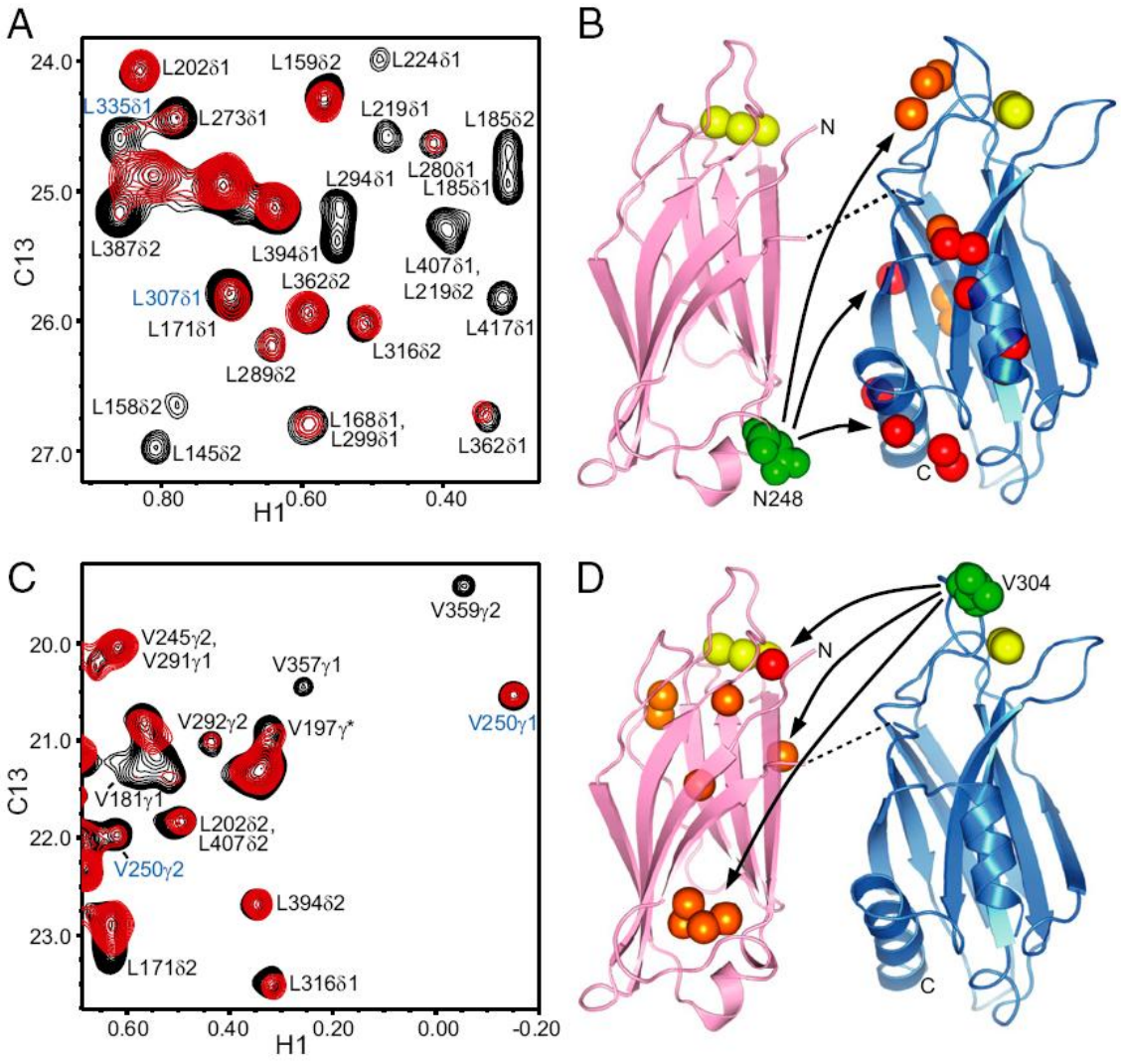

Figure 3.2 PBE Analysis of C_2AB on nanodiscs. (A and C) ^{1}H-^{13}C HMQC spectra of 50 µM ^{2}H-ILV-$^{13}CH_3$-C_2AB N248C-MTSL with 1 mM Ca^{2+} and 60 µM nanodiscs after (black) and before (red) reduction of the MTSL. Assignments for the C_2A and C_2B domains were based on our previous NMR studies on the isolated domains (Fernandez et al., 2001; Shao et al., 1998) and are labeled for well-resolved cross-peaks. The cross-peaks for methyls labeled in blue are indicative of PBEs showing an antiparallel C_2

domain orientation (at the top of the C_2B domain in A and at the bottom of the C_2A domain in C). (B and D) Interdomain PBE summary for N248C-MTSL (B) and V304C-MTSL (D). The C_2A (left) and C_2B (right) ribbon diagrams are shown with Ca^{2+} ions (yellow spheres) and the residues mutated to cysteine (green spheres). Strong PBEs (0-0.4, red spheres) and medium PBEs (0.4-0.6, orange spheres) are shown at the site of the methyl carbons for residues 294, 387, 394, 401, 409, 413, and 417 (red) and 273, 291, 292, 307, and 335 (orange) in B; 171 (red) and 149, 158, 181, 197, 239, 240, and 250 (orange) in D. The curved arrows illustrate that C_2A N248C-MTSL induces substantial PBEs on the bottom, middle, and top of the C_2B domain and that C_2B V304C-MTSL induces substantial PBEs on the top, middle, and bottom of the C_2A domain. The linker between the C_2 domains is represented by a dashed line.

studies that showed the orientation between the two domains was dynamic using EPR (Herrick et al., 2006) and single-molecule FRET (Choi et al., 2010; Vrljic et al., 2010). From the N248C mutant that attached MTSL to the bottom of the C_2A domain, we observed strong (<0.4) and medium (=0.4-0.6) PBEs for many cross-peaks at the bottom and middle portions of the C_2B domain (Figure 3.2A and B). This pattern of cross-peaks indicates mostly parallel and oblique orientations of C_2AB. Both of these orientations allow the simultaneous binding of a single C_2AB molecule through the top loops of both domains to a single membrane, and there is a range of acceptable conformations that would permit this possibility. However, we observed medium PBEs from the N248C mutant to the top of the C_2B domain (Figure 3.2A and B), indicating that a population of antiparallel C_2AB must also exist that gives rise to these effects. From the V304C mutant that attached MTSL to the top of the C_2B domain, we observed generally weaker PBEs with only one strong PBE at the top of the C_2A domain. The V304 residue is at the very tip of the Ca^{2+} binding loops on the C_2B domain, so it probably is not close enough to have larger effects on residues of the C_2A domain much of the time. However, we still observed medium PBEs to the top, middle, and bottom of the C_2A domain from the V304C mutant (Figure 3.2C and D), consistent with the results obtained with the N248C mutant. These results confirm that a substantial population of antiparallel C_2AB molecules exists when synaptotagmin-1 binds to membranes. We cannot feasibly quantify the populations of the conformers through analysis of the PBE data due to the dynamic nature of the bound molecules, but our results are consistent with estimates from

NBD fluorescence data whereby a population of antiparallel C_2AB molecules allows the bottom of the C_2B domain to contact membranes directly (Seven et al., 2013).

3.4 Discussion

Synaptotagmin-1 can aggregate liposomes and chromaffin granules (Damer and Creutz, 1994), and C_2AB bound to Ca^{2+} can bridge two membranes, bringing them within 4 nm (Arac et al., 2006). These observations led to a model whereby synaptic vesicle fusion can be triggered by synaptotagmin-1 bringing the vesicle and plasma membranes together in a Ca^{2+}-dependent manner in coordination with the SNAREs . This model is supported by the finding that mutations of arginines in the bottom of the C_2B domain impair the ability of synaptotagmin to cluster liposomes, limits the ability to stimulate SNARE-dependent lipid mixing of reconstituted vesicles, and nearly completely abolishes Ca^{2+}-evoked neurotransmitter release (Xue et al., 2008). This model also supports the notion that C_2B can bridge membranes directly through the Ca^{2+}-binding loops at the top of the domain and other residues such as the arginines at the bottom of the domain. The role of the C_2A domain is questioned as it does not appear to be necessary for bringing together apposed membranes. We thus examined the relative orientations of C_2AB on membranes to determine if C_2A also functions to bridge membranes, as suggested previously by EPR (Herrick et al., 2009).

Analysis of our PBEs for C_2AB bound to nanodiscs (Figure 3.2) actually suggests that a majority of C_2AB molecules use the Ca^{2+}-binding loops on both domains to bind a single membrane. This feature is a logically expected considering the Ca^{2+}-binding loops

have a high affinity for membranes and the increase in local concentration of one domain binding to a membrane should increase the probability of the second domain binding to the same membrane. Only a small amount of molecules actually need to bind to apposed membranes as the surface area of two membranes that come close in space for fusion is also quite small. In addition, Syt1 C_2B is all that is necessary to directly bridge membranes, which could happen with the C_2A and C_2B domains either in antiparallel or parallel orientations. Estimates from NBD fluorescence suggest the antiparallel population is 5-10% or higher, even under conditions where liposomes do not clusters (Seven et al., 2013). This estimate is consistent with our measurement of PBEs on nanodiscs, as well as EPR data that showed the bottom of the C_2B domain was near the membrane surface and that a significant portion of the molecules had antiparallel conformations (Herrick et al., 2009). The EPR analysis did suggest that C_2AB had a predominantly antiparallel orientation, which may be inconsistent with the NBD and PRE data. However, the populations cannot be reliably determined by EPR, NBD fluorescence, or PRE data and the experimental conditions and concentrations differed, so the findings could be in agreement. Regardless of the percentages, a significant portion of the C_2AB molecules do have an antiparallel orientation and can bind to apposed membranes and bridge liposomes through their Ca^{2+}-binding loops alone. We propose that C_2AB molecules can bind in a parallel or antiparallel fashion to liposomes, allowing for membrane bridging either through the C_2B domain directly or through both the C_2A and C_2B domains (Figure 3.3).

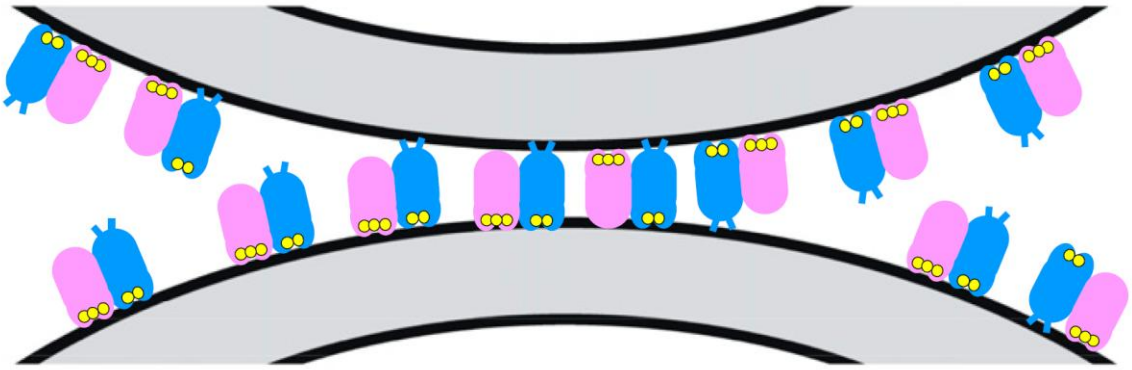

Figure 3.3 Model of synaptotagmin-1 membrane bridging. The C_2A (pink) and C_2B (blue) domains can be in either antiparallel or parallel orientation in the presence of the Ca^{2+} (yellow circles), able to associate with either membrane, although the antiparallel conformation has a smaller population. R398 and R399 on the C_2B domain (blue sticks) can interact with the membranes in either orientation when the membranes are close in space or in an antiparallel orientation when the membranes are further apart.

We conclude from these data that despite local concentration favoring binding to a single membrane, synaptotagmin can bind to two membranes in an antiparallel fashion. The function of this binding is not known as C_2B can also bridge membranes without C_2A. Presumably the function would be involved with the Ca^{2+} release step of neurotransmitter release as the Ca^{2+}-binding loops are needed to bridge membranes through two domains. Vesicle docking brings membranes into close space prior to this step in neurotransmitter release (Sudhof, 2004), but Syt1 is expected to bring the membranes even closer together during fusion. In addition, the bridging of membranes may be important for subsequent rounds of exocytosis, helping to dock new synaptic vesicles as a form of synaptic plasticity. The C_2A domain may help to bridge membranes that are not yet close enough for direct interactions through the C_2B alone. The C_2A domain may also play addition roles unrelated to vesicle tethering during fusion such as destabilizing membranes (Martens et al., 2007). Nevertheless, further research will be needed to investigate the function in neurotransmitter release behind synaptotagmin bridging membranes through two domains.

Chapter 4 Analysis of the Synaptotagmin-1/SNARE Complex via Paramagnetic Broadening in Solution and on Nanodiscs

4.1 Introduction

Neurotransmitter release through Ca^{2+}-evoked synaptic vesicle exocytosis is a tightly regulated process controlled exquisitely by protein machinery (Brunger et al., 2009; Jahn and Fasshauer, 2012; Rizo and Sudhof, 2012). Critical parts of this machinery include the SNARE proteins synaptobrevin, syntaxin-1, and SNAP-25, which form a tight four helix bundle (Poirier et al., 1998; Sutton et al., 1998) to bring together the vesicle and plasma membranes (Hanson et al., 1997). Another critical protein is synaptotagmin-1 (Syt1), which is composed of two C_2 domains (C_2A and C_2B) that bind three and two Ca^{2+}, respectively (Fernandez et al., 2001; Shao et al., 1998; Sutton et al., 1995; Ubach et al., 1998), to enable phospholipid binding (Chapman and Davis, 1998; Zhang et al., 1998). Syt1 mutants altering Ca^{2+}-dependent phospholipid binding correspondingly increase or decrease neurotransmitter release efficiency (Fernandez-Chacon et al., 2001; Rhee et al., 2005), demonstrating that Syt1 is the putative Ca^{2+} sensor for release.

The C_2B domain of Syt1 can bridge membranes through its Ca^{2+} binding loops and two arginines residues on the opposite side of its β-sandwich structure (Arac et al., 2006), which may partly underlie its primary role in neurotransmitter release (Mackler and Reist, 2001). The C_2B domain is also of primary importance for the interaction of Syt1 with the SNARE complex (Dai et al., 2007; Zhou et al., 2013a), which may be

essential to its function. Syt1-SNARE interactions are thought to be important for neurotransmitter release, as Ca^{2+} binding through Syt1 needs to be coupled to the actions of the SNARE complex at the moment of synaptic vesicle exocytosis. Many types of interactions between Syt1 and SNAREs either assembled in or disassembled from the SNARE complex have been reported (Rizo et al., 2006), and it is unclear which interactions are relevant for the late step of release.

Here we describe an attempt to characterize the interaction between Syt1 and the SNARE complex using the paramagnetic tag MTSL to obtain intermolecular restraints. Through this approach, we find that the middle of the SNARE complex C-terminal half on the syntaxin and SNAP-25 N-terminal SNARE domains is near to the interaction site for the Syt1 C_2B domain. However, this method largely fails as multiple interactions between the SNARE complex and Syt1 are present under the same conditions, preventing us from obtaining a defined molecular structure that would allow characterization of the primary interaction mode. In addition, we show that analysis of the Syt1-SNARE complex on nanodiscs is feasible, although the interactions we observe on these membranes with Ca^{2+} mirror the ones we observe in solution without Ca^{2+}.

4.2 Material and Methods

4.2.1 Expression and Purification of Proteins

The SNARE motif fragments of rat synaptobrevin 2 (residues 29-93), human-25 (residues 11-82 and 141-203) and rat syntaxin-1A (residues 191-253) in a pGEX-KT vector, and rat Syt1 C_2B (residues 271-421), C_2B (R398Q,R399Q mutant), and C_2AB

(residues 131-421 and 140-421) in a pGEX-KG vector were expressed and purified as previously described (Arac et al., 2006; Chen et al., 2002; Zhou et al., 2013a). Single-cysteine SNARE mutant constructs were prepared through site-directed mutagenesis by PCR with customized primers. The proteins were expressed in *Escherichia coli* BL21(DE3) cells in LB broth for unlabeled proteins. M9 minimal expression media was used to produce uniformly labeled ^{13}C, ^{15}N proteins with $^{13}C_6$-glucose as the sole carbon source (3 g/L) and $^{15}NH_4Cl$ as the sole nitrogen source (1 g/L). M9 expression media in 99.9% D_2O with ^{2}H,^{12}C-glucose as the sole carbon source (3 g/L) and $^{15}NH_4Cl$ as the sole nitrogen source (1 g/L) was used to produce perdeuterated proteins. ILVM methyl-labeled proteins were produced by adding [3,3-$^{2}H_2$] ^{13}C-methyl alpha-ketobutyric acid (80 mg/L), [3-^{2}H] ^{13}C-dimethyl alpha-ketoisovaleric acid (80 mg/L), and ^{13}C-methyl methionine (250 mg/L) (Cambridge Isotope Laboratories) to the perdeuterated protein cultures 30 minutes prior to Isopropyl β-D-1-thiogalactopyranoside (IPTG) induction (Gelis et al., 2007; Goto et al., 1999). SNARE complex assembly was achieved by mixing the SNARE domains in equimolar ratio as previously described (Chen et al., 2002; Zhou et al., 2013a), except that the reaction was incubated at room temperature while rotating during assembly.

4.2.2 Paramagnetic Labeling of SNAREs

To label SNARE cysteine mutants with paramagnetic tags, the protein was treated with 10 mM DTT, which was subsequently removed by gel filtration chromatography on a Superdex S75 column in 25 mM Tris-HCl pH 7.4, 150 mM NaCl. For MTSL labeling,

the protein was concentrated to 40-60 μM and incubated overnight at 4°C with a 10-fold molar excess of MTSL from a 40 mM stock in dimethyl sulfoxide (Seven et al., 2013). The excess MTSL was removed by buffer exchange in the gel filtration buffer using a 3-kDa molecular weight cutoff filter before being assembled into the SNARE complex. The SNARE complex was then buffer exchanged into the NMR buffer with a 10-kDa molecular weight cutoff filter. KSCN salt was used in some experiments to limit non-specific interactions and prevent precipitation of the synaptotagmin-SNARE complex in the presence of calcium. The MTSL nitroxide radical was reduced when needed by addition of 1 mM ascorbic acid and 1 mM sodium dithionite from a 100 mM stock adjusted to pH 7.4 prepared immediately before use.

4.2.3 Preparation of Nanodiscs Containing the SNARE Complex

Full-length synaptobrevin was first incorporated into nanodiscs, similar to as previously described (Banerjee et al., 2008; Brewer et al., 2011). Syb 29-116 was combined with a mixture of lipid, ApoA1, sodium cholate, and n-octyl-β-D-glucopyranoside (β-OG). The lipid:ApoA1:syb ratio was 120:2:1, prepared from stock concentrations of 13 mM, 200 μM, and 110 μM, respectively, while the sodium cholate and β-OG were added to a 1% final concentration from 10% stocks. After vortexing the mixture, it was left at room temperature for 30 minutes without disturbance. The mixture was passed over Extracti-Gel D resin (Pierce) in a 4-cm-high column to remove the detergent and form the nanodiscs. The other SNAREs were added in equimolar ratio and protease inhibitors (Roche) were added before allowing the reaction to assemble

overnight while rotating at 4°C. A Superdex-200 Hiload 16⁄60 column (GE Healthcare) in NMR buffer was used to remove any liposomes and further purify the nanodiscs. The sample was then concentrated to the desired concentration using a 30-kDa molecular weight cutoff filter.

4.2.4 NMR Spectroscopy

Varian INOVA spectrometers equipped with cold probes operating at 600 or 800 MHz were used to acquire all NMR spectra at 25°C. ^{1}H-^{13}C HMQC and ^{1}H-^{15}N HSQC TROSY spectra were obtained as detailed in the figure legends using 10-100% D_2O. The data were processed using NMRPipe (Delaglio et al., 1995) and analyzed using NMRView (Johnson and Blevins, 1994).

4.3 Results and Discussion

4.3.1 The C_2B Domain of Synaptotagmin Binds to the Middle of the SNARE Complex C-terminal Half Near the Syntaxin and SNAP-25 N-terminal Domain

Due to the aggregation and non-specific interactions of Syt1 with the SNARE complex even at moderate protein concentrations (Dai et al., 2007), we were unable to obtain the structure of the Syt1-SNARE complex by traditional NMR methods such as measuring nuclear Overhauser effects (NOEs) between proteins. Instead, we turned to the use of paramagnetic broadening effects (PBEs) that can be used to measure distances of up to 25 Å between proteins, not requiring large protein concentrations (Battiste and Wagner, 2000; Card et al., 2005).

To implement PBEs, we attached the nitroxide radical MTSL to various locations on the SNARE complex, especially along the C-terminus and middle of the SNARE complex where binding was predicted previously (Dai et al., 2007; Kim et al., 2012; Rickman et al., 2004). We chose six total sites for attachment on the SNARE complex on the various SNARE domains by making single cysteine point mutations to react with the MTSL tag (Figure 4.1A). Due to the large size and aggregation prone nature of the SNARE complex with Syt1 C_2AB, many residues are broadened completely using ^{1}H-^{15}N TROSY HSQC acquisition with perdeuterated proteins (Dai et al., 2007). Therefore, we labeled Syt1 C_2AB on Ile, Leu, and Val methyl groups with a perdeuterated background and recorded ^{1}H-^{13}C HMQC spectra that are highly sensitive even for large macromolecules (Ruschak and Kay, 2010).

We found the Syt1-SNARE complex would precipitate in the presence of Ca^{2+}, even at 5 μM protein concentrations, so we obtained our spectra in the presence of 1 mM EDTA. The affinity of Syt1 for the SNARE complex is lower in the absence of Ca^{2+} (Zhou et al., 2013a), so in attempt to saturate SNARE complex binding for Syt1 to a reasonable degree, we added 64 μM MTSL-labeled SNARE complex to 32 μM ^{2}H-ILV-$^{13}CH_3$-C_2AB and acquired ^{1}H-^{13}C HMQC spectra of the samples before and after reducing the nitroxide radical. We first noticed that PBEs induced by MTSL attached to the SNARE complex on Syt1 were seen primarily on resonances on the C_2B domain (Figure 4.1B; black cross-peaks without corresponding red cross-peaks), while the C_2A domain resonances were largely unaffected (Figure 4.1B; black cross-peaks with corresponding red cross-peaks), agreeing with the severe broadening seen only on the

C_2B domain previously just due to binding (Dai et al., 2007). From this result, we concluded that interactions in Syt1-SNARE complexes are mostly mediated by the Syt1 C_2B domain.

In attempts to determine the approximate binding region of Syt1 on the SNARE complex, we compared the PBEs seen on the C_2B domain for the various cysteine mutants on the SNARE complex used as attachment sites for MTSL. To analyze the mutants, we determined the intensity of the individual cross-peaks before reduction divided by the cross-peak intensity after reduction (I_{ox}/I_{red} ratio). We then mapped these intensities on a ribbon diagram of Syt1 C_2B to visualize the results (Figure 4.1C). Unexpectedly, Q197C on the C-terminal SNAP-25 domain (SNC Q197C-MTSL) generated the least broadening on C_2B, as this region had previously been hypothesized to mediate Syt1 binding (Dai et al., 2007). SNC Q187C-MTSL in the SNARE complex showed more broadening on the Syt1, and syb A72C-MTSL exhibited even more broadening, but these mutants still had small amounts of broadening compared to others. Compared to syb A72C-MTSL, syb 61C-MTSL had similar, but slightly more broadening, so the C_2B domain likely to binds somewhere a similar distance from these residues. Syx H239C-MTSL and N65C on the N-terminal SNAP-25 domain (SNN N65C-MTSL) had the most broadening of all six mutants. Surprisingly, for these two mutants >10 methyl groups were broadened nearly beyond detection (<0.15 I_{ox}/I_{red} ratio), implying that several methyl groups come very close to the MTSL nitroxide radical for these samples and the C_2B bound near the middle of the SNARE complex C-terminal

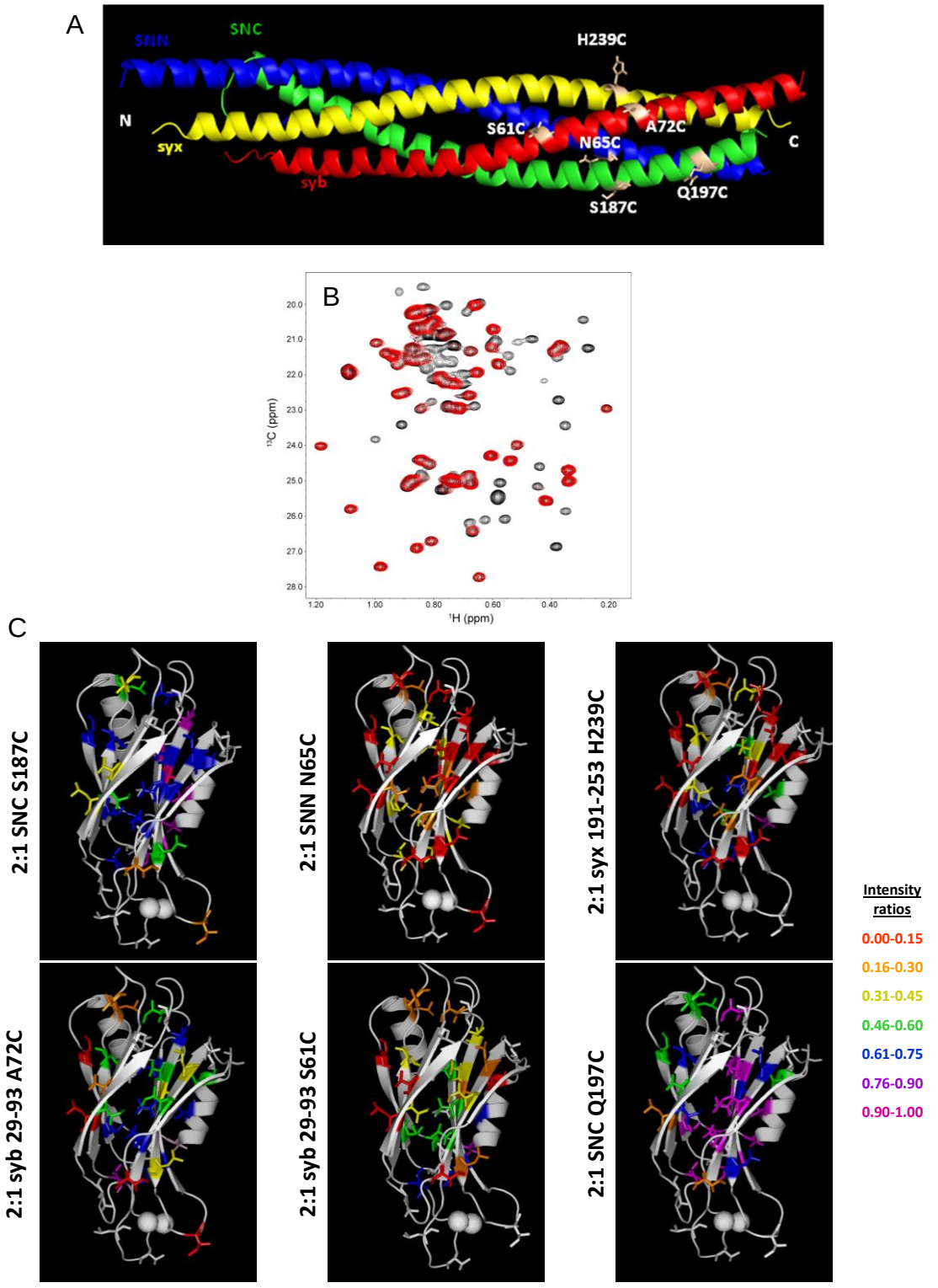
A
SNN
SNC
H239C
N
S61C
A72C
N65C
C
syx
syb
Q197C
S187C
B
^{13}C (ppm)
^{1}H (ppm)
C
2:1 SNC S187C
2:1 SNN N65C
2:1 syx 191-253 H239C
2:1 syb 29-93 A72C
2:1 syb 29-93 S61C
2:1 SNC Q197C
Intensity ratios
0.00-0.15
0.16-0.30
0.31-0.45
0.46-0.60
0.61-0.75
0.76-0.90
0.90-1.00

Figure 4.1 Paramagnetic broadening from MTSL-labeled SNARE complexes on the Syt1 C_2AB in solution. (A) Ribbon diagram of the SNARE complex (syntaxin, yellow; synaptobrevin, red; SNAP-25 N-terminal and C-terminal SNARE motifs, blue and green, respectively). The residues individually mutated to cysteine for MTSL attachment are shown in wheat. (B) Leu,Val region of the ^{1}H-^{13}C HMQC spectra of 32 µM ^{2}H-ILV-$^{13}CH_3$-C_2AB in the presence of 64 µM SNARE complex SNN N65C-MTSL before (red contours) or after (black countours) reduction of the tag by the addition of 1 mM ascorbic acid and 1 mM sodium dithionite. The buffer used was 25 mM Tris pH 7.4, pD 7.8, 125 mM NaCl, 1 mM EDTA, 100% D_2O. (C) Ribbon diagrams of the Syt1 C_2B domain highlighting the oxidized to reduced ratios (I_{ox}/I_{red}) for the Ile, Leu, and Val methyls of the various SNARE complex cysteine mutants used (2:1 ratio of 64 µM SNARE complex to 32 µM C_2AB). The I_{ox}/I_{red} ratios are visualized with different colors [I_{ox}/I_{red} = <0.15 (red), 0.16-0.30 (orange), 0.31-0.45 (yellow), 0.46-0.60 (green), 0.61-0.75 (blue), 0.76-0.90 (purple), >0.90 (pink)].

half, most likely on syx and/or SNN. However, this conclusion cannot be considered definitive due to the multiplicity of binding modes that may bias towards interaction modes that are closer to the attached nitroxide tag, especially for the cysteine mutants exhibiting strong broadening.

4.3.2 The Synaptotagmin-1/SNARE Complex Has Two or More Distinct Structural States

Continuing with our analysis, we wanted to determine the region of C_2B that bound to the SNARE complex. To achieve this goal, we would look to see which residues are most broadened on the C_2B domain, which could then be manually oriented towards that cysteine mutant on the SNARE complex. Through the use of several mutants we could thereby "lock in" the position of C_2B on the SNARE complex manually, and then further computationally.

Looking at the data for mutants furthest away from the C_2B binding site, SNC Q197C-MTSL and SNC S187C-MTSL, residues in the Ca^{2+} binding loops were the most broadened, with residues on the covex β-sheet also having clear broadening (Figure 4.1A). Therefore, it appeared as if the convex face of the C_2B domain may face the C-terminus of the SNARE complex with the top Ca^{2+} binding loops even closer to the C-terminus. However, looking at results from attaching MTSL to the other positions on the SNARE complex, especially syx H239C-MTSL and SNN N65C-MTSL, a large number of residues are severely broadened severaly due to the tag ($I_{ox}/I_{red} < 0.15$). These residues, must come close to the MTSL label (<10 Å) despite being distributed

throughout the C_2B domain that is 40 Å in its longest dimension. Therefore, we can conclude that there are two or more structural states of the Syt1-SNARE complex.

4.3.3 The Synaptotagmin-1/SNARE Complex Has Similar Structure Whether in Solution or on Synaptobrevin Anchored Nanodiscs

To see the influence of membranes and Ca^{2+} on the structure of the SNARE complex, we attempted to acquire spectra of the Syt1-SNARE complex with the syb transmembrane domain anchored in nanodiscs. As nanodiscs are several hundred kDa in size, we also increased the protein concentrations used. First, we added 180 µM ^{2}H-ILV-$^{13}CH_3$-C_2AB 141-421 C277S to 350 µM synaptobrevin-anchored SNARE complex on nanodiscs with 1 mM EDTA. Compared to the ^{1}H-^{13}C HMQC spectrum of C_2AB in solution, several cross-peaks were missing after adding the SNARE complex nanodiscs (Figure 4.2A), especially from the C_2B domain, but nevertheless, some cross-peaks still remained. However, upon adding an effective concentration of 1 mM $CaCl_2$, the Syt1 cross-peaks almost completely disappeared, even from the C_2A domain (Figure 4.2B), which was similarly seen when a construct of the C_2B domain without the C_2A domain was used in a similar sample (Figure 4.2C). Note that we did see precipitation upon adding Ca^{2+}, but still had enough protein left in solution to restore the spectra after adding saturating amounts of EDTA again, so this precipitation is not the reason for the cross-peak disappearance. The presence of membranes presumably helps to limit precipitation unlike in solution where the protein loss would be more significant.

We thought that the clustering of membranes by the C_2B domain and/or the interaction of the SNARE complex with multiple sites of the C_2B domain may be the reason for the severe broadening seen both with and without Ca^{2+} in these spectra. Therefore, we used C_2B R398Q,R399Q, previously designed to prevent liposome clustering (Arac et al., 2006) but also prevents SNARE complex aggregation (Zhou et al., 2013a), to obtain our spectra. We surprisingly found that we could see the signals for this mutant at a protein concentration of only 90 μM in the presence of Ca^{2+} with the SNARE complex on nanodiscs. We acquired ^{1}H-^{13}C HMQC spectra of ^{2}H-ILV-$^{13}CH_3$-C_2B R398Q,R399Q with syx H239C-MTSL SNARE complex on nanodiscs in the presence of Ca^{2+} before and after reduction of the tag, and we were able to observe PBEs for the cross-peaks of several methyl groups (Figure 4.2D).

To see how these results compared to those obtained in solution, we again mapped the obtained PBEs obtained on nanodiscs onto the C_2B domain. We then compared those PBEs to the analogous ones seen in solution for the same H239C mutant obtained with 15 μM SNARE complex and 20 μM C_2AB with EDTA. Despite the differences in constructs used and presence of membranes and Ca^{2+}, the patterns of PBEs match remarkably well. The one key difference is that there appears to be more broadening for some residues for the nanodiscs data. This change likely arises as the PBEs increase as the molecular size of the system increases (Battiste and Wagner, 2000), or from higher protein saturation on nanodiscs. Despite this difference, the interaction of C_2B with the SNARE complex appears to be the same whether on nanodiscs or in solution, at least considering the cross-peaks that we could observe.

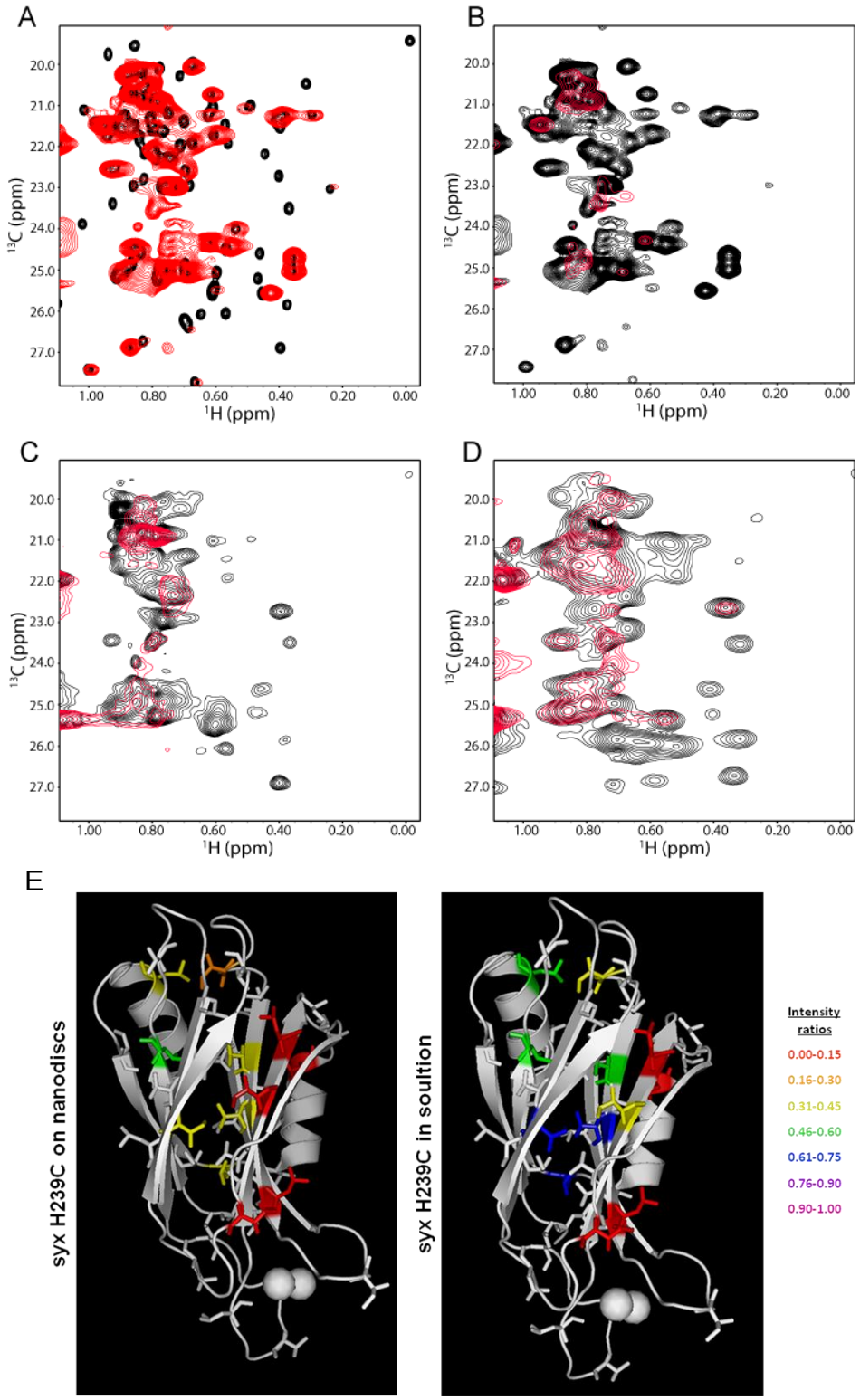
A
B
C
D
E
^{13}C (ppm)
^{1}H (ppm)
syx H239C on nanodiscs
syx H239C in soultion
Intensity ratios
0.00-0.15
0.16-0.30
0.31-0.45
0.46-0.60
0.61-0.75
0.76-0.90
0.90-1.00

Figure 4.2 Analysis of Syt1 with SNARE complex anchored to nanodiscs. (A) Leu,Val region of the ^{1}H-^{13}C HMQC spectra of 32 μM ^{2}H-ILV-$^{13}CH_3$-C_2AB 141-421 C277S (black countours) and 180 μM ^{2}H-ILV-$^{13}CH_3$-C_2AB 141-421 C277S in the presence of 350 μM synaptobrevin anchored SNARE complex on nanodiscs with 1 mM EDTA (red contours). The buffer used was 25 mM Tris-HCl pH 7.4, 125 mM NaCl, 100% D_2O for all spectra. (B) 180 μM ^{2}H-ILV-$^{13}CH_3$-C_2AB 141-421 C277S in the presence of 350 μM synaptobrevin anchored SNARE complex on nanodiscs with 1 mM EDTA (black contours) and 1 mM $CaCl_2$ (red contours) (C) 200 μM ^{2}H-ILV-$^{13}CH_3$-C_2B C277S in the presence of 350 μM synaptobrevin anchored SNARE complex on nanodiscs with 1 mM EDTA (black contours) and 1 mM $CaCl_2$ (red contours). (D) 90 μM ^{2}H-ILV-$^{13}CH_3$-C_2B R398Q,R399Q in the presence of 110 μM synaptobrevin anchored SNARE complex syx H239C-MTSL on nanodiscs with 1 mM $CaCl_2$ before (red contours) or after (black countours) reduction of the tag by the addition of 1 mM ascorbic acid and 1 mM sodium dithionite. (E) Ribbon diagrams of the Syt1 C_2B domain highlighting the I_{ox}/I_{red} for the Ile, Leu, and Val methyls for the syx H239C mutant attached to MTSL either on nanodiscs [left, from (D)] or in solution (right, 15 μM SNARE complex with 20 μM ^{2}H-ILV-$^{13}CH_3$-C_2AB). The I_{ox}/I_{red} ratios are visualized with different colors as in Figure 1 [I_{ox}/I_{red} = <0.15 (red), 0.16-0.30 (orange), 0.31-0.45 (yellow), 0.46-0.60 (green), 0.61-0.75 (blue), 0.76-0.90 (purple), >0.90 (pink)].

4.3.4 Nitroxide Paramagnetic Broadening is Largely Unsuitable for Solving the Synaptotagmin-1/SNARE Complex and Other Multistate Protein Complexes

Because of the detection of multiple binding sites in our initial experiments, we sought conditions where we could resolve a single binding site. We first lowered concentrations and used a lower ratio of SNARE complex to Syt1 in attempt to limit interactions that may lead us to detect non-specific binding sites using buffer conditions identical to those in Figure 4.1, but lowering the C_2AB concentration to 20 μM and SNARE complex concentration to 15 μM. Despite using lower concentrations, we still readily detected multiple binding sites to the same degree as we did at higher concentrations (Figure 4.3A). The PBEs we saw were smaller overall but were generally scaled down versions from the higher concentrations with no improvement in specificity of broadening. However, the fact that the PBEs were smaller is a slight progression as it demonstrates that the broadening effects can be influenced by experimental conditions and are not independent of the degree of saturation.

We continued to search for conditions where we could work with the proteins in solution in the presence of Ca^{2+} to increase affinity and possible specificity. We finally found conditions to do so by adding nine residues to the N-terminus of the Syt1 C_2AB construct (residues 131-421 rather than 140-421) and using KSCN salt rather than NaCl salt. The added residues at the N-terminus are a glutamate, glutamate, lysine repeat that increases solubility, and SCN^- is a chaotropic anion decreases non-specific interactions and increase solubility (Richens et al., 2009; Zhang and Cremer, 2006). We also labeled Syt1 131-421 C277A,K325C with MTSL in hopes to isolate one of the binding sites on

C_2B and find the precise SNARE complex binding site, rather than vice versa. We added 7 μM C_2AB K325C-MTSL to 34 μM SNARE complex and acquired a four series of ^{1}H-^{15}N TROSY HSQC spectra, one each for the oxidized and reduced samples of the individual $^{2}H,^{15}N$ SNARE domains. Despite using very low concentrations of the Syt1 with MTSL attached, using Ca^{2+} to increase specificity, and using KSCN to decrease non-specific interactions, we still readily detected two distinct binding sites on the SNARE complex where the I_{ox}/I_{red} were less than 0.40 (Figure 4.3B), with one binding site on SNC SNARE domain and one binding site on syx (note that these ratios are higher than the I_{ox}/I_{red} seen for the PBEs on C_2B due to the relatively very low concentration of the protein attached to MTSL used in this case). Surprisingly, we did not see much broadening on the SNN SNARE domain (all residues had an $I_{ox}/I_{red} > 0.70$), disagreeing with our earlier results (see above), but we did not verify the reproducibility of these data.

Even under these conditions that should heavily favor a specific binding site, we still managed to detect two binding sites on the SNARE complex. The highly charged nature of Syt1 and the SNARE complex should favor non-specific interactions and may exist at least partially as a multistate complex, hindering our efforts to solve individual complexes. In addition, the $1/r^6$ dependence of PBEs on the distance between the paramagnetic center and atomic nuclei highly weight lowly populated complexes that come close to the nitroxide radical, a feature generally applicable in the study of multistate protein complexes (Clore and Iwahara, 2009). Together, these features prevent us from accurately determining a static structure of the Syt1-SNARE complex using a nitroxide tag.

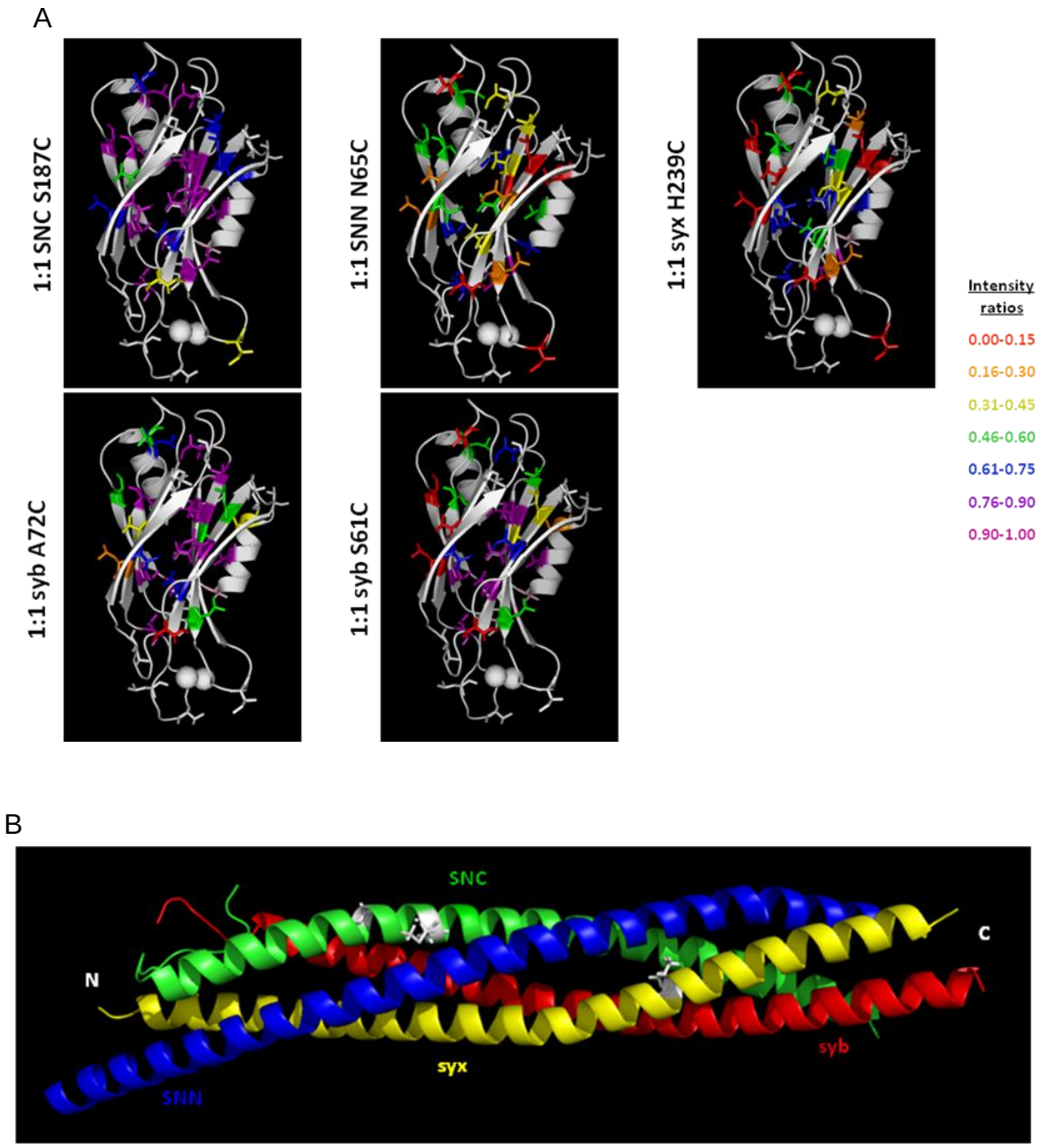

Figure 4.3 Improved conditions still yield multiple binding sites for the Syt1-SNARE complex. (A) Ribbon diagrams of the Syt1 C_2B domain highlighting the oxidized to reduced ratios (I_{ox}/I_{red}) for the Ile, Leu, and Val methyls of the various SNARE complex cysteine mutants as seen in Figure 4.1 using the same proteins and buffer, but with lower

protein concentrations (~1:1 ratio of 15 μM SNARE complex to 20 μM ^{2}H-ILV-$^{13}CH_3$-C_2AB). The I_{ox}/I_{red} ratios are visualized with different colors [I_{ox}/I_{red} of <0.15 (red), 0.16-0.30 (orange), 0.31-0.45 (yellow), 0.46-0.60 (green), 0.61-0.75 (blue), 0.76-0.90 (purple), >0.90 (pink)]. (B) Ribbon diagram of the SNARE complex with residues broadened to an I_{ox}/I_{red} <0.40 shown in white. ^{1}H-^{15}N TROSY HSQC spectra of 34 μM SNARE complex samples ^{2}H,^{15}N-labeled at syntaxin-1, synaptobrevin, SNAP-25 N-terminal, and SNAP-25 C-terminal SNARE motifs were individually recorded with 7 μM Syt1 C_2AB 131-421 C277A,K325C-MTSL before and after reduction in the presence of Ca^{2+}. The buffer composition used was 25 mM D-Tris-DCl pH 7.4, 125 mM KSCN, 1 mM $CaCl_2$, 10% D_2O.

4.4 Discussion

As the complexity of reconstituted systems has increased in over the past few years, structural tools have also been developed to perform analyses of these systems. Here we studied the structure of the Syt1-SNARE complex by NMR using the paramagnetic tag MTSL as well as membrane nanodiscs. MTSL has been increasingly used in NMR as a structural restraint to describe protein complexes (Card et al., 2005; Schilder et al., 2014). Nanodiscs have also been used recently to characterize the structure of membrane associated proteins (Brewer et al., 2011; Hagn et al., 2013).

By attaching MTSL to various locations along the SNARE complex, we were able to approximate the binding site of the C_2B domain. We first were able to ascertain that the C_2A domain had very limited binding to the SNARE complex as we expected from previous analysis (Dai et al., 2007). We then found that the C_2B domain may bind near the middle of the SNARE complex C-terminal half on syntaxin-1 and/or the SNAP-25 N-terminal domain. This result conflicted with the finding that mutations in the far C-terminal end of the SNARE complex for residues D186, D193 on the SNAP-25 C-terminal domain had more of an effect on binding than mutations in the middle of the SNARE complex for residues D51, E52, and E55 on the SNAP-25 N-terminal domain (Dai et al., 2007). Instead, our findings likely favor studies that found the latter residues to be important for binding (Kim et al., 2012; Rickman et al., 2004), as well as a single-molecule study that placed the C_2B domain near the same location (Choi et al., 2010). MTSL attached to the far C-terminus of the SNARE complex (e.g. SNC Q197C) produced the least broadening on Syt1 cross-peaks, while mutations further towards the

middle of the SNARE complex (e.g. syx H239C and SNN N65C) produced strong broadening. The presence of membranes as well as various experimental conditions and constructs used may be critical for the differences in these results. Note that mutations in residues D179 and D186 of SNAP-25 did not have an effect on binding in the presence of membranes (Kim et al., 2012), but that D186 and D193 were not examined as well in the same study. Binding of Syt1 to the far C-terminal end of the SNARE complex is still not ruled out, but C_2B binding to closer to the middle of the SNARE complex are more favored by our results. However, our results should also be taken with caution due to detection of lowly populated states in this study.

Our analysis also revealed the Syt1 C_2B domain has severe broadening in several distinct locations when interacting with MTSL-labeled SNARE complex. Two reasons likely give rise to this result. Firstly, the SNARE complex is largely composed of acidic residues and Syt1 is largely composed of basic residues, so multiple types of electrostatic interactions are likely to occur between these proteins (Zhou et al., 2013a). Secondly, due to the $1/r^6$ dependence of PBEs on the distance between the paramagnetic center and atomic nuclei, even very lowly populated states can lead to large broadening of resonances if residues come into close contact with the paramagnetic probe. For this reason, MTSL is often used to probe states that are lowly populated (Clore and Iwahara, 2009), rather than obtain single structures for protein complexes. These problems can become exacerbated even further as the MTSL probe is largely exposed and able to come close to surface residues that may interact non-specifically for a short time with the probe. In addition, the charged nature of Syt1 and the SNARE complex facilitate very

lowly populated states that are readily detected by the probe. Even under conditions of low concentrations and using the chaotropic anion SCN^-, these problems still arise and make the use of PBEs largely unsuitable for specific structural analysis of the Syt1-SNARE complex.

To determine the effect of membranes and Ca^{2+} on the Syt1-SNARE complex binding mode, we also explored the use of SNARE complex anchored to nanodiscs. We were especially interested to see if these proteins on membranes would be limited in interactions, and thereby largely eliminate the problems we found with non-specific interactions. Interestingly, we found that using C_2AB and C_2B constructs were mostly unsuitable for this analysis, even in the absence of Ca^{2+}, as the cross-peaks from the C_2B domain were heavily broadened in the presence of SNARE complex anchored to nanodiscs through the synaptobrevin transmembrane domain. The aggregation of the SNARE complex through multiple non-specific interactions we saw in our analysis in solution may mediate this broadening. Mutating residues R398 and R399 of the C_2B domain, known to cause aggregation of the SNARE complex (Zhou et al., 2013a), alleviated this problem, and we could acquire data even in the presence of Ca^{2+}. As these residues also are necessary for clustering liposomes (Arac et al., 2006), membrane interactions may also be the reason for cross-peak broadening using the wild type Syt1 constructs.

The PBEs we saw on Syt1 C_2AB in solution with EDTA and on Syt1 C_2B R398Q,R399Q on nanodiscs with Ca^{2+} matched well for the resonances we could observe in both sets of spectra, implying that the presence of membranes and Ca^{2+} do not affect

the structure of the Syt1-SNARE complex. The C_2B mutant may be partially responsible for this similar result, especially due to the loss of interactions with membranes that may affect binding modes between the Syt1-SNARE complex. However, this work provides evidence that the structures in solution and on membranes are likely similar.

Chapter 5 Dynamic Synaptotagmin-1-SNARE Complex Structure in Solution

5.1 Introduction

A sophisticated protein machinery governs Ca^{2+}-triggered synaptic vesicle exocytosis to control release of neurotransmitters (Brunger et al., 2009; Rizo and Sudhof, 2012). The SNAREs synaptobrevin, SNAP-25, and syntaxin-1 are central components of this machinery that bring the vesicle and plasma membranes together (Hanson et al., 1997) by forming a tight four-helix bundle (Poirier et al., 1998; Sutton et al., 1998) and are key for membrane fusion. Synaptotagmin-1 (Syt1) executes Ca^{2+} triggered fast release (Fernandez-Chacon et al., 2001) through its cytoplasmic region composed of two C_2 domains. The loops at the top of the C_2A and C_2B domains, β-sandwich structures, can bind multiple Ca^{2+} ions (Fernandez et al., 2001; Sutton et al., 1995; Ubach et al., 1998), and these loops can bind membranes in a Ca^{2+}-dependent matter that is key for Syt1 function (Fernandez-Chacon et al., 2001). The major role in release is played by Ca^{2+} binding to the C_2B domain, possibly because the C_2B domain can bridge two membranes through its top Ca^{2+} binding top loops and bottom loops that include two arginines (R398 and R399) (Arac et al., 2006; Xue et al., 2008). The SNARE proteins also interact with Syt1 (Bennett et al., 1992; Gerona et al., 2000; Li et al., 1995), which is likely involved in the Ca^{2+}-triggered release step of synaptic vesicle exocytosis (Pang et al., 2006). Syt1 and the SNAREs also act in tight concert with complexins (Giraudo et al., 2006; Schaub et al., 2006; Tang et al., 2006), small soluble proteins that can both inhibit and activate neurotransmitter release (Huntwork and Littleton, 2007; Maximov et

al., 2009; Reim et al., 2001). The central α-helix of complexin binds to the center of the SNARE complex (Chen et al., 2002). This central helix is preceded by an accessory α-helix that has an inhibitory function in release (Maximov et al., 2009; Xue et al., 2007), likely resulting from electrostatic repulsion with negative charges in the membrane (Trimbuch et al., 2014).

Many advances have been made in recent years, including the reconstitution of eight central proteins of the release machinery in synaptic vesicle fusion (Ma et al., 2013), but how these components actually trigger release is still unclear. These questions remain in part because high-resolution structures of Syt1-SNARE complexes have not been determined that may help to elucidate how Syt1 and the SNAREs are functionally coupled and how Syt1 and complexin work together in neurotransmitter release. Due to being highly charged, many types of Syt1-SNARE interactions have been reported (Rizo et al., 2006), and it is uncertain which are promiscuous and which are physiologically relevant. For example, Syt1 can interact with syntaxin-1 and SNAP-25 in the absence of other proteins (Bennett et al., 1992; Gerona et al., 2000; Li et al., 1995), but if these interactions occur in the same way on the SNARE complexes is unclear. In addition, interactions between Syt1-SNARE complex were reported to be mediated by distinct acidic regions of SNAP-25 (Rickman et al., 2006; Zhang et al., 2002). The polybasic region on the side of the Syt1 C_2B domain was found to be involved in SNARE complex binding in some studies (Dai et al., 2007; Lai et al., 2011; Rickman et al., 2006), while the bottom of the C_2B domain was positioned near the SNARE complex in a single-molecule FRET model (Choi et al., 2010). Another weaker binding site on the C_2B

domain near R398 and R399 may also be important for SNARE complex binding (Zhou et al., 2013a) , although this region contributed to aggregation when the proteins were in solution *in vitro*. Additional discrepancies arise from the fact that Syt1 and the complexin-I central and accessory α-helix fragment [Cpx(26-83)] can simultaneously bind the SNARE complex in solution, yet they compete for SNARE complex binding on membranes (Xu et al., 2013).

Here we describe the use of highly sensitive transverse relaxation optimized spectroscopy (TROSY)-based methods, designed for the study of large molecular proteins and protein complexes (Ruschak and Kay, 2010), in order to elucidate the structure of Syt1-SNARE complexes, a culmination of fifteen years of attempts. We focus on the use of paramagnetic probes to obtain long-distance intermolecular restraints that can be used to dock proteins together when structures of the individual binding partners are known (Otting, 2010). Through the use of pseudocontact shifts (PCSs) on Syt1 molecules induced by lanthanide probes attached on the SNARE complex, we were able to define a dynamic structure mediated by a polybasic region on the concave side of the Syt1 C_2B domain β-sandwich and two adjacent acidic regions from syntaxin-1 and SNAP-25 on the SNARE complex. Interactions within the Syt1-SNARE complex are strongly disrupted by double mutations in either these basic residues on Syt1 or acidic residues from syntaxin-1 or SNAP-25 at the binding site in this structure, but not in double mutations away from the binding site. Double mutations of basic residues on Syt1 at the polybasic region not oriented directly towards the SNARE complex have only slightly weakened interaction. These data together with the observation that Syt1

mutations have very similar effects on neurotransmitter release in neuronal cultures support the physiological relevance of the structure. The binding mode we observed can explain why Syt1 and CpxI(26-83) compete for SNARE complex binding on membranes, but not in solution, as the C_2B domain is in a ideal location on the SNARE complex to relieve the inhibition of release caused by the CpxI accessory α-helix. In addition, the C_2B domain is in a position to bridge the synaptic vesicle and plasma membranes upon Ca^{2+} influx to trigger membrane fusion in cooperation with SNAREs.

5.2 Material and Methods

5.2.1 Expression and Purification of Proteins

The SNARE motif fragments of rat synaptobrevin 2 (residues 29-93), human SNAP-25 (residues 11-82 and 141-203) and rat syntaxin-1A (residues 191-253) in a pGEX-KT vector, and rat Syt1 C_2B (residues 271-421), C_2B (R398Q,R399Q mutant), and C_2AB (residues 131-421 and 140-421) in a pGEX-KG vector were expressed and purified as previously described (Arac et al., 2006; Chen et al., 2002; Zhou et al., 2013a). Mutant constructs were prepared through site-directed mutagenesis by PCR with customized primers. The proteins were expressed in *Escherichia coli* BL21(DE3) cells in LB broth for unlabeled proteins. M9 minimal expression media was used to produce uniformly labeled ^{13}C, ^{15}N proteins with $^{13}C_6$-glucose as the sole carbon source (3 g/L) and $^{15}NH_4Cl$ as the sole nitrogen source (1 g/L). M9 expression media in 99.9% D_2O with ^{2}H,^{12}C-glucose as the sole carbon source (3 g/L) and $^{15}NH_4Cl$ as the sole nitrogen source (1 g/L) was used to produce perdeuterated proteins. ILVM methyl-labeled

proteins were produced by adding [3,3-$^{2}H_2$] ^{13}C-methyl alpha-ketobutyric acid (80 mg/L), [3-^{2}H] ^{13}C-dimethyl alpha-ketoisovaleric acid (80 mg/L), and ^{13}C-methyl methionine (250 mg/L) (Cambridge Isotope Laboratories) to the deuterated protein cultures 30 minutes prior to Isopropyl β-D-1-thiogalactopyranoside (IPTG) induction (Gelis et al., 2007; Goto et al., 1999). SNARE complex assembly was achieved by mixing the SNARE domains in equimolar ratio as previously described (Chen et al., 2002; Zhou et al., 2013a), but the reaction was incubated at room temperature while rotating during assembly.

5.2.2 Nuclear Magnetic Resonance (NMR) Spectroscopy

Varian INOVA spectrometers equipped with cold probes operating at 600 or 800 MHz were used to acquire all NMR spectra at 25°C. ^{1}H-^{13}C HMQC and ^{1}H-^{15}N HSQC TROSY spectra were obtained as detailed in the figure legends using 10% D_2O. The total times of acquisition varied from 4 to 56 hours. The data were processed using NMRPipe (Delaglio et al., 1995) and analyzed using NMRView (Johnson and Blevins, 1994). The buffer used for all PCS measurements was 25 mM Tris-HCl pH 7.4, 125 mM KSCN, 1 mM $CaCl_2$, 10% D_2O.

5.2.3 Lanthanide Labeling of SNAREs

To label SNARE cysteine mutants with paramagnetic tags, we treated the protein with 10 mM DTT which was subsequently removed by gel filtration chromatography in 25 mM Tris-HCl pH 7.4, 150 mM NaCl on a Superdex S75 column. The protein was

then concentrated to 30-100 µM and incubated 10 minutes at room temperature with 3-fold molar excess of the Dy^{3+}-C2 tag (Graham et al., 2011). After tag labeling, the other SNAREs were added for assembly and incubated while rotating overnight for assembly at room temperature. Sodium chloride was added to a final concentration of 1 M prior to mixing the SNAREs to prevent precipitation of syntaxin in the presence of lanthanide from the excess tag. When using ^{15}N or ^{13}C isotopically labeled SNAREs, unlabeled and lanthanide-tagged SNAREs were included in 40% excess as even a small percentage of free NMR labeled SNARE domain can give rise to signals much larger than assembled, lanthanide-tagged SNARE complex. Buffer exchange at 25°C into 25 mM Tris-HCl pH 7.4, 500 mM NaCl with a 10-kDa molecular weight cutoff filter was used to remove the excess tag and unassembled SNAREs from the SNARE complex. The SNARE complex was finally exchanged to 25 mM D-Tris-DCl pH 7.4, 125 mM KSCN, 1 mM $CaCl_2$, 10% D_2O. For Syt1 labeled samples, a 30 mM stock of TCEP was used to reduce the samples when needed by adding it for a final concentration of 0.3 mM (1 mM TCEP from a 100 mM stock was used for SNARE complex labeled samples as they were obtained at higher protein concentrations).

5.2.4 Pseudocontact Shift Measurement and Analysis

We acquired ^{1}H-^{15}N HSQC TROSY spectra to measure PCSs within the SNARE complex using 90 µM SNARE complex samples ^{2}H,^{15}N-labeled on SNAP-25 (residues 11-82) or syntaxin-1 SNARE motifs for the Dy^{3+}-C2 tag attached to residue 166 of SNAP-25 or ^{2}H,^{15}N-labeled on synaptobrevin or syntaxin-1 SNARE motifs for the Dy^{3+}-

C2 tag attached to residue 41 of SNAP-25. We determined the PCSs by measuring the chemical shift differences before and after removal of the Dy^{3+}-C2 tag by addition of a final concentration of 1 mM TCEP. NH groups within less than ~18 Å from the lanthanide were broadened beyond detection due to the low sensitivity of the spectra. The NH groups where we were able to measure PCSs are not close enough to be affected by a diamagnetic tag, so we could use the SNARE complex with the tag removed by TCEP to measure PCSs accurately. We estimated the error in PCSs by determining the reproducibility of chemical shifts measured over several repeated spectra. The PCSs measured within the SNARE complex were used to determine the $\Delta\chi$ tensors for the Dy^{3+}-C2 tag attached to residue 166 or 41 of SNAP-25 (referred to from here on as SC166Dy and SC41Dy, Figure 5.3) using the program Numbat (Schmitz et al., 2008). We determined how sensitive the tensor parameters were to small changes in the lanthanide center by recalculating the tensor after constraining the tensor center to random locations within 4 Å of the tensor center determined optimally when no tensor center restraints were used. The obtained tensors were then used to reanalyze fits between experimentally measured and calculated PCSs on the C_2B domain (e.g. Figure 5.5H,J).

^{1}H-^{13}C HMQC and ^{1}H-^{15}N HSQC TROSY spectra were used to measure PCSs from SC166Dy or SC41Dy on Syt1 fragments (C_2AB, C_2B, or C_2B R398Q,R399Q) for samples of 30 µM Syt1 and 30 µM (for either C_2B construct) or 20 µM (for C_2AB) SNARE complex tagged with lanthanide. All Syt1 fragments produced similar PCSs for the respective cysteine mutants, indicating they all yielded the same structural data, but

we used the C_2B R398Q,R399Q mutant (referred to as C_2B below) for analysis because it produced the best quality data and the PCSs were less likely to be changed by weaker binding modes. We estimated the binding to be about 66% saturated from ^{1}H-^{15}N HSQC titrations (e.g. Figure 5.1B), so we multiplied the PCSs measured by a factor of 1.5 for the full binding values. We did not use saturating conditions to avoid aggregation and precipitation. The PCSs were small and the digital resolution in the second dimension (^{13}C or ^{15}N) was much lower in our spectra, so we only used PCSs in the ^{1}H dimension.

We calculated the C_2B166 tensor (Figure 5.6A) with Numbat including only PCSs induced by SC166Dy on C_2B. We used Pymol to superimpose the C_2B166 and SC166 tensors (Figure 5.6B) by using the tensor orientations and coordinates from Numbat. The C_2B domain was manually rotated in Pymol around the z-axis of the SC166 tensor (Figure 5.6F) maintaining a similar orientation and distance of the domain from the SC166 tensor until the C_2B domain made van der Waals contact with the SNARE complex. The manual models for the SC166Dy and SC41Dy tensors (Figure 5.3E,F) were made in Pymol by manually rotating the C_2B domain on the SNARE complex to match the positive and negative PCS pattern on the C_2B domain to lobes of the SNARE complex while keeping the proteins in contact. We also used HADDOCK (Schmitz and Bonvin, 2011) to derive structures from the PCS measurements on the C_2B domain from SC166Dy and SC41Dy by scaling these measurements by a factor from 1 to 7 to account for the possibility that the preferred binding site is lowly populated. A factor of 5 was used to obtain the HADDOCK model for SC166Dy. We used Numbat to determine the calculated values for the models obtained by all of these methods (Schmitz et al., 2008).

We selected a structure representative of each of the 73 clusters resulting from MD simulations based on chemical shifts to see if the PCS measurements on the C_2B domain could be fit to an ensemble. We calculated the SC166Dy and SC41Dy tensor for each structure using the experimental PCSs on the SNARE complex only, then used these tensors to back-calculate the expected PCSs for each of the 73 structures on the C_2B domain. We used MATLAB to find the population weights of the 73 structures that would best fit the experimental C_2B data by minimizing the root mean square deviation between experimental and back-calculated PCSs. We performed the calculations separately for PCSs induced by SC166Dy and SC41Dy to get two separate correlations (Figure 5.8E, F).

The two structures from the ensemble of structures resulting from either the unrestrained or chemical shift restrained MD simulations that most closely resembled the 166 and 41 manual models were selected. We refer to these structures at the 166 and 41 MD models. The 166 MD model was taken from the ensemble of unrestrained MD simulations, and the 41 MD model was taken from the ensemble of chemical shift restrained MD simulations. We deposited these structures and the measured PCSs in the PDB.

5.2.5 Unrestrained Molecular Dynamics Simulations

We used the 166 HADDOCK model obtained with HADDOCK-PCS as starting coordinates for the C_2B-SNARE complex. A TIP3P water box with a minimum distance of 12 Å between the box edge and any protein atom was used to solvate the complex.

Sodium and chloride ions were added to keep the ionic concentration at 0.15 mol/L after the system was neutralized. Explicit solvent with the NAMD2.7 program (Phillips et al., 2005) under the Charm22 force field (MacKerell et al., 1998) was used to perform the MD simulations. The neutralized and solvated system was minimized with the protein restrained for 5000 steps followed by 5000 steps without restraints. The system was heated slowly for 500 ps to 300 K. To allow for solvent relaxation, the system was first equilibrated with the protein backbone atoms restrained for 500 ps followed by equilibration without any restraints for 1 ns. A NPT ensemble was used to carry out a production run for 56 ns during which pressure was maintained at 1 Atm using a Nosé-Hoover Langevin piston barostat and temperature was maintained at 300K using a Langevin thermostat. 2 fs was set as the time step. Particle mesh Ewald summation was used to treat long-range electrostatic interactions, while a cutoff distance of 12 Å and switching distance of 10 Å were applied for short-range non-bonded interactions. The SHAKE algorithm was used to contain all hydrogen atom bonds.

5.2.6 Chemical Shift Ensemble Generation

We performed Replica-Averaged Metadynamics (RAM) simulations (Camilloni and Vendruscolo, 2014) of the C_2B-SNARE complex with the TIP4P05 water model using the Amber03W force field (Abascal and Vega, 2005; Best and Mittal, 2010). GROMACS (Pronk et al., 2013) with ALMOST (Fu et al., 2014) and PLUMED2 (Tribello et al., 2014) to run all simulations. Particle mesh Ewald summation was used to treat long-range electrostatic interactions, while a cutoff of 9 Å was used for non-bonded

interactions. The canonical ensemble was used to carry out all simulations. At 1820 nm^3 dodecahedron box of 58,000 water molecules was used to solvate the system. N and HN chemical shifts were back calculated using Camshift (Kohlhoff et al., 2009) and applied over four replicas simulated in parallel at 300 K as averaged restraints (Camilloni et al., 2013), with a 24 kJ/(mol ppm^2) force constant. To increase the agreement with chemical shifts, the force field is thus perturbed as the system evolves resulting from application of the maximum entropy principle (Cavalli et al., 2013; Roux and Weare, 2013).

Bias-exchange metadynamics was used to enhance the sampling over the four replicas (Piana and Laio, 2007) along four different collective variables (CV): 1) the Debye-Huckel energy calculated using only the charged residues between the SNARE complex and C_2B domain (Do et al., 2013); 2) the distance between the SNARE complex and C_2B domain centers of mass; 3) and 4) the difference and sum of dRMSD with respect to the SNARE complex and C_2B domain derived by one PCS data set at a time. The σ values of the four CVs were set to 0.5 kJ/mol, 0.015 nm, 0.005 nm, and 0.005 nm respectively with Gaussian deposition performed at an initial rate of 0.125 kJ/mol/ps. A RAM was used to generate a sampling of conformational space given the complexity of the system and limited backbone chemical shift availability. The system had explored a wide range of conformations after 60 ns of simulation time per replica. For additional PCS analysis, these conformations were classified into 73 low free-energy clusters.

5.2.7 Binding Assays for Synaptotagmin-SNARE complex

1D ^{13}C-edited ^{1}H HSQC spectra of 10 μM uniformly ^{13}C-labeled synaptotagmin-1 C_2AB (residues 140-421) in 25 mM Tris-HCl pH 7.4, 125 mM KSCN, 1 mM $CaCl_2$, 0.5 mM TCEP, 10% D_2O were obtained similarly to as previously described (Arac et al., 2003; Zhou et al., 2013a). Unlabeled SNARE complex was titrated into the sample at the indicated concentrations in the figures up to 20 μM. The strongest methyl resonance (SMR) intensity was measured for each point before subtracting the natural ^{13}C abundance signal from unlabeled SNARE complex that was scaled from the SMR for 20 μM SNARE complex alone.

5.2.8 Assays for Lipid Binding

A mixture of 1-palmitoyl-2-oleoyl-*sn*-glycero-3-phosphocholine (POPC), 1-palmitoyl-2-oleoyl-*sn*-glycero-3-phosphoethanolamine (POPE), 1,2-dioleoyl-*sn*-glycero-3-phosphoethanolamine-N-(5-dimethylamino-1-naphthalenesulfonyl) (Dansyl-DOPE), 1,2-dioleoyl-*sn*-glycero-3-phospho-L-serine (DOPS), cholesterol, L-α-Phosphatidylinositol (PI), and L-α-Phosphatidylinositol 4,5-diphosphate (PIP2) was prepared for liposomes to be used in the binding assays. For Ca^{2+} titrations a stock of 2 mM total lipid was prepared in a mixture of 32% POPC, 23% POPE, 5% Dansyl-DOPE, 25% DOPS, 10% cholesterol and 5% PI. A Photon Technology International spectrophotometer was used to record fluorescence spectra at 25°C by exciting tryptophan fluorescence on Syt1 C_2AB at 280 nm and recording Dansyl-DOPE FRET emission at 528 nm. 0.3 μM Syt1 C_2AB (residues 140-421) and 100 μM lipids were used with the concentrations of Ca^{2+} indicated in the figures for each sample with buffer

composed of 50 mM HEPES-NaOH pH 7.4, 100 mM NaCl, 1 mM $MgCl_2$, 0.5 mM TCEP. The emission intensity of the sample in 2.5 mM EGTA was subtracted from the emission intensity at the given calcium concentration to determine the FRET intensity.

A lipid mixture of 40% POPC, 32% POPE, 12% DOPS, 10% cholesterol, 5% PI, and 1% PIP_2 was used for Ca^{2+}-independent binding experiments. We measured the single methyl resonance (SMR) from 1D ^{13}C-edited ^{1}H NMR spectra of 3 μM Syt1 C_2AB (residues 140-421) with 0 and 1000 μM lipid added in buffer composed of 50 mM HEPES-NaOH pH 7.4, 100 mM NaCl, 1 mM $MgCl_2$, 1 mM EGTA, 0.5 mM TCEP, 10% D_2O.

5.2.9 Synpatotagmin-1 Knockout Rescues

WT and Syt1 KO mice were used to prepare neuronal cultures as described (Maximov et al., 2007). Hippocampi dissected from P0 pups were dissociated with papain digestion then plated on glass coverslips coated with Matrigel. Neurons were cultured with MEM (Gibco) supplemented with B27 (Gibco), transferrin, fetal bovine serum, Ara-C (Sigma), and glucose for 14-16 days *in vitro*. A rat Syt1 cDNA carrying the desired mutation in a lentiviral vector were introduced to cultures for rescue experiments, as previously described (Pang et al., 2010). Human embryonic kidney 293T cells were co-transfected with three packaging plasmids and the lentivral vector to make viruses. The viruses were harvested by collecting the supernatant 48 h after transfection and were used to infect DIV4 neuronal cultures. Physiological or biochemical analyses were performed on cultures at DIV14-16.

5.2.10 Cultured Neuron Electrophysiology Recordings

The electrophysiology was performed similarly as previously described (Bacaj et al., 2013). The whole-cell pipette solution was composed of 10 mM HEPES-CsOH pH 7.4, 135 mM CsCl, 1 mM EGTA, 1 mM Na-GTP, 4 mM Mg-ATP, and 10 mM QX-314, and the bath solution was composed of 10 mM HEPES-NaOH pH 7.4, 140 mM NaCl, 5 mM KCl, 2 mM $MgCl_2$, and 10 mM glucose unless otherwise noted. A Multiclamp 700B amplifier (Molecular Devices) was used to monitor synaptic current and a Model 2100 Isolated Pulse Stimulator (A-M Systems, Inc.) synchronized with the Clampex 9 or 10 data acquisition software (Molecular Devices) used to control extracellular stimuli, while a bipolar electrode triggered evoked synaptic responses. 50 µM AP-5 and 20 µM CNQX in bath solution were used to pharmacologically isolate GABA-R-mediated IPSCs and recorded a holding potential of -70 mV. IPSCs evoke large inward currents because of the high internal CT levels in the intracellular solution. 1 µM tetrodotoxin and the compounds above were used while monitoring mIPSCs. Campfit 9.02 (Molecular Devices) was used to analyze miniature events using a template matching search with a minimal threshold of 5 pA. Inclusion or rejection was visually inspected for each event. For Ca^{2+} titrations, multiple Ca^{2+} concentrations starting at 2 mM were used to measure eIPSCs in each cell, followed by measurement at higher and then lower concentrations. All electrophysiological experiments were performed blind to the genotype/condition of the cultures analyzed.

5.2.11 Immunoprecipitation and Immunoblotting

Cultured Syt1 KO neurons were solubilized for 1 h in the presence of PBS pH 7.4, 1 mM $CaCl_2$, and 0.2% Triton X-100 with protease inhibitors (Roche). The solution was centrifuged at 16,000 g at 4°C for 10 min to clear the lysate. Polyclonal antibodies to syntaxin-1 (438B) or preimmune sera were incubated with the lysate at 4°C over 1 h for immunoprecipitation, followed by 2h incubation with 15 µL of 50% slurry protein-A Sepharose beads (GE Healthcare) at 4°C. After washing four times with 1 mL of extraction buffer, the bound protein was eluted with 2× SDS buffer with 10 mM DTT and boiled at 100°C for 20 min.

SDS-PAGE was used to separate co-precipitated protein which were then detected with monoclonal antibodies for rat synaptobrevin-2 (cl. 69.1, Synaptic Systems) and Syt1 (604.4, Synaptic Systems). Dye-conjugated secondary antibodies were added (IRDye 800CW Donkey anti-Mouse IgG, Li-cor) and membranes were scanned by an Odyssey scanner (Li-cor) using Image Studio software (Li-cor) for quantification.

5.3 Results

5.3.1 A Polybasic Region of the Synaptotagmin-1 C_2B Domain Binds the SNARE Complex

Our efforts to determine structures of Syt1-SNARE complexes are hindered by two major problems. Firstly, NMR analyses at moderate protein concentrations (50-100 µM) suggested the presence of partial aggregation that can lead to multiple non-specific binding sites (Dai et al., 2007), but these concentrations are necessary as binding is weak

without Ca^{2+} present (Zhou et al., 2013a). We made extensive attempts to study Syt1-SNARE complexes in the absence of Ca^{2+} using paramagnetic relaxation effects (PREs), but detected the presence of many sparsely-populated binding modes that impeded our efforts to define the major binding mode (Chapter 4). Secondly, albeit adding Ca^{2+} does increase Syt1-SNARE affinity, the SNARE complex massively precipitates in the presence of a Syt1 construct comprising of two C_2 domains (residues 140-421) with Ca^{2+} even at protein concentrations of 10 μM (Zhou et al., 2013a). We found a longer Syt1 fragment (residues 131-421; referred to as C_2AB) had a lower tendency to aggregate allowing us in part to achieve the results below (Xu et al., 2013). More importantly, while looking for conditions that have minimal aggregation, we also discovered 40-50 μM C_2AB and SNARE complex could be kept in solution with 1 mM Ca^{2+} by including 125 mM thiocyanate (SCN^-), a chaotropic anion that helps to facilitate bona-fide, native protein binding site identification by disrupting non-specific interactions (Richens et al., 2009; Zhang and Cremer, 2006).

With these findings we were able to use TROSY-enhanced ^1H-^{15}N heteronuclear single quantum coherence (HSQC) spectra to analyze the interaction of C_2AB and the SNARE complex and obtain information about the binding site. Chemical shift changes on cross-peaks in the ^1H-^{15}N TROSY-HSQC spectra of ^2H,^{15}N-labeled C_2AB induced by the SNARE complex (Figure 5.1B,C) correspond mostly to the side of the C_2B β-sandwich known as the polybasic region (Figure 5.1A), indicating that the primary binding site for the SNARE complex on C_2AB is the polybasic region. We also observed

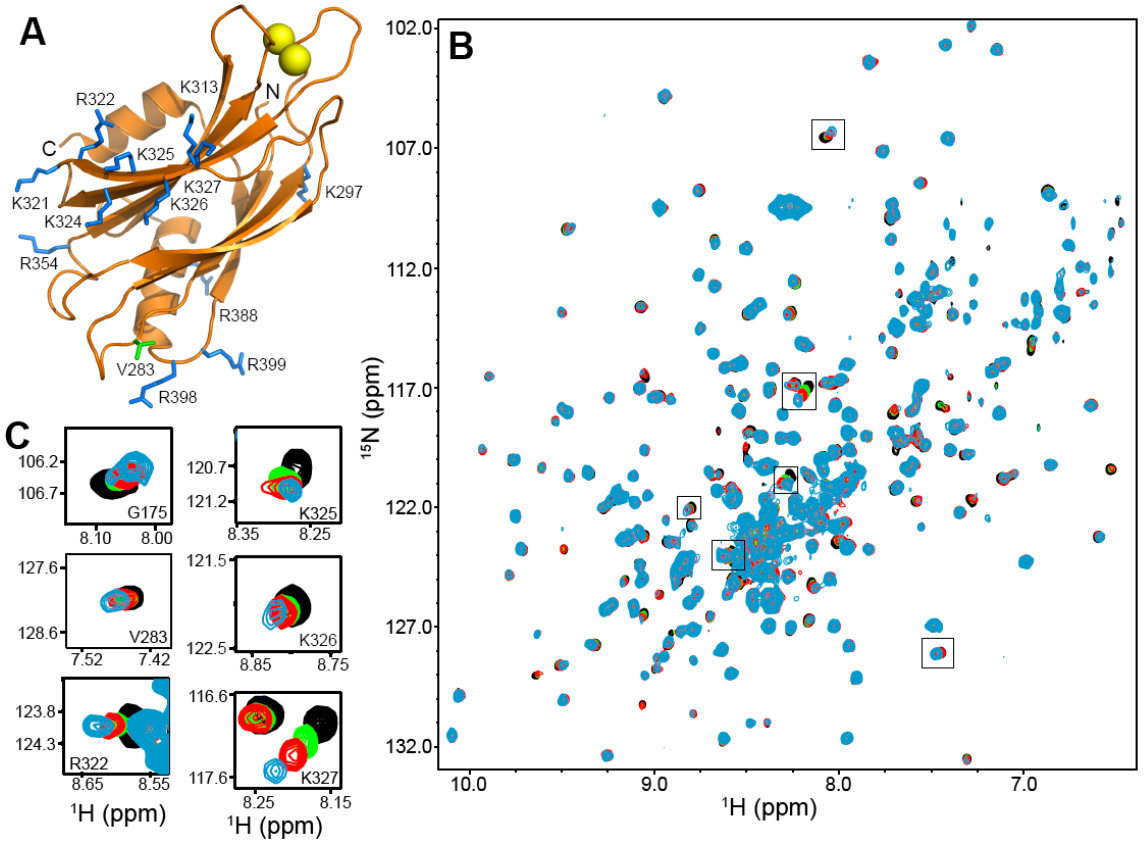

Figure 5.1 The Syt1 C_2B domain polybasic region binds to the SNARE complex. (A) Ribbon diagram of the Syt1 C_2B domain showing the side chains that form the polybasic region, other basic residues that were mutated in this study, and V283, R398 and R399 at the bottom of the domain. Basic residues are colored in blue and V283 in green. Ca^{2+} ions are represented by yellow spheres. N and C represent the N- and C-termini, respectively. (B) ^{1}H-^{15}N TROSY HSQC spectra of ^{2}H,^{15}N-C_2AB (50 µM) in the absence (black contours) and presence of 10, 20 or 40 µM SNARE complex (green, red and blue contours, respectively). (C) Expansions of the regions corresponding to the G175, V283, R322, K325, K326 and K327 cross-peaks in the spectra shown in (B).

chemical shift changes in weaker binding sites that contribute to aggregation of Syt1 (140-421)-SNARE complexes (Zhou et al., 2013a), namely near the R398-R399 region at the bottom of the C_2B domain and on the Ca^{2+}-binding region C_2A domain. Specifically, these changes were seen in the ^{1}H-^{15}N HSQC spectra for cross-peaks from V283 (near R398-R399 on the C_2B domain) and G175 (in a Ca^{2+}-binding loop on the C_2A domain) (Figure 5.1), especially at higher concentrations. These changes suggest that the residues from the region are still able to bind to the SNARE complex, albeit very weakly, possibly due to disruption in interactions due to thiocyanate. The disruptions of these interactions may be the reason for increased solubility of the Syt1-SNARE complex. The amides of the polybasic region exhibited small changes in chemical shifts (Figure 5.1C), likely due to the fact that the binding is mediated by ionic interactions and that the interaction is dynamic. In reverse experiments where $^{2}H,^{15}N$-labeled SNARE complex was added to unlabeled C_2AB, the ^{1}H-^{15}N HSQC spectra had not significant cross-peak changes that could be used to map the binding site on the SNARE complex (Figure 5.2), supporting further that the interaction occurs through ionic contacts and is dynamic.

5.3.2 Pseudocontact Shifts (PCSs) from the SNARE Complex to the Synaptotagmin-1 C_2B Domain

Unlike PREs that can be detected for very sparsely populated states because they depend on only distance from the paramagnetic center to a NMR-active nucleus and are extremely strong at very short distances (Clore and Iwahara, 2009), PCSs depend on both

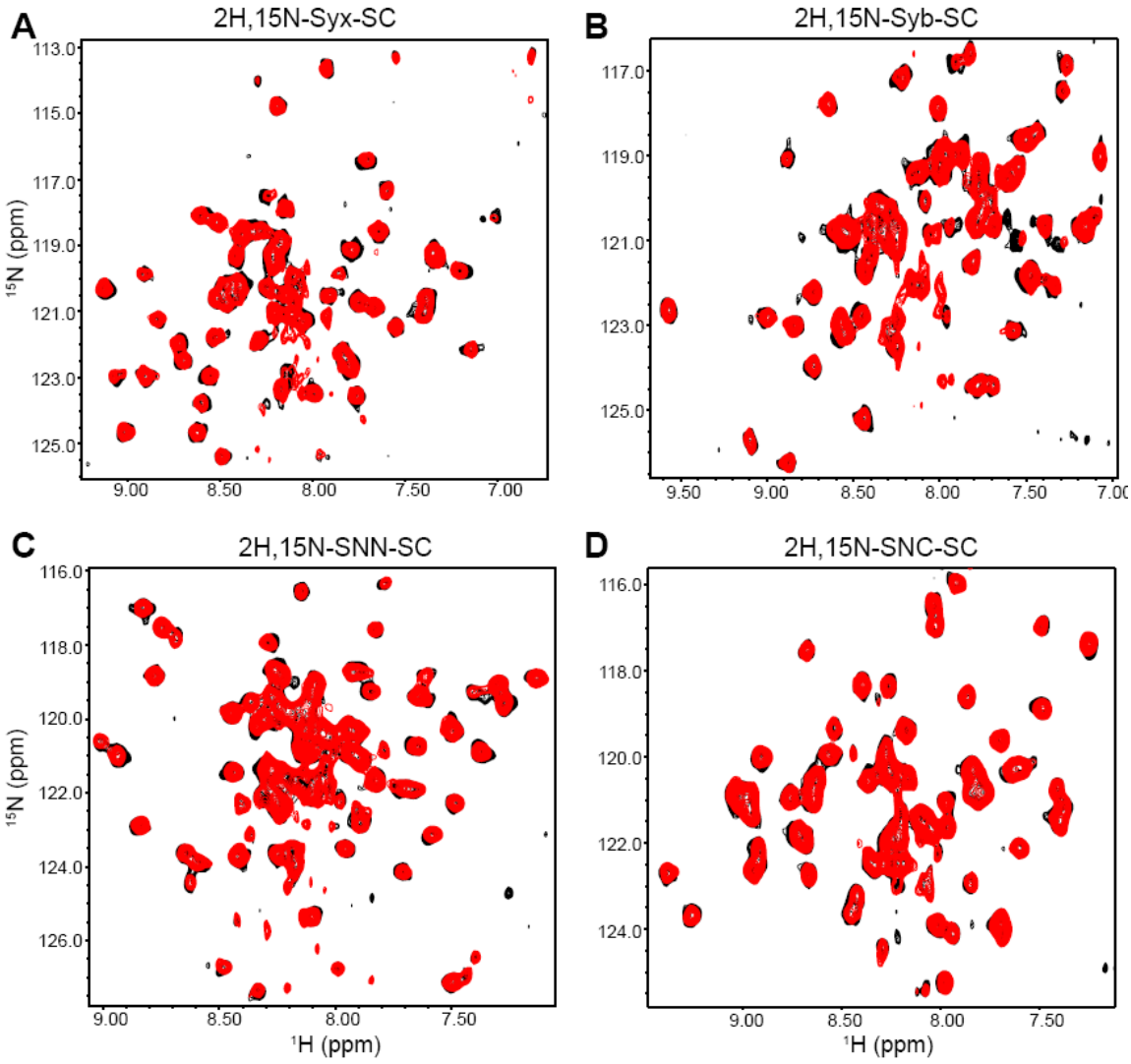

Figure 5.2 Chemical shift perturbations do not reveal the binding site of Syt1 on the SNARE complex. ^{1}H-^{15}N TROSY HSQC spectra of 40 µM SNARE complex samples ^{2}H,^{15}N-labeled at the syntaxin-1 (A), synaptobrevin (B), SNAP-25 N-terminal (SNN) (C), and SNAP-25 C-terminal (SNC) (D) SNARE motifs in the absence (black contours) and presence (red contours) of 20 µM C_2AB. Related to Figure 5.1.

distance and orientation between a lanthanide and a nucleus (Otting, 2010), and therefore PCSs tend to average out to zero over an ensemble of non-specific or sparsely populated states. Due to this feature, PCSs can not only determine structures of stable protein complexes rapidly but also resolve the binding mode preferred within an ensemble of states (Bashir et al., 2011). As we had available the full resonance assignments for the Syt1 C_2A and C_2B domains and the backbone assignments for the SNARE complex (Chen et al., 2005; Chen et al., 2002; Fernandez et al., 2001; Shao et al., 1998), we explored many approaches to attach lanthanides to these proteins to measure PCSs between them and determine a structure of the Syt1-SNARE complex in this manner. We made many attempts over a three year period to incorporate lanthanides into proteins using many lanthanide chelating tags, including dipicolinic acid (Su et al., 2009), EDTA-derived tags (Otting, 2010), and Cys-Ph-TAHA (Peters et al., 2011), but unfortunately these tags led to massive precipitation presumably due to the interaction of the highly acidic SNAREs with lanthanide that escapes from the chelator.

The introduction of 1,4,7,10 tetraazacyclododecane-tetraacetic acid (DOTA)-based lanthanide tags allowed us to overcome this limitation as their very high affinity for lanthanides and extremely slow off rates prevented the protein from interacting directly with free lanthanide. First using Dy^{3+}-DOTA-M8 (Haussinger et al., 2009), we observed double resonances when labeling C_2AB at residue 321 or 396 (by cysteine mutagenesis and modification), which would limit our ability to obtain structural information for the Syt1-SNARE complex. These results showed however that we could add the SNARE complex to C_2AB labeled with Dy^{3+}-DOTA-M8 and have no precipitation, which was an

important step forward. We then tried using a DOTA-amide-based tag known as C2 (no relation to the C_2 domain) that was developed shortly after the DOTA-M8 tag (de la Cruz et al., 2011; Graham et al., 2011) on ten residues of the SNARE complex. We observed strong broadening and only small PCSs, indicating the tag was highly mobile, for the ^{1}H-^{15}N TROSY-HSQC resonances when using four of the residue labeling positions (synaptobrevin residue 72 and 75; SNAP-25 residues 66 and 197). We observed double cross-peaks when attaching the Dy^{3+}-C2 tag to residue 221 of syntaxin-1. When we attached the tag to residue 235 of syntaxin-1, strong PCSs could be obtained, but the PCSs could not be fit to a single tensor. Labeling at the other positions (synaptobrevin residue 55; syntaxin-1 residue 214; SNAP-25 residues 41 and 166) resulted in strong PCSs on the SNARE complex that could be fit to unique anisotropic magnetic susceptibility tensors ($\Delta\chi$ tensors shown for the SNAP-25 residues in Figure 5.3). However, the synaptobrevin residue 55 and syntaxin-1 residue 214 cysteine mutants yielded PCSs on the C_2AB that were too small to be used. When adding 20 μM SNARE complex tagged with Dy^{3+}-C2 at residues 41 and 166 of SNAP-25 (SC41Dy and SC166Dy) to 30 μM C_2AB, the PCSs were small, but could be measured significantly for many cross-peaks of the ^{1}H-^{15}N TROSY-HSQC and ^{1}H-^{13}C HMQC spectra of C_2AB (Figure 5.4A,D). These spectra were obtained with uniformly ^{15}N,^{2}H C_2AB that was also labeled with ^{1}H,^{13}C on methyl groups of Ile, Leu, and Val residues (^{15}N, ^{2}H-ILV-$^{13}CH_3$ C_2AB) as methyl groups have optimal relaxation properties (Ruschak and Kay, 2010).

Adding 30 μM SNARE complex (both for SC41Dy and SC166Dy) to further saturate binding hindered accurate measurements due to increased aggregation that led to

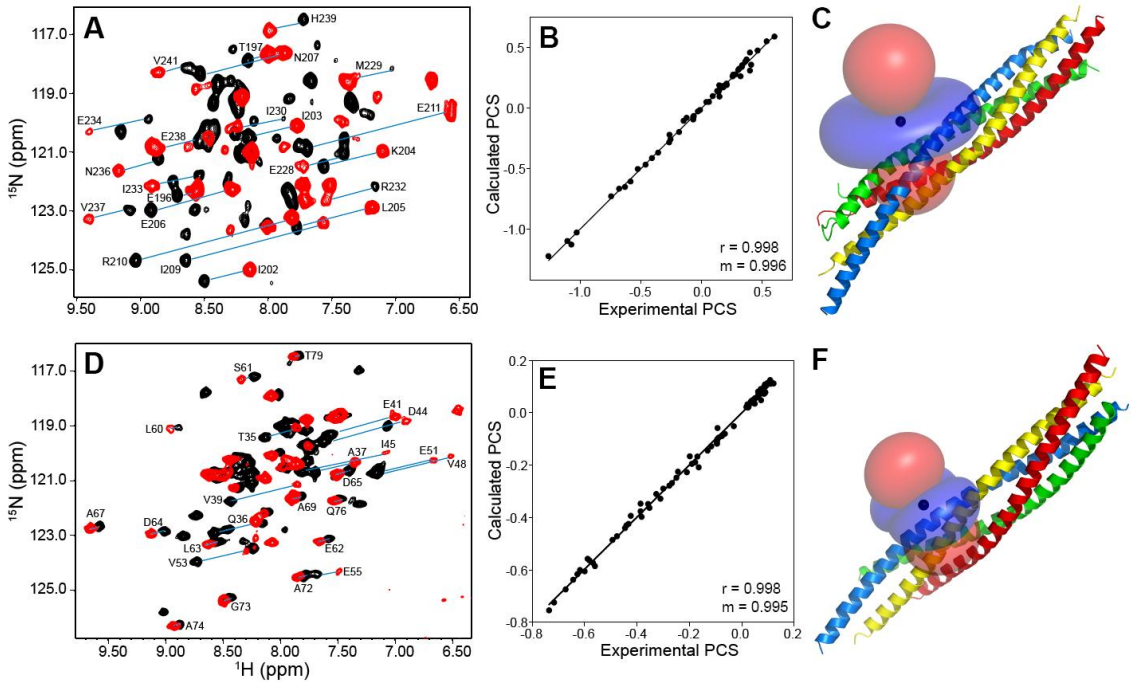

Figure 5.3 PCSs induced in the SNARE complex by Dy^{3+}-C2 labels on residue 166 or 41 of SNAP-25 define Δχ tensors. (A,D) ^{1}H-^{15}N TROSY-HSQC spectra of SNARE complex samples containing ^{2}H,^{15}N-syntaxin-1 (A) or ^{2}H,^{15}N-synaptobrevin (D) and Dy^{3+}-C2 labels on residue 166 (A) or 41 (D) of SNAP-25 before (red contours) or after (black contours) removal of the tag. Blue lines connect selected corresponding red and black cross-peaks, illustrating the observed PCSs. (B,E) Correlation between experimental PCSs measured with Dy^{3+}-C2 labels on residue 166 (B) or 41 (E) of SNAP-25 and PCSs calculated with the Δχ tensors derived from the experimental values. Correlation coefficients (r) and slopes (m) are indicated. The values obtained for $\Delta\chi_{ax}$ and $\Delta\chi_{rh}$ (10^{-32} m^3) are 35.1 and 2.9, respectively, for the SC166 tensor (B), and 15.9 and 6.7, respectively, for the SC41 tensor (E). (C,F) Ribbon diagrams of the SNARE complex (syntaxin, yellow; synaptobrevin, red; SNAP-25 N-terminal and C-terminal

SNARE motifs, blue and green, respectively) with isosurfaces representing regions with positive (blue) and negative (red) PCSs, contoured at ± 0.8 ppm with the SC166 (C) and SC41 (F) tensors. The tensor centers are indicated with black spheres. The same color-coding for the SNAREs is used in all figures.

cross-peak broadening, so we could not obtain larger PCSs. The C_2A domain was previously shown to lead to aggregation (Zhou et al., 2013a) and all the stronger PCSs were observed on the C_2B domain when using the C_2AB construct, so we tried using a Syt1 construct with only the C_2B domain (residues 270-421). We found that adding 30 μM SC41Dy and SC166Dy to 30 μM ^{15}N, ^{2}H-ILV-$^{13}CH_3$ C_2B (Figure 5.4B,E) led to less broadening compared to the C_2AB construct. The PCSs obtained using the either the C_2B or C_2AB construct were parallel and equivalent in relative magnitude (Figure 5.4A,B,D,E), demonstrating that the major binding mode remained the same without the C_2A domain. Since it was observed that Syt1 and CpxI can bind simultaneously to the SNARE complex in solution (Xu et al., 2013), we added Cpx in the experiments with C_2B as a control to examine the PCS data consistency. Only a few cross-peaks changed position slightly for the ^{1}H-^{15}N TROSY-HSQC and ^{1}H-^{13}C HMQC (Figure 5.4C) spectra after adding CpxI, indicating that Syt1 C_2B and CpxI share proximal albeit distinct binding sites on the SNARE complex, with the C_2B domain coming close to van der Waals contact with CpxI.

5.3.3 The Synaptotagmin-1/SNARE Complex is Dynamic in Solution

Aggregation of Syt1 C_2AB and C_2B with the SNARE complex can be largely limited by mutating residues R398 and R399 of C_2B to glutamines (Zhou et al., 2013a). Our NMR data using this C_2B mutant (Figure 5.5A,B) had very similar PCSs to those seen for WT C_2B (Figure 5.4B,E), with a slight improvement in data quality. Residues R398 and R399 do not contribute to the major binding mode and likely mediate

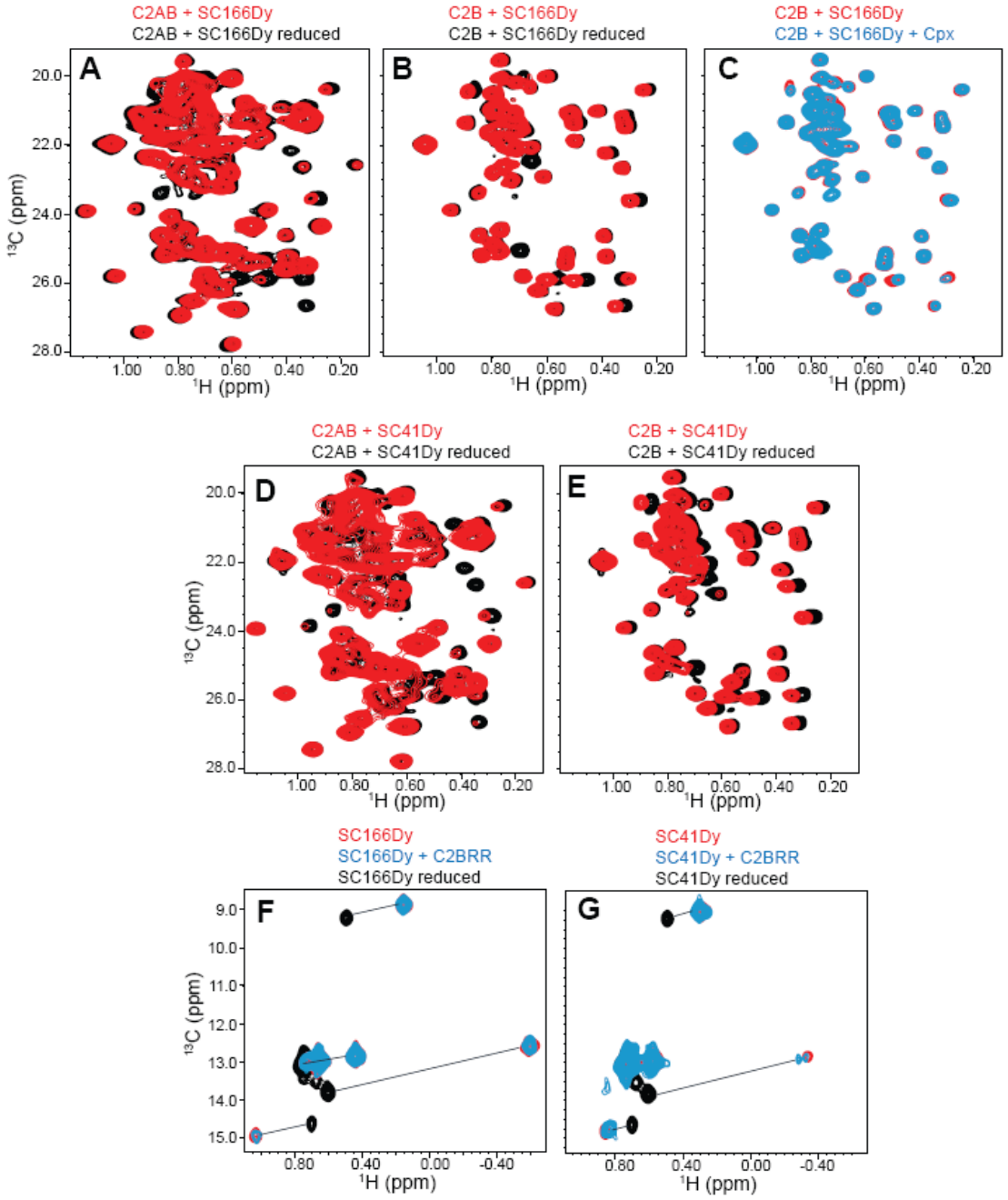

Figure 5.4 SC166Dy and SC41Dy PCS evaluations. (A-E) Leu,Val region of ^{1}H-^{13}C HMQC spectra of 30 μM ^{15}N,^{2}H-ILV-^{13}CH$_3$-labeled C_2AB (A,D) or C_2B (B,C,E) in the presence of SC166Dy (A-C) or SC41Dy (D,E) before (red contours) or after (black

contours) removal of the tag by reduction. The concentration of SC166Dy or SC41Dy was 20 μM in (A,D) and 30 μM in (B,C,E). In (C), blue contours show a spectrum of $^{15}N,^{2}H$-ILV-$^{13}CH_3$-C_2B bound to SC166Dy in the presence of CpxI. Note that in panels (A,C) the contour levels were chosen to allow visualization of some of the PCSs and at the same time the avoid overcrowding observed at lower contour levels. Some of the cross-peaks from the red spectra are not observable at these contour levels due to the broadening caused by the lanthanide tag, but most cross-peaks are observable at lower contour levels and reveal PCSs that are parallel to those observed for C_2B in panels (B,E). (F,G) Ile region of ^{1}H-^{13}C HMQC spectra of 30 μM SC166Dy (F) and SC41Dy (G) containing $^{15}N,^{2}H$-ILV-$^{13}CH_3$-syntaxin-1 acquired after removal of the tag (black contours) or before removal of the tag in the absence (red contours) or presence (blue contours) of 30 μM C_2B domain bearing the R398Q,R399Q mutation (C_2BRR). Related to Figure 5.3.

interactions that are non-native and promote aggregation, which could hinder our structural analyses despite this data being nearly identical to the C_2B data without the mutation, so we used the PCS data from the ^{1}H-^{15}N TROSY-HSQC and ^{1}H-^{13}C HMQC spectra of ^{15}N, ^{2}H-ILV-$^{13}CH_3$ C_2B R398Q,R99Q (referred to below as C_2B for simplicity) for further analysis. We measured 149 and 151 PCSs induced on C_2B by SC41Dy and SC166Dy, respectively. In addition, we obtained ^{1}H-^{13}C HMQC spectra of ^{15}N, ^{2}H-ILV-$^{13}CH_3$ syntaxin-1 for SC41Dy and SC166Dy to see if PCSs induced within the SNARE complex were changed when adding unlabeled C_2B as a control. We observed no changes for SC166Dy (Figure 5.4F), indicating that C_2B does not contract the tag, but we saw changes in the PCSs to a small extent (5-20%) for SC41Dy (Figure 5.4G), indicating that C_2B comes in close proximity or contacts the tag in this position. The tag at SNAP-25 residue 41 may alter the ensemble of SC166Dy data, but we still analyzed the SC41Dy data to determine consistency of the SC166Dy data.

Using the PCSs induced on C_2B, we derived a $\Delta\chi$ tensor on C_2B for SC166Dy (referred to as the C_2B166 tensor; Figure 5.6A) in order to obtain a structure of the C_2B-SNARE complex. This C_2B tensor had good correlations between experimentally measured and back-calculated PCSs (Figure 5.6C), but had a considerably different shape from the tensor derived on the SNARE complex (referred to as the SC166 tensor; compare Figure 5.6A and 5.6B). In addition, when superimposing the two tensors to obtain a model, the SNARE complex does not contact the C_2B domain (Figure 5.6B). In this model, the PCSs back-calculated on the C_2B domain using the SC166 tensor only correlate modestly with the experimentally measured PCSs (Figure 5.6D). The SC166

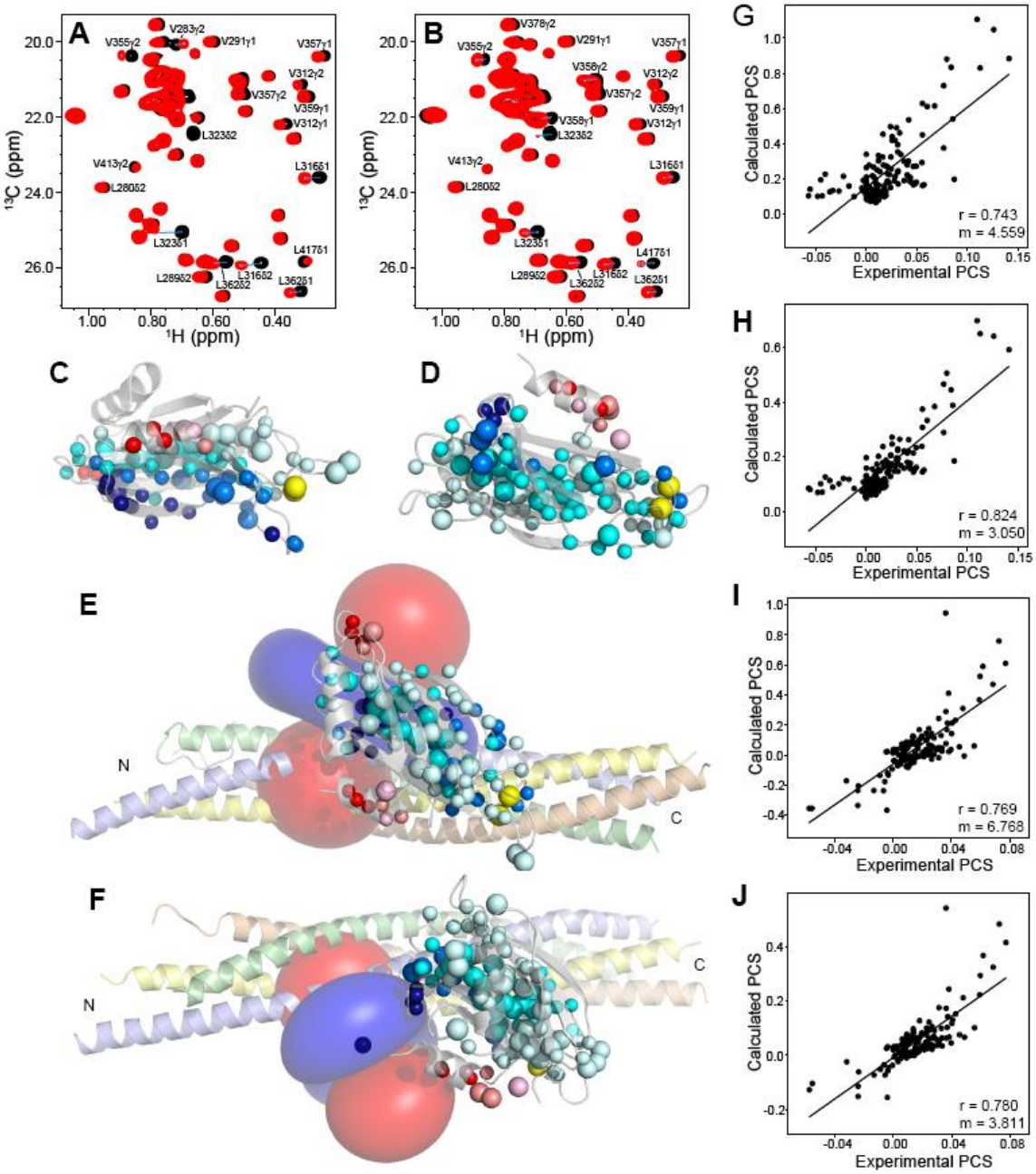

Figure 5.5 PCSs induced on the Syt1 C_2B domain by the SC166Dy and SC41Dy.

(A,B) Leu,Val region of ^{1}H-^{13}C HMQC spectra of 30 μM ^{15}N,^{2}H-ILV-$^{13}CH^{3}$-C_2B

R398Q,R399Q mutant in the presence of 30 μM SC166Dy (A) or SC41Dy (B) before (red contours) or after (black contours) removal of the tag. Assignments of selected methyl cross-peaks are indicated. (C,D) Ribbon diagrams of the Syt1 C_2B domain illustrating the PCSs induced by SC166Dy (C) or SC41Dy (D). Amide hydrogens and methyl carbons are shown as spheres and color-coded according to the measured PCSs (dark blue, > 0.06 ppm; blue, 0.04/0.06 ppm; cyan, 0.02/0.04 ppm; pale cyan, 0.008/0.02 ppm; red, -0.04/-0.06 ppm; salmon, -0.02/-0.04 ppm; light pink, -0.008/-0.02 ppm). Ca^{2+} ions are represented by yellow spheres. (E,F) Models of C_2B bound to the SNARE complex built manually by trying to optimize the match between the positive/negative patterns of C_2B PCSs (shown in panels C,D) and the positive/negative lobes of the SC166 (E) and SC41 (F) tensors represented by isosurfaces as in Figures 5.3C,F. The SNAREs are shown semi-transparent. We refer to these models as the 166 and 41 manual models. Note that when we ascribe a 'good match', some of the nuclei with negative PCSs are not located in the negative lobes of the tensor but are near them such that dynamic motions can readily bring these nuclei into the negative lobes. (G-J) Correlations between experimental PCSs induced on C_2B by SC166Dy (G,H) or SC41Dy (I,J) and PCSs calculated with the 166 and 41 manual models using the optimized SC166 (G) and SC41 (I) tensors (illustrated in Figures 5.3C,F, respectively) or slightly modified tensors (H,J). Correlation coefficients (r) and slopes (m) are indicated. In (H), the SC166 tensor was re-calculated with the SNARE complex PCSs forcing the tensor center to move 4 Å with respect to the optimized center, away from C_2B, yielding r = 0.995 and m = 0.988 for the correlation between measured and calculated SNARE complex PCSs and values of $\Delta\chi_{ax}$

and $\Delta\chi_{rh}$ (10^{-32} m^3) equal to 24.8 and 8.7, respectively. Similarly, in (J), the SC41 tensor center was forced to move 2 Å away from C_2B, yielding r = 0.997 and m = 0.990 for the correlation between measured and calculated SNARE complex PCSs and values of $\Delta\chi_{ax}$ and $\Delta\chi_{rh}$ (10^{-32} m^3) equal to 15.7 and 6.1, respectively.

tensor is axially symmetric, so the C_2B domain can be made to contact the SNARE complex by rotating it around the z-axis (Figure 5.6F). A similar correlation between the calculated and measured C_2B PCSs was obtained (Figure 5.6E), but the C_2B domain bound to the SNARE complex in this model would clash with CpxI (Figure 5.6F). We also attempted to use HADDOCK to obtain structures of the C_2B-SNARE complex that fit the SC166Dy PCS data (Schmitz and Bonvin, 2011), but the structures did not have good correlation between the calculated and measured PCSs. We obtained similar results using the SC41Dy PCS data.

We noticed a well defined pattern of positive and negative PCSs induced by SC166Dy on C_2B (Figure 5.5C), so we manually docked the C_2B domain on the SNARE complex by matching the positive and negative lobes of the SC166 tensor to the positive and negative PCSs on the C_2B domain while keeping contact between the proteins. This model (referred to as the 166 manual model; Figure 5.5E) gave reasonable correlation between the calculated and measured PCSs, although with a large slope (Figure 5.5G). There is a degree of uncertainty in the center coordinates, and since the slope depends strongly on the distance of C_2B from the center of the SC166 tensor, it should be interpreted with caution. We found that changing the tensor center 4 Å in the 166 manual model away from C_2B decreased the slope and improved the correlation of the PCSs on C_2B (Figure 5.5H), while the correlation between calculated and measured PCSs on the SNARE complex remained excellent ($r = 0.995$). Matching the positive and negative lobes of the SC41Dy tensor with the positive and negative PCSs from SC41Dy on C_2B (Figure 5.5D) produced similar results. This model (41 manual model; Figure 5.5F) also

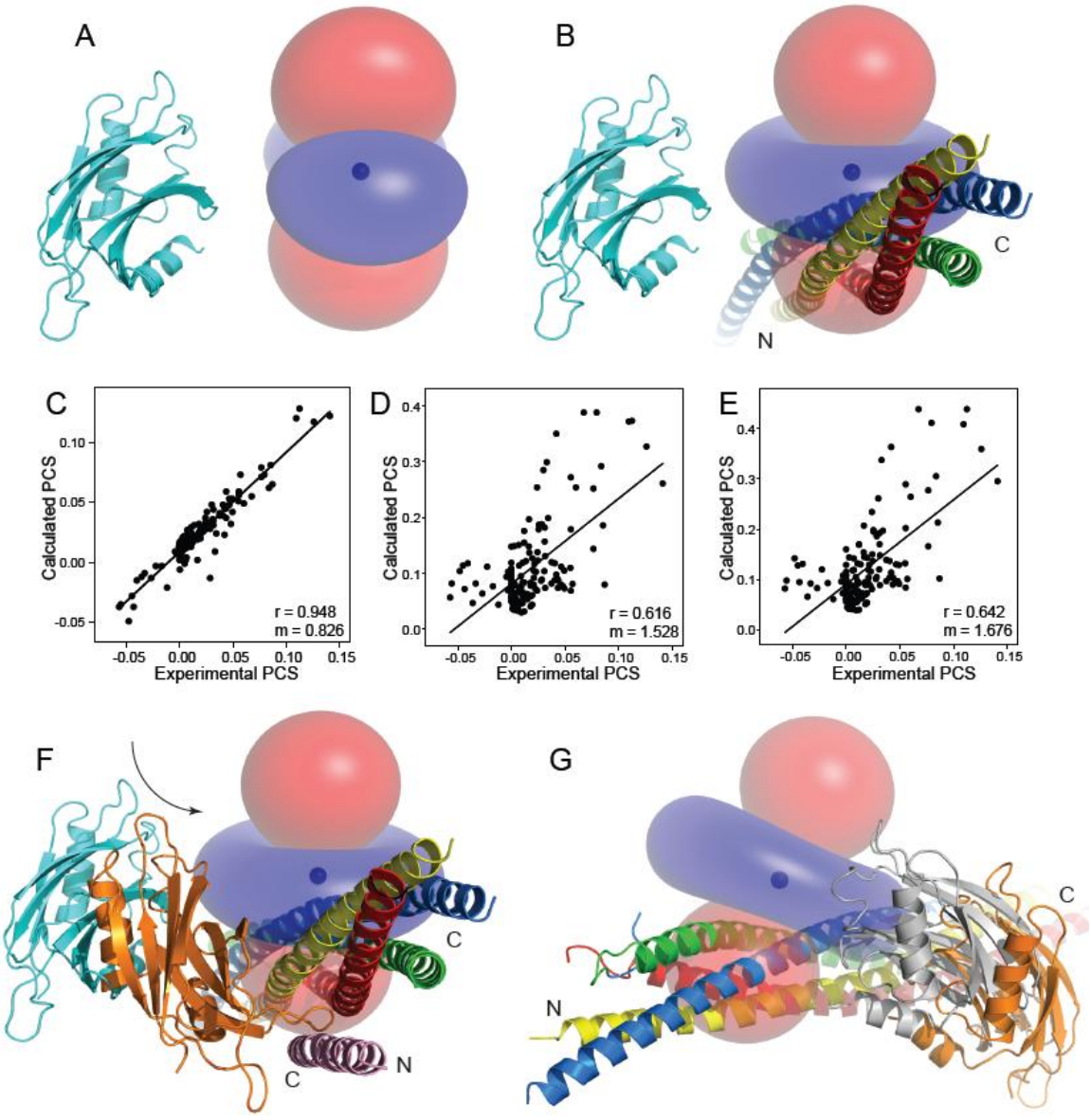

Figure 5.6 SC166 and C_2B166 tensor comparison. (A) Ribbon of the diagram of the C_2B domain and isosurfaces representing regions with positive (blue) and negative (red) PCSs, contoured at ± 0.8 ppm with the C_2B166 tensor. The values for $\Delta\chi_{ax}$ and $\Delta\chi_{rh}$ (10^{-32} m^3) are 32.0 and 18.4, respectively. (B) Ribbon diagram of the C_2B domain and the SNARE complex with isosurfaces representing regions with positive (blue) and negative

(red) PCSs, contoured at ± 0.8 ppm with the SC166 tensor. This is the same tensor illustrated in Figure 5.3C but rotated to allow comparison with the C_2B166 tensor shown in panel A. The position of C_2B was derived by superimposing the centers of the SC166 and C_2B166 tensors. (C) Correlation between experimental C_2B PCSs caused by SC166Dy and PCSs calculated with the C_2B166 tensor illustrated in panel (A). (D) Correlation between experimental C_2B PCSs caused by SC166Dy and PCSs calculated with the SC166 tensor in the model resulting after superimposing the C_2B166 and SC166 tensors (illustrated in panel B). (E) Correlation between experimental C_2B PCSs caused by SC166Dy and PCSs calculated with the SC166 tensor in the model with C_2B rotated, illustrated with C_2B in orange in panel (F). (F) Ribbon diagram of the SNARE complex with isosurfaces representing regions with positive (blue) and negative (red) PCSs, contoured at ± 0.8 ppm with the SC166 tensor, showing the positions of C_2B after superimposing the centers of the SC166 and C_2B166 tensors (cyan ribbon) and after rotating C_2B around the vertical axis (defined here by the negative lobes of the SC166 tensor) to make contact with the SNARE complex (orange ribbon). CpxI(26-83) is also shown (in pink) based on superimposing the models with the crystal structure of the CpxI(26-83)-SNARE complex (PDB code 1KIL) to illustrate that C_2B would have steric clashes with CpxI(26-83) in the position of the orange ribbon. (G) Ribbon diagram of the SNARE complex with isosurfaces representing regions with positive (blue) and negative (red) PCSs, contoured at ± 0.8 ppm with the SC166 tensor, showing in orange the rotated position of C_2B from panel (F) and in gray the position of C_2B from the 166 manual model of Figure 5.5E. In (A,B,F,G), the tensor center is indicated with a black sphere.

Note that in (F) the rotated C_2B (orange) is at the same distance from the tensor center as in the original model obtained by superimposing the centers of the C_2B166 and SC166 tensors (cyan C_2B), and that in (G) C_2B from the 166 manual model (gray) is considerably closer to the tensor center than the rotated C_2B (orange). Related to Figure 5.5.

gave a reasonable correlation between calculated and measured PCSs for the C_2B PCSs, again with a large slope (Figure 5.5I). Changing the tensor center 2 Å in the 41 manual model away from C_2B decreased the slope and improved the correlation of the PCSs on C_2B slightly (Figure 5.5J), while the correlation between calculated and measured PCSs on the SNARE complex also remained excellent ($r = 0.997$), demonstrating again the tensor center and slope of the correlations of the C_2B PCSs are uncertain.

The highly dynamic nature of the interaction between C_2B and the SNARE complex is most likely the reason for the large slopes in Figure 5.5G-J. The dynamic nature is also seen through the different shapes of tensors that result from PCSs on the SNARE complex and C_2B domain (Figure 5.6A,B). A distorted tensor has similarly been observed to be created by the fast motions of a lanthanide relative to a molecule, attenuating the recorded PCSs and creating a tensor center further away from the molecule than the genuine lanthanide position (Shishmarev and Otting, 2013). The distance of the C_2B to SC166 tensor center in the 166 manual model (Figure 5.6G) and the distance of C_2B to the C_2B166 tensor center (Figure 5.6A) likewise show that C_2B166 tensor center is further away.

The large slopes in Figure 5.5G-J may also be explained by the preferred binding site being only modestly populated. We tested this possibility by using HADDOCK to find structures to fit the measured PCSs on C_2B scaled by factors from two to seven. Structures were not obtained with a good fit using the SC41Dy data, but we did obtain structures using the SC166Dy data with consistent orientations of the C_2B relative to the

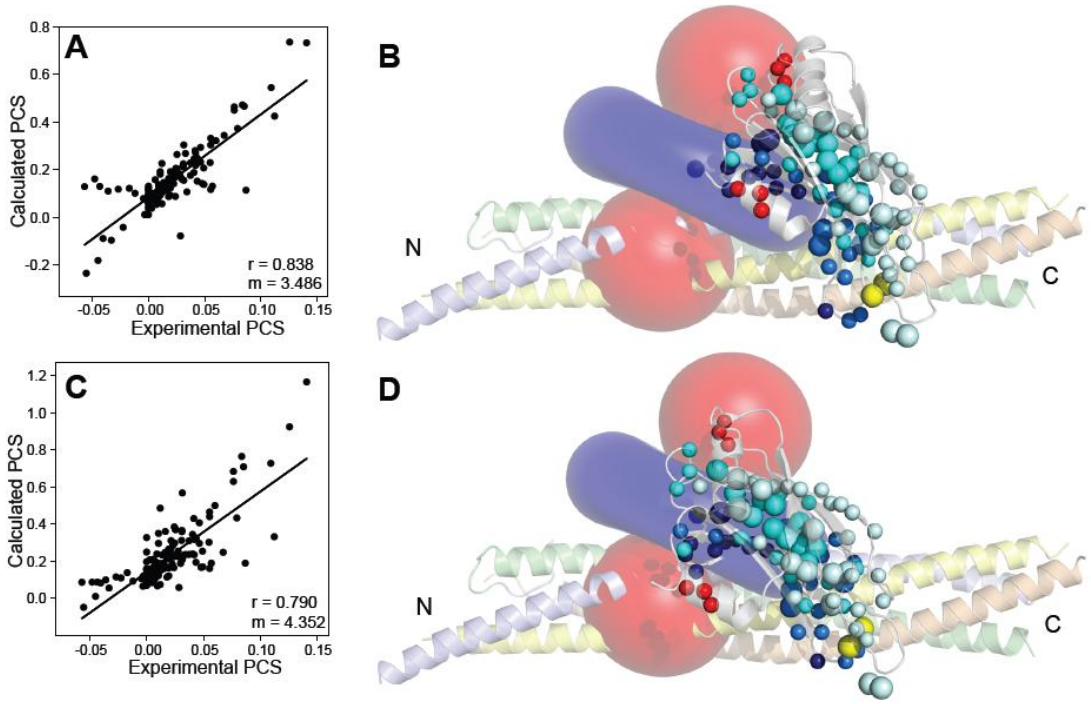

Figure 5.7 Analysis of 166 HADDOCK and MD C_2B-SNARE complex models. (A,C) Correlations between experimental C_2B PCSs induced by SC166Dy and PCSs calculated with the SC166 tensor and the 166 HADDOCK model (A) or the 166 MD model (C). Correlation coefficients (r) and slopes (m) are indicated. (B,D) Representations of the 166 HADDOCK model (B) and 166 MD model (D) with the SNAREs and C_2B shown as semi-transparent ribbons and the positive/negative lobes of the SC166 tensor represented by isosurfaces as in Figure 5.3C. The C_2B PCSs induced by SC166Dy are illustrated to visualize how well the positive/negative patterns match with the positive/negative lobes of the SC166 tensor. Amide hydrogens and methyl carbons are shown as spheres and color-coded according to the measured PCSs (dark blue, > 0.06 ppm; blue, 0.04/0.06 ppm; cyan, 0.02/0.04 ppm; pale cyan, 0.008/0.02 ppm; red, -0.04/-

0.06 ppm; salmon, -0.02/-0.04 ppm; light pink, -0.008/-0.02 ppm). Ca^{2+} ions are represented by yellow spheres. Related to Figure 5.8.

SNARE complex and good correlations between the measured and calculated PCSs, illustrated by a representative structure obtained by scaling the PCSs on C_2B by a factor of five (referred to as the 166 HADDOCK model; Figure 5.7A). Despite these results, the number of salt bridges between the SNAREs and C_2B were limited, and the positive and negative lobes of the SC166 tensor did not match well the positive and negative PCS pattern on C_2B (Figure 5.7B). Also, in unrestrained molecular dynamics (MD) simulations starting with the 166 HADDOCK model, C_2B moved toward the position of the 166 manual model after visiting a wide range of orientations (Figure 5.8A,B), demonstrated by a representative structure near the end of the simulation (orange in Figure 5.8A,B). This structure (referred to as the 166 MD model) has a good correlation between the calculated and measured PCSs (Figure 5.7C), multiple salt bridge between the SNAREs and C_2B (see below), and a good match of positive and negative patterns between the SC166 tensor lobes and C_2B PCS pattern (Figure 5.7D). The 166 HADDOCK model (purple, Figure 5.8A) has the C_2B oriented similarly as in the manual model (gray, Figure 5.8A), but the HADDOCK model "pushes away" the C_2B domain from the tensor center. This "pushing away" appears to result naturally from attempting to fit a single structure to all the PCS data and is unavoidable since PCSs for many residues that are more highly dynamic relative to the tensor center quickly approach zero.

This overall analysis demonstrates that fitting PCS data averaged due to dynamics cannot necessarily be reliably fit to single structures, and that the motions of C_2B relative to the SNARE complex can cause large slopes as seen in Figure 5.5G,H and 5.7C when doing so. Therefore, the 166 manual and MD models can be considered to be located

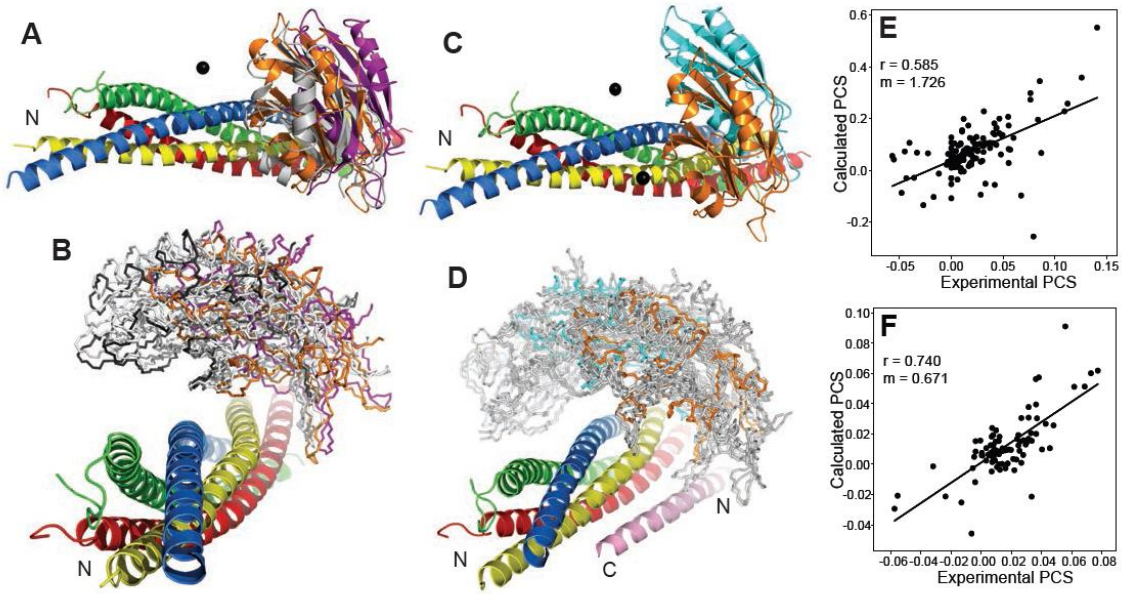

Figure 5.8 Analysis by MD simulations of the C_2B-SNARE complex. (A) Ribbon diagrams of the SNARE complex and C_2B in the positions corresponding to the 166 manual model (gray), the 166 HADDOCK model (purple), and the 166 MD model (orange). (B) Ribbon diagram of the SNARE complex and stick models showing Cα traces of C_2B in a range of orientations visited during the MD simulation started from the 166 HADDOCK model (purple). One of the structures from the end of the simulation (in orange) is represented in panel (A) and is referred to as 166 MD model. (C) Ribbon diagrams of the SNARE complex and C_2B in the positions corresponding to the 166 MD model (orange) and the 41 manual model (cyan). (D) Ribbon diagram of the SNARE complex and stick models showing the Cα traces of C_2B in a range of representative orientations visited during MD simulations incorporating chemical shift restraints. The structure of the CpxI(26-83)-SNARE complex (PDB code 1KIL) has been superimposed to show that CpxI would bump with C_2B in some of the positions in the MD simulations.

N represents the N-terminus of the SNARE complex in (A-D). N and C represent the N- and C-termini of CpxI(26-83) in (D). (E,F) Correlations between experimental C_2B PCSs induced by SC166Dy (E) or SC41Dy (F) and PCSs calculated as ensemble averages using different populations of structures from the 73 clusters visited during the chemical-shift restrained MD simulations. Correlation coefficients (r) and slopes (m) are indicated.

approximately at the center of ensemble states of the C_2B-SNARE complex as representative structures derived from 166 PCS data, but the ensemble clearly encompasses multiple binding modes involving interactions with nearby sites and/or different orientations of C_2B. The 41 manual model similarly is located at approximately center of ensemble states represented in the 41 PCS data. The positions of the 41 manual model and 166 MD model are quite close for the C_2B domain (Figure 5.8C), and the uncertainty in the analysis and/or binding mode perturbation caused by tag for the SC41Dy data (see above) could give rise to the differences between these models. The ensembles probed by the 166 and 41 PCSs likely overlap extensively considering the highly dynamic nature of the C_2B-SNARE complex, and the preferred binding modes exhibited in both data sets are closely related (see below).

We performed extensive MD simulations restrained by chemical shifts (Camilloni et al., 2012) to obtain a wider range of structures that are potentially in these ensembles. The 166 MD model and 41 manual model were located at the center of the structures visited during the simulations for this ensemble (Figure 5.8D), demonstrating the consistency of the results above with these simulations.

These structures were classified into 73 clusters and one member from each cluster was used to calculate the PCSs on C_2B. We then found the population weights to obtain optimal correlations between the experimentally measured and the population-averaged PCSs. A reasonable degree of correlation between the measured and population-averaged PCSs was found for both the SC166Dy and SC41Dy PCS data, with slopes much closer to one than those obtained with the individual representatives of the

ensemble (Figure 5.8E,F). However, the correlation coefficients are poorer with this treatment, and the structures that dominate the fits are far from the center of the tensors. In addition, structures for the SC166Dy data included structures with strong steric overlap between C_2B and CpxI. Therefore, from the chemical shift-restrained MD simulations, many structures are likely to form part of the ensemble of C_2B-SNARE complex binding modes, but additional structures are necessary to account for the observed PCSs fully. Altogether, these results demonstrate that the calculated PCSs are decreased by averaging PCSs over an ensemble of structures, mirroring what we see in our experimental results, but only modest correlations between calculated and experimental PCSs could be achieved using the current methods.

5.3.4 Binding Mode of the Synaptotagmin-1/SNARE Complex in Solution

To fit the PCS data better, a more extensive exploration of C_2B-SNARE complex orientations is necessary. Development of molecular dynamics simulations with replica-averaged PCS restraints will likely help this analysis, as described for residual dipolar couplings that were similarly dynamically averaged (De Simone et al., 2011), but finding conformational ensembles that fit the experimental data and are faithful representations of the true ensembles remains a major challenge (Varadi et al., 2014), especially since the experimental data can never be used to fully verify the reality of these ensembles. Importantly, although the complete ensemble of the Syt1-SNARE complex is relatively uncertainty, we are able to have a clear view of how the Syt1 and the SNARE complex predominantly interact in solution from our structural models. These models can be

probed to test the relevance of Syt1-SNARE complex interactions functionally and determine how these proteins cooperate in triggering neurotransmitter release.

First, the PCSs observed clearly define that the C_2B polybasic region binds to a SNARE complex polyacidic region formed by the syntaxin-1 SNARE motif and the SNAP-25 N-terminal SNARE motif, with these regions comprising the interaction interface for all models (Figure 5.9A-D). Second, the large number of C_2B basic residues and SNARE complex acidic residues give a clear rationale behind the dynamic interaction of the Syt1-SNARE complex, as a static structure would only represent one of the many binding modes possible in solution. Third, even with limitations of no single structure faithfully representing the many binding modes, the 166 MD model (or 166 manual model) and 41 manual model share common features from which emerge predictions about the most important residues for binding. Noteworthy is that in both models, the C_2B concave surface of the β-sandwich is proximal to the surface of the SNARE complex (Figure 5.9A,B). Therefore, although the C_2B polybasic strand (residues 321-327) was seen as a functional unit, key distinctions between the functional importance of certain residues in this region arise from both models. R322, K325, and K327 from the polybasic strand and K313 from the neighboring β-strand face and contact the SNARE complex directly highlighting that they are highly probable to be critical for binding. On the other hand, K324 and K326 are close to the SNARE complex, but not oriented directly towards it, so these residues would be predicted to have less prominent roles even if they still do assist binding. The difference in these groups of residues arises from the PCS data which defines the preferred orientation and is further supported by

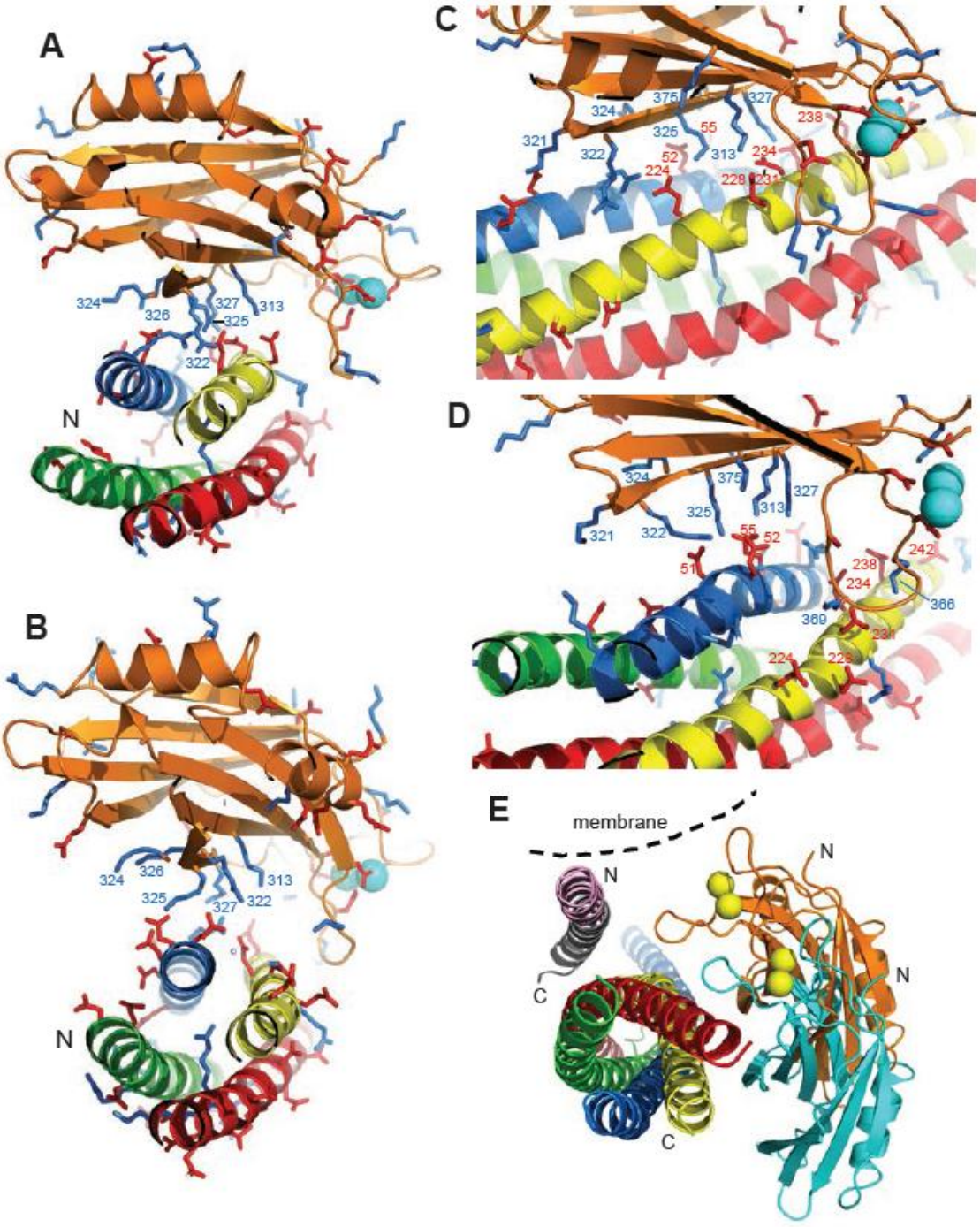

Figure 5.9 The binding mode Syt1 C_2B-SNARE complex. (A,B) Ribbon diagrams of the 166 MD model (A) and the 41 manual model (B) with C_2B shown in orange and Ca^{2+} ions represented by cyan spheres. Stick models show the side chains of basic (blue) and

acidic (red) residues. Basic side chains from the polybasic strand and the concave side of C_2B are labeled. (C,D) Close-ups of the binding modes observed in the 166 MD model (C) and 41 MD model (D). Representation and color-coding are as in (A,B). Selected basic and acidic side chains in the interfaces are labeled. (E) Ribbon diagrams showing the positions of C_2B in the 166 MD model (orange) and the 41 manual model (cyan) after superposition with the structure of the CpxI(26-83)-SNARE complex (PDB code 1KIL). CpxI(26-83) is shown in pink (accessory helix) and gray (central helix). The dashed line represents a membrane surface and illustrates that binding of C_2B to a membrane would lead to steric and electrostatic repulsion of the CpxI accessory helix with the membrane. N represents the N-terminus of the SNARE complex in (A,B) and the N-terminus of CpxI(26-83) and C_2B in (E). C represents the C-termini of CpxI(26-83) and the SNARE complex in (E).

MD simulations where the concave face of C_2B facing the SNARE complex has higher probability than K324 and K326 facing the SNAREs.

The SNARE complex residues that participate in interaction with C_2B in different models are more varied, arising from the presence of more acidic residues and a larger acidic surface in the proximal region. For the 166 MD model, the groove formed by the syntaxin-1 SNARE motif and SNAP-25 N-terminal SNARE motif (referred to as SNN) is oriented toward the concave face of C_2B, with several ionic interactions on syntaxin-1 (E224,E228, D231, and E234) and several residues of SNN (D51, E52, and E55) nearby (Figure 5.9C). On the other hand, the 41 manual model primarily involves the SNN residues to mediate this interaction (Figure 5.9B). The 41 model was built manually, so a detailed analysis of it is not suitable, but the chemical shift-restrained MD simulations similarly placed the C_2B domain close to the locations seen in the 41 manual model, giving some insight into the possible interactions in this area. A representative from these structures (referred to as the 41 MD model; Figure 5.10) reveals that the SNN acidic residues can establish multiple salt bridge with residues K313, R322, K325, and K327 of C_2B (Figure 5.9D). The syntaxin-1 acidic region was also observed to interact with residues K366 and K369 of C_2B at the Ca^{2+} binding loops.

In summary, the representative structures we obtained led to a model in which the predominant interactions of the Syt1-SNARE complex are mediated by the polybasic residues on the concave surface of the C_2B domain and the acidic region of syntaxin-1 and SNN, surfaces present in all the structures visited in the MD simulations. This model explains the basis for the dynamic nature of the Syt1-SNARE complex, as the large

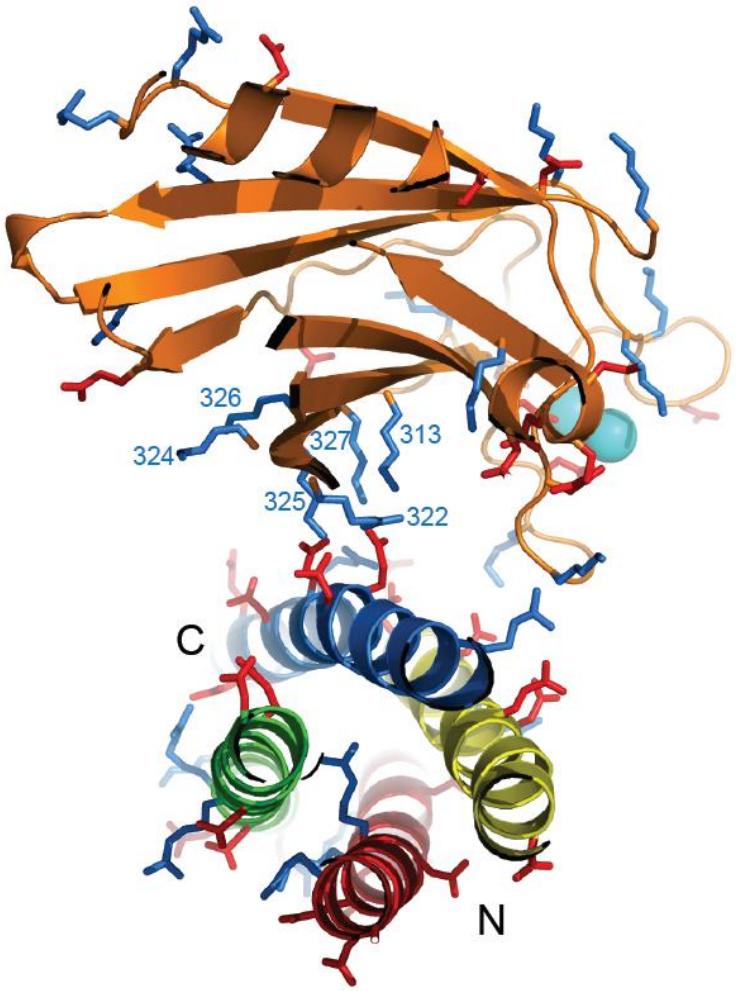

Figure 5.10 The binding mode Syt1 C_2B-SNARE complex 41 MD model. Ribbon diagram of the 41 MD model with C_2B shown in orange and Ca^{2+} ions represented by cyan spheres. Stick models show the side chains of basic (blue) and acidic (red) residues. Basic side chains from the polybasic strand and the concave side of C_2B are labeled. N and C represent the N- and C-termini of the SNARE complex, respectively. Related to Figure 5.9.

number of charges on both surfaces allows multiple salt bridges to occur in many different orientations with similar thermodynamic equivalence. The finding that CpxI (residues 26-83) and Syt1 C_2AB bind simultaneously to the soluble SNARE complex while being in competition for SNARE complexes anchored to a membrane (Xu et al., 2013) is also explained by this model. The simultaneous binding of CpxI(26-83) and C_2B is allowed by distinct binding sites on the SNARE complex, but C_2B binding to a membrane when induced by Ca^{2+} results in strong steric and electrostatic repulsion between the CpxI accessory helix and the membrane (Figure 5.9E), both being negatively charged. In addition, even the simultaneous binding in solution places CpxI(26-83) and C_2B in close proximity on the SNARE complex (Figure 5.9E), explaining why CpxI induced slight perturbations in the PCSs induced by SC166Dy on C_2B (Figure 5.4C).

5.3.5 Confirmation of the Synaptotagmin-1/SNARE Complex Binding Mode via Mutagenesis

To test our model of the Syt1-SNARE complex and look at the specific side chains contributing to binding, we used an assay in which the strongest methyl resonance (SMR) intensity in 1D ^{13}C-edited ^{1}H-NMR spectra of uniformly labeled ^{13}C-labeled C_2AB decreases upon unlabeled SNARE complex binding (Figure 5.11A) (Arac et al., 2003). The native R398-R399 at the bottom of C_2B was included for all C_2AB used in these assays. We performed initial experiments to follow a recent study of interactions in the Syt1-SNARE complex (Zhou et al., 2013a) under the same conditions (with 125 mM NaCl, not KSCN), titrating SNARE complex into 3 μM ^{13}C-labeled C_2AB with a single

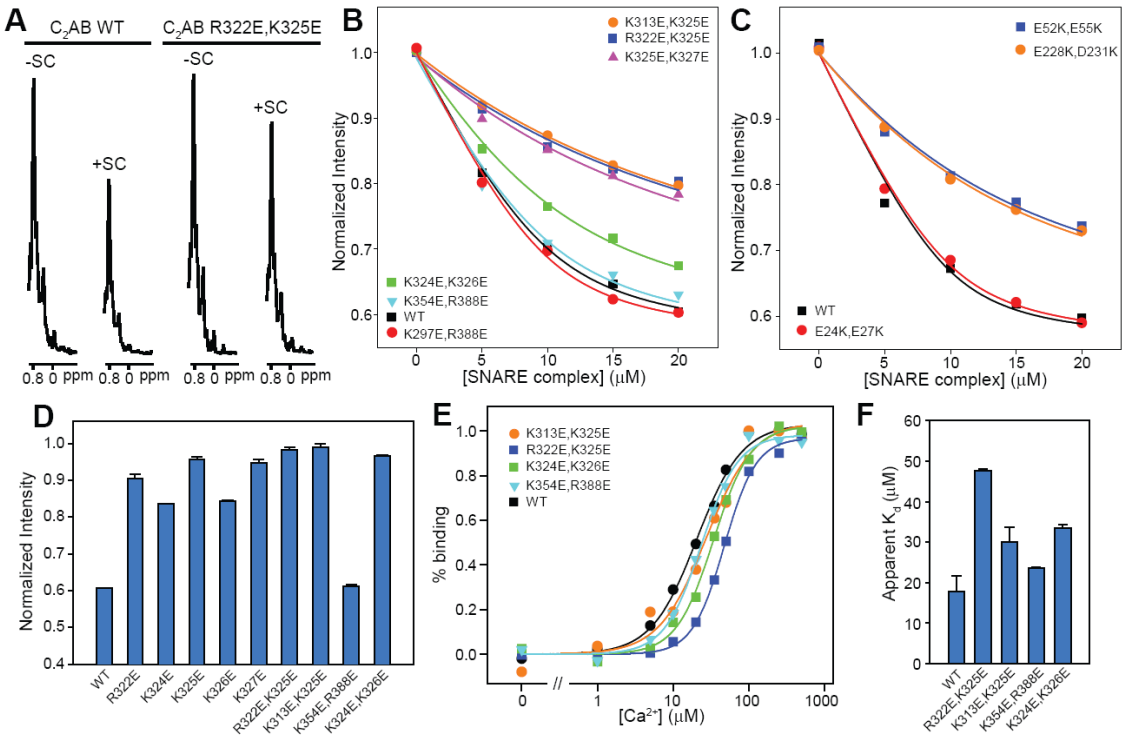

Figure 5.11 Verification of the binding mode for the C_2B-SNARE complex by mutagenesis. (A) 1D ^{13}C-edited ^{1}H-NMR spectra of 10 μM ^{13}C-labeled WT or R322E,K325E mutant C_2AB in the absence or presence of 15 μM unlabeled SNARE complex (SC). (B) Plots of normalized intensities of the SMRs in 1D ^{13}C-edited ^{1}H-NMR spectra of 10 μM WT or mutant ^{13}C- C_2AB as a function of SNARE complex concentration. The mutations in C_2AB are indicated and color-coded. (C) Plots of normalized intensities of the SMRs in 1D ^{13}C-edited ^{1}H-NMR spectra of 10 μM WT ^{13}C-C_2AB as a function of WT or mutant SNARE complex concentration. The mutations in SNARE complex are indicated and color-coded (E24K,E27K and E52K,E55K are in SNAP-25; E228K,D132K is in syntaxin-1). The data in (B,C) were obtained in 25 mM Tris (pH 7.4), 125 mM KSCN and 1 mM $CaCl_2$, and were fitted to a single-site binding

model (Zhou et al., 2013) yielding the K_ds summarized in Figure 5.12C,D, respectively. The intensities at 0 μM SNARE complex concentration calculated from the fitting of each data set were used to normalize all the data. (D) Bar diagrams showing the intensities of the SMRs in 1D ^{13}C-edited ^{1}H-NMR spectra of 3 μM WT or mutant ^{13}C-C_2AB upon addition of liposomes containing 1% PIP_2 (1 mM total lipid), normalized by the intensities observed in the absence of liposomes. (E) Binding of WT and mutant C_2AB to dansyl-labeled liposomes as a function of Ca^{2+} concentration measured from Trp-dansyl FRET. The data were fit with Hill equations. (F) Bar diagram illustrating the apparent Ca^{2+} K_ds obtained for WT and mutant C_2AB in Ca^{2+}-dependent phospholipid binding experiments such as those shown in (E). Bars show average K_ds calculated from two independent experiments, and error bars show standard deviations.

point charge reversal mutation, but found that these mutants did not have any strong effects on binding (Figure 5.12A,B). This result likely is due to the large number of charges on the C_2B binding surface that can rearrange to form thermodynamically equivalent complexes, so we prepared ^{13}C-labeled C_2AB with two residue charge reversal mutants by replacing two basic residues with glutamates. We also increased the concentration for the C_2AB mutants to 10 μM to improve the signal to noise and used 125 mM KSCN to minimize contributions in the assay from interactions that lead to aggregation, as used in PCS measurements.

Notably, as predicted from our representative structural models, the three double mutants replacing residues on the concave face of C_2B (K313E,K325E; R322E,K325E; K325E,K327E) strongly impaired binding when titrating unlabeled SNARE complex into ^{13}C-C_2AB (Figure 5.11B), while control double mutants not part of the polybasic region at different distances from the region (K297E,R388E and K354E,R388E; see Figure 5.1A) have no affect on binding. Importantly, a double mutant in the polybasic region on the side but not on the concave face of C_2B (K324E,K326E) impaired binding to a much lesser extent than the mutations of the polybasic directly on the concave face (Figure 5.11B). To give a semiquantitative picture of the mutations, the apparent K_ds were derived from these data (Figure 5.12C), but these experiments did not use SNARE complex concentrations more than 20 μM to avoid contributions of weaker binding sites, so the mutants with stronger binding impairments in the titrations were far from saturation and the apparent K_ds should be interpreted with caution. Nevertheless, these

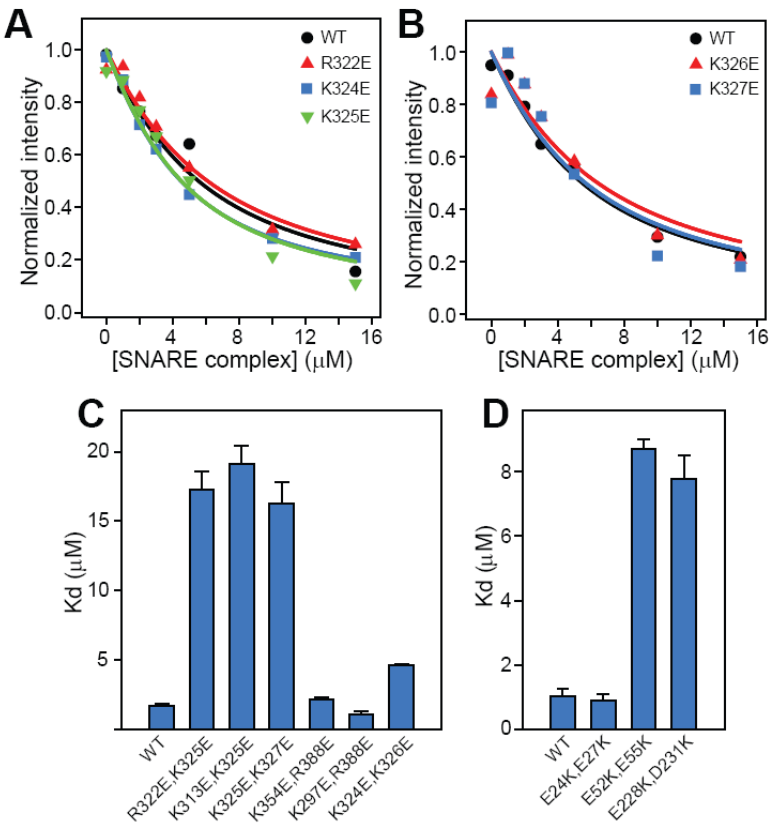

Figure 5.12 Further verification of the binding mode for the C_2B-SNARE complex by mutagenesis. (A,B) Plots of normalized intensities of the SMRs in 1D ^{13}C-edited ^{1}H-NMR spectra of 3 μM WT or mutant ^{13}C-C_2AB as a function of SNARE complex concentration. C_2AB mutants contained single substitutions in basic residues as indicated and color-coded. The data were acquired in 25 mM Tris (pH 7.4), 125 mM NaCl and 1 mM $CaCl_2$, and were fitted to a single-site binding model (Zhou et al., 2013). (C,D) Bar diagrams illustrating the K_ds derived from fitting the data of Figures 5.9B,C to single-site binding models. Because of the uncertainty in the limiting intensities at infinite SNARE complex concentrations for the mutants that bind to the SNARE complex more weakly,

this limiting value was forced to be 0.555 times the intensity at 0 SNARE complex concentration. The 0.555 factor was derived from averaging the ratios between intensities at 0 and infinite SNARE complex concentration in the fits obtained for WT C_2AB. Bars show average K_ds calculated from two independent experiments, and error bars show standard deviations. Related to Figure 5.11.

data clearly demonstrate the C_2B concave face is the primary interaction surface for the SNARE complex in these assays, further confirming our representative structural models that also fall into this orientation. In addition, titrating charge reversal double mutants on syntaxin-1 and SNN (syntaxin-1 E228K, D231K and SNN E52K,E55K) in the SNARE complex, based on these representative models from our PCS data, into WT ^{13}C-C_2AB impaired biding markedly, while a mutation in another acidic patch (SNN E24K,E27K) used as a control had no effect (Figures 5.11C,5.12D). Interestingly, although the syntaxin-1 E228K, D231K and SNN E52K,E55K mutations produce considerable impairments in binding, this disruption is stronger for the double mutants on the concave face of C_2B, possibly due to the fact the SNAREs are involved in distinct binding modes to different extents (sometimes alternatively), and the concave face of C_2B is involved in most binding modes. These results thereby provide strong support for the representative structures derived from the PCS data.

We wanted to test if the effects of the C_2B mutations correlate between SNARE complex binding and function in neurons, so we also analyzed PIP_2 binding for these mutants since the C_2B polybasic region has been implicated in PIP_2 binding independent of Ca^{2+} (Fukuda et al., 1994). C_2AB binding to PIP_2 in liposomes without Ca^{2+} is weak and not detected easily as seen in FRET assays (Radhakrishnan et al., 2009), so we again used a 1D ^{13}C-edited ^{1}H-NMR assay, especially because NMR spectra are highly sensitive to interactions with large species such as liposomes. Liposomes with 1% PIP_2 (1 mM total lipid) caused a 40% decrease in SMR intensity of the ^{13}C-edited ^{1}H-NMR spectra when added to WT ^{13}C-C_2AB (Figure 5.11D), showing that C_2AB does bind to

the liposomes in the absence of Ca^{2+}, albeit weakly. The single point mutants of ^{13}C-C_2AB in the polybasic region impaired binding strongly, although the control K354E,R388E double mutant had no effect on binding, while other double mutants abolished binding regardless of whether the side chains were on the concave face of C_2B (K313E,K325E; R322E,K325E) or not (K324E,K326E) (Figure 5.11D). These data clearly demonstrate that the Syt1 C_2B polybasic region mediates binding to PIP_2 as previously implicated. Interestingly, the PIP_2 binding is hindered more strongly and indiscriminately by mutations on the polybasic region than SNARE complex binding.

Ca^{2+}-dependent phospholipid binding to C_2AB is also critical for the function of Syt1 (Fernandez-Chacon et al., 2001). We tested selected double mutants for these effects as well using a assay that measures FRET from tryptophan residues on C_2AB to dansyl groups on the liposome surface (Fernandez et al., 2001) to measure binding as a function of Ca^{2+} (Figure 5.11E). The R322E,K325E mutant had the largest effect on the apparent K_ds seen in these titrations, and K313E,K325E and K324E,K326E had similar effects (Figure 5.11F).

5.3.6 Impaired Synaptotagmin-1/SNARE Complex Binding Correlates with Disruption of Synaptotagmin-1 Function

To investigate if the binding mode of the Syt1-SNARE complex above is physiologically relevant, we determined the ability of Syt1 to rescue neurotransmitter release in Syt1 KO mice neuronal cultures with electrophysiology using many of the Syt1

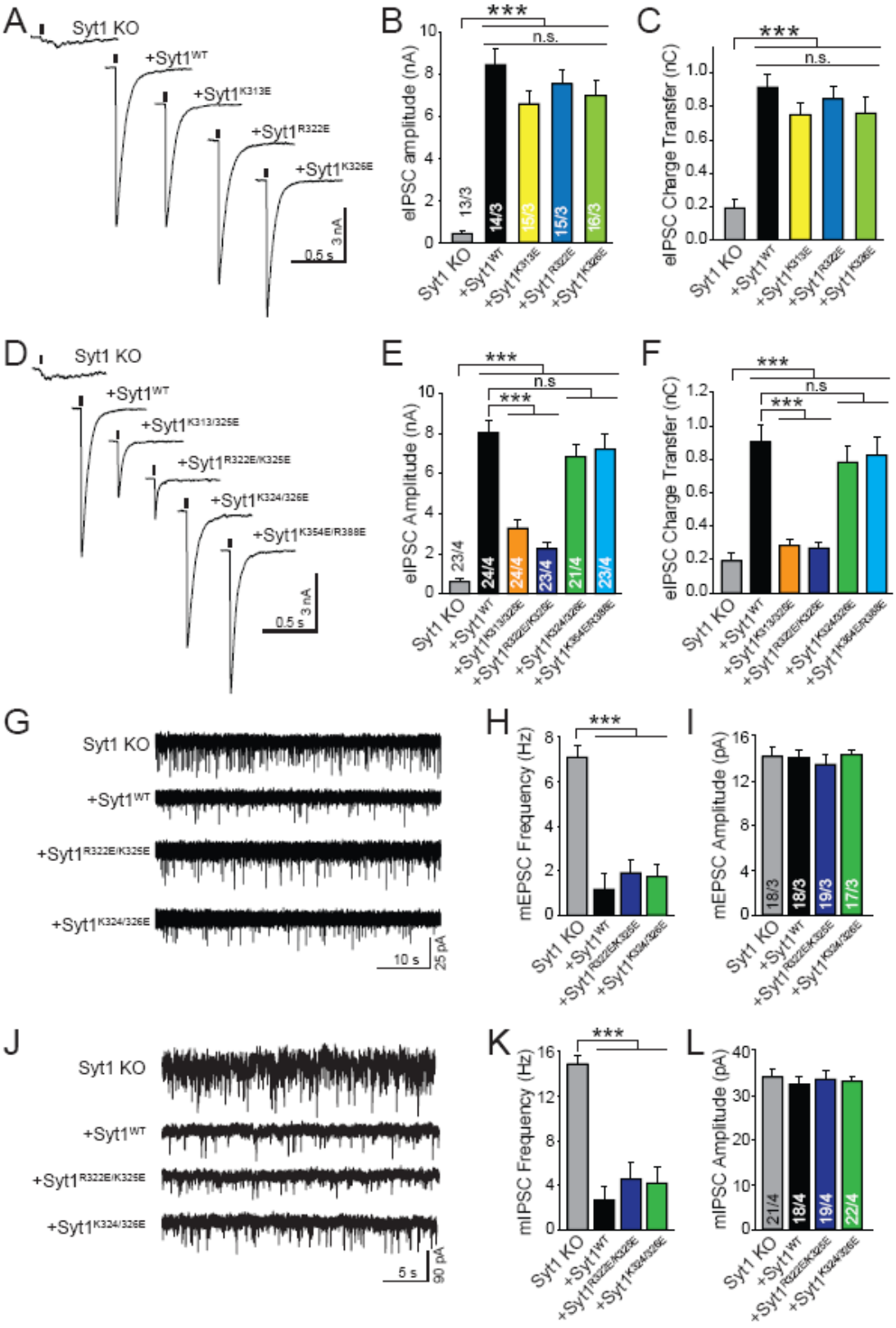
A
Syt1 KO
+Syt1WT
+Syt1K313E
+Syt1R322E
+Syt1K326E
3 nA
0.5 s
B
***
n.s.
eIPSC amplitude (nA)
13/3
14/3
15/3
15/3
16/3
Syt1 KO
+Syt1WT
+Syt1K313E
+Syt1R322E
+Syt1K326E
C
***
n.s.
eIPSC Charge Transfer (nC)
D
Syt1 KO
+Syt1WT
+Syt1K313/325E
+Syt1R322E/K325E
+Syt1K324/326E
+Syt1K354E/R388E
3 nA
0.5 s
E
***
n.s
***
eIPSC Amplitude (nA)
23/4
24/4
24/4
23/4
21/4
23/4
Syt1 KO
+Syt1WT
+Syt1K313/325E
+Syt1R322E/K325E
+Syt1K324/326E
+Syt1K354E/R388E
F
***
n.s
***
eIPSC Charge Transfer (nC)
G
Syt1 KO
+Syt1WT
+Syt1R322E/K325E
+Syt1K324/326E
10 s
25 pA
H
***
mEPSC Frequency (Hz)
Syt1 KO
+Syt1WT
+Syt1R322E/K325E
+Syt1K324/326E
I
mEPSC Amplitude (pA)
18/3
18/3
19/3
17/3
J
Syt1 KO
+Syt1WT
+Syt1R322E/K325E
+Syt1K324/326E
5 s
90 pA
K
***
mIPSC Frequency (Hz)
L
mIPSC Amplitude (pA)
21/4
18/4
19/4
22/4

Figure 5.13 Impaired Syt1 function in neurons correlates with impaired Syt1-SNARE complex binding. (A,D) Sample traces of evoked inhibitory postsynaptic currents (eIPSCs) observed in cultured Syt1 KO neurons without or with lentiviral expression of WT or mutant Syt1 as indicated. Stimulus onset is indicated by the tick mark. (B,C,E,F) Summary graphs of the eIPSC amplitudes and charge transfers observed in the rescue experiments with WT and mutant Syt1. (G,J) Sample traces of spontaneous release in excitatory (G) or inhibitory (J) neurons from Syt1 KO mice without or with lentiviral expression of WT Syt1 or selected Syt1 double mutants as indicated. (H,I,K,L) Summary graphs of spontaneous miniature EPSC (mEPSC) (H,I) and mIPSC (K,L) frequencies and amplitudes. All data are means ± SEM; numbers in bars indicate number of neurons/independent cultures analyzed. Statistical significance was assessed by oneway ANOVA (***, $p<0.001$; n.s., not significant).

mutants on the C_2B domain from our binding assays. Evoked release was severely abrogated in Syt1 KO neurons and rescued robustly with expression of full length WT Syt1 via lentiviral expression in these neurons (Figure 5.13A-C), as previously described (Xu et al., 2007). We tested three single mutants from the polybasic region of Syt1 in parallel (K313E, R322E, and K326E), finding that these mutants each rescued evoked release nearly as well as WT Syt1 (Figure 5.13A-C). These results show that single mutants, even single charge reversal mutants, do not strongly affect Syt1 function. These results match our findings that SNARE complex binding to C_2AB is not strongly impaired by the same single mutations in our NMR assay (Figure 5.12A,B).

We next wanted to see if the double mutants in basic residues had functionally correlated effects with our binding assays. Rescues of evoked release with the two double mutations on the Syt1 C_2B concave face (K313E,K325E and R322E,K325E) had strongly impaired release relative to WT Syt1, while on the other hand, rescue of evoked release with a double mutation not oriented towards the concave face (K324E,K326E) and with a control double mutation not near the binding site (K354E,R388E) were only very slightly impaired relative to WT Syt1 (Figure 5.13D-F). Since all double mutants were overexpressed to similar levels, protein overexpression does no account for the differences in rescue activity (Figure 5.14). Our C_2AB-SNARE complex binding assays (Figure 5.11B) correlate strikingly with the impairment of Syt1 function in neuronal cultures among all the mutants. On the other hand, the mutant effects on Ca^{2+}-independent PIP_2 binding or Ca^{2+}-dependent phospholipid binding (Figure 5.11D-F) only correlate partially with evoked release, as single mutants and the K324E,K326E mutant

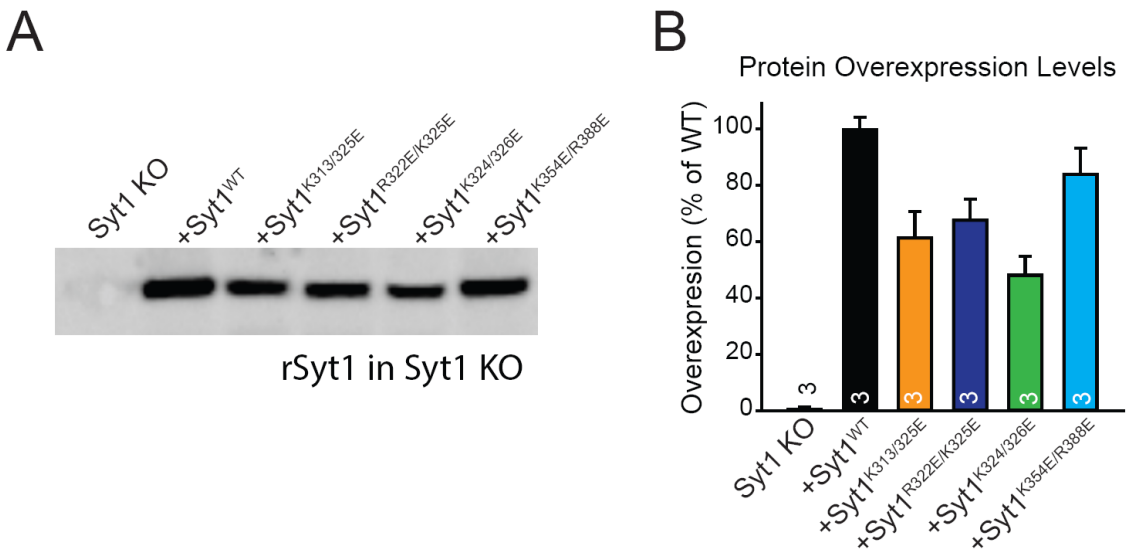

Figure 5.14 Levels of protein overexpresion for WT and double mutant Syt1 from rescue experiments. (A) Sample Western blots illustrating the overexpression levels of the WT and double mutant Syt1 in the rescue experiments. (B) Quantification of the protein overexpression levels in three different independent experiments. Related to Figure 5.13.

strongly impair PIP_2 binding but not evoked release, the K324E,K326E mutant affects Ca^{2+}-dependent phospholipid binding but not evoked release, and the K313E,K325E mutant has a slight effect on Ca^{2+}-dependent phospholipid binding but a large effect on evoked release. The binding mode of the Syt1-SNARE complex derived from our PCS data and verified in our binding assays therefore correlates well with the functional analysis from the rescue experiments.

To gain insights into which release step is affected by double mutations differentially, we analyzed Syt1 KO neurons rescued with R322E,K325E and K324E,K326E for spontaneous release. As previously described (Xu et al., 2009), WT Syt1 overexpression can suppress the large spontaneous release increase seen in both inhibitory and excitatory Syt1 KO neurons without changing the individual mIPSC or mEPSC amplitudes (Figure 5.13G-L). All double mutants suppressed the minis to a similar level as WT Syt1, suggesting that clamping the secondary Ca^{2+} sensor in Syt1 KO neurons mediating increased spontaneous release is not dependent on Syt1-SNARE complex interactions.

We also used the double mutants to measure the extracellular Ca^{2+}-dependence of evoked release in Syt1 KO neurons (Figure 5.15). The IPSC charge transfer and amplitude were observed to be strongly impaired in analysis of the Ca^{2+}-dependence of the R322E,K325E mutant. The extracellular Ca^{2+} EC50 also significantly increased comparing the rescue of WT Syt1 to the rescue of the R322E,K325E mutant (Figure 5.15D,H). The EC50 for the K324E,K326E mutant did not change significantly, but this mutant had slightly decreased release compared to WT at higher extracellular Ca^{2+}

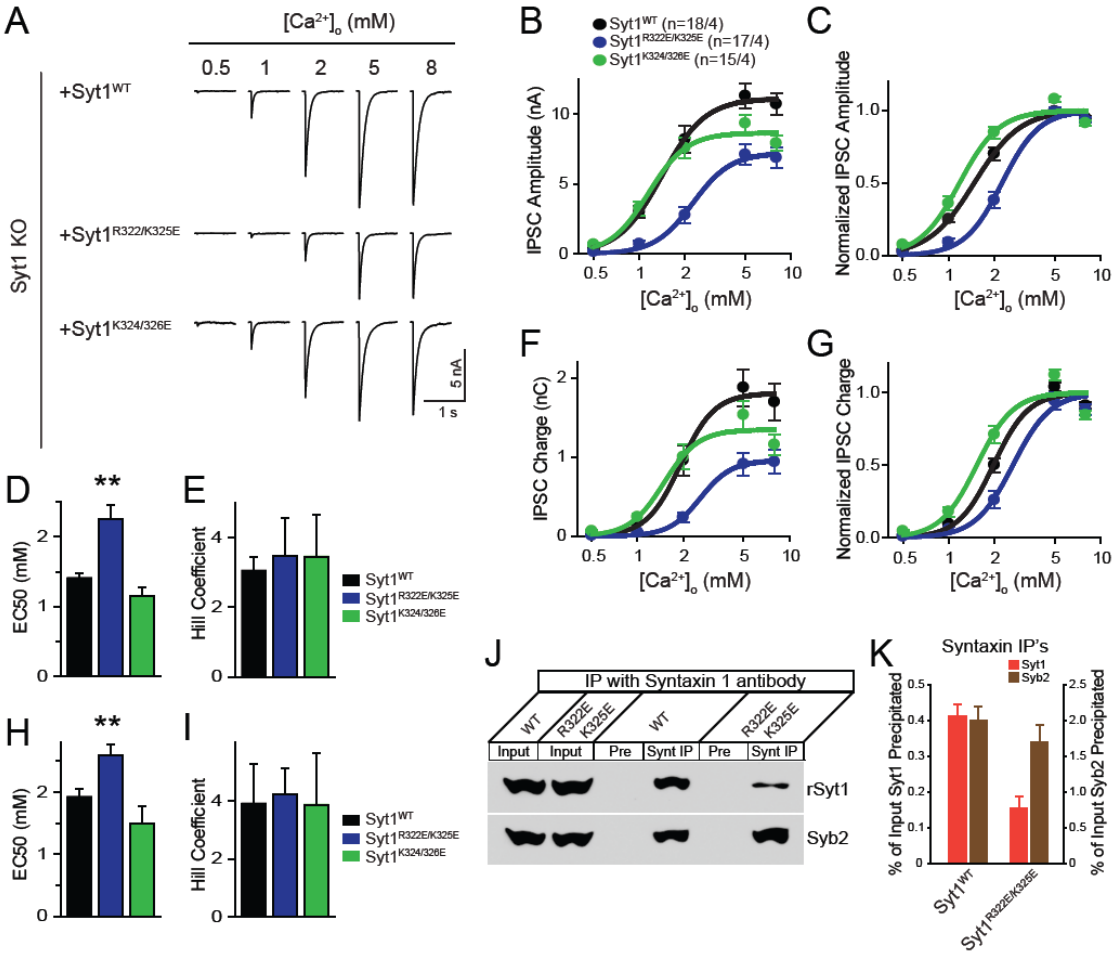

Figure 5.15 The Ca^{2+}-triggered step of release is impaired by disruption of Syt1-SNARE complex binding. (A) Sample traces of evoked IPSCs observed in Syt1 KO neurons rescued with WT or double mutant Syt1 as a function of extracellular Ca^{2+} concentration. (B,C,F,G) eIPSC amplitude (B,C) or charge transfer (F,G) observed as a function of extracellular Ca^{2+} concentration in the rescue experiments with WT or double mutant Syt1. The plots were fit with Hill equations. The data are presented in absolute values (B,F) or normalized to the limiting values at infinite extracellular Ca^{2+} derived from the fits (C,G). (D,E,H,I) Summary graphs of the EC50s and Hill coefficients

calculated from the data in panels (B,F). (J) Co-immunoprecipitation experiments with a polyclonal syntaxin-1 antibody. Co-immunoprecipitations were performed with Syt1 KO neurons rescued with WT or R322E,K325E mutant Syt1 and analyzed by Western blotting with monoclonal antibodies against Syt1 or Syb2. (K) Quantitative analysis of coimmunoprecipitation of WT and R322E,K325E mutant Syt1s with syntaxin-1 antibody. All data are means ± SEM. Statistical significance (D,E,H,I) was assessed by one-way ANOVA (**, $p<0.01$).

concentrations. Together, these observations suggest interactions in the Syt1-SNARE complex may have a key role in the Ca^{2+} triggering step of neurotransmitter release. To confirm that the impaired interactions seen in our binding assays with recombinant proteins was seen in neurons, we co-immunoprecipitated proteins with a syntaxin-1 antibody in Syt1 KO neurons using either WT Syt1 or the R322E,K325E mutant. The amount of Syt1 that co-immunoprecipitated with syntaxin-1 decreased by 62% comparing the R322E,K325E mutant to WT Syt1, without significantly affecting the co-immunoprecipitated control of synaptobrevin (Figure 5.15J,K), further supporting that impaired neurotransmitter release is caused by disruption of Syt1-SNARE interactions due to the R322E,K325E mutation.

5.4 Discussion

Syt1-SNARE interactions have been studied over the past twenty years and are thought to be key for coupling Ca^{2+} sensing to membrane fusion in neurotransmitter release. Lack of high-resolution structures of Syt1-SNARE complexes and conflicting results in different studies have, in part, made determining the basis for this coupling elusive. We demonstrate here the hurdles encountered when attempting to obtain such information, emerging in part due to the presence of more than one binding mode. After exploring many strategies, the approach above of using PCS measurements allowed us to largely surmount these difficulties to describe a dynamic structure representing the preferred binding mode of the Syt1-SNARE complex in solution, with biochemical and functional data supporting the relevance of these interactions. As discussed below, the

dynamic structure of the Syt1-SNARE complex may permit synchronous neurotransmitter to occur at the high speeds necessary for interneuronal communication, similar to examples of protein dynamics as a key for biological function that have been increasingly observed (Mittermaier and Kay, 2009). In addition, this dynamic structure suggests a clear mechanism of how the inhibition of release by the CpxI accessory helix is relieved by Syt1 and supports a model whereby the synaptic vesicle and plasma members are brought together upon Ca^{2+} influx by Syt1 in cooperation with the SNAREs to induce membrane fusion (Figures 5.9E and 5.16).

The dynamic nature of the C_2B-SNARE complex prevents us from using a single structure to fit all the PCS data in our analysis, which hinders use of current computational tools to interpret the data fully. However, by manually matching the positive and negative PCS pattern on the C_2B domain to lobes for the tensor on the SNARE complex, we can approximately but unambiguously obtain the preferred orientation and location of the C_2B relative to the SNARE complex. The SC166Dy PCSs obtained were particularly useful as the pattern of PCSs on C_2B strongly restrain its position on the SNARE complex for the 166 manual or MD models (Figure 5.5E, 5.7D). Any movement from this position would worsen the match of the PCS patterns, cause loss of contact between the C_2B and SNARE complex, or create strong steric clashes. The size of measured PCSs are dampened by large motions of the C_2B relative to the SNARE complex, so any one structure cannot represent fully the binding mode dynamics in solution, but the models from the PCS data and MD simulations assist in determining

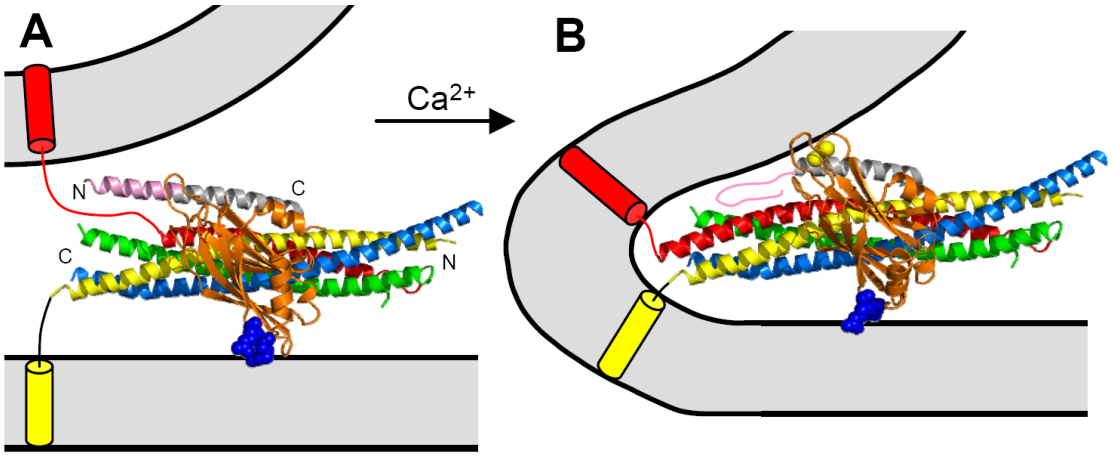

Figure 5.16 Model for the mechanism of Ca^{2+}-dependent neurotransmitter release triggered by Syt1 and the SNAREs in an interplay with CpxI. (A) Model of a primed state with a partially assembled SNARE complex where the C-terminus of the synaptobrevin SNARE motif remains flexible. CpxI(26-83) is shown according to the crystal structure of the CpxI(26-83)-SNARE complex (PDB accession code 1KIL). The position of Ca^{2+}-free C_2B corresponds to that of the 166 MD model. R398 and R399 at the bottom of C_2B are shown as dark blue spheres and bound to the plasma membrane. (B) Model of a fused state with a fully assembled SNARE complex after Ca^{2+} influx, with C_2B bound to the SNARE complex and to both membranes. Ca^{2+} ions are represented by yellow spheres. Key aspects of this model are: i) before Ca^{2+} influx, Syt1 binds to a partially assembled SNARE complex through the concave, basic side of the C_2B domain and, in this primed state, the CpxI accessory helix repels the vesicle membrane, hindering membrane fusion; ii) Ca^{2+} binding to C_2B induces binding to the vesicle membrane, forcing the inhibitory accessory helix to melt away; iii) simultaneous

binding of R398-R399 of C_2B to the plasma membrane and of the Ca^{2+}-binding loops to the vesicle membrane forces the two membranes together which, together with full zippering of the SNARE complex, induces membrane fusion; iv) these actions of C_2B may require re-orientation with respect to the SNARE complex, which would be facilitated by the dynamic nature of the C_2B-SNARE complex interactions. This mechanism is consistent with the 166 MD model and 41 manual model, which we take as representatives of the preferred orientations defined by the two PCS datasets, as well as with many of the structures visited during our MD simulations. Hence, the proposed mechanism relies on the overall dynamic binding mode rather than on a biased choice of a particular model.

the interactions that mediate C_2B-SNARE complex binding. Importantly, the binding mode seen in these models reveals key features of how Syt1 and the SNAREs may work together in neurotransmitter release and provides a natural explanation for the dynamic relationship between the proteins.

The main data used for structural analysis was acquired with 125 mM KSCN and the C_2B mutant R398Q,R399Q. However, this binding mode is supported by a wide range of data from PCSs measured with WT and C_2B and C_2AB (Figure 5.4A,B,D,E), which parallel the data within experimental error, to binding assays for mutations C_2AB and the SNARE complex (Figure 5.11B,C) to Syt1 KO neuron rescues (Figures 5.13,5.15) to syntaxin co-immunoprecipitation data (Figure 5.15J,K). Many previous studies also agree with the binding mode, although these results may have previously been thought to be contradictory. The binging region of Syt1 was ascribed to SNAP-25 (Gerona et al., 2000) and syntaxin-1(Bennett et al., 1992), but our data now show that both SNARE domains contribute to Syt1 binding due to the dynamic nature of the interaction. Several studies mapped the binding region for Syt1 on the SNARE complex specifically to the acidic residues D51, E52, and E55 on SNAP-25 (Kim et al., 2012; Rickman et al., 2006). Our studies find that these residues are indeed important to fully mediate the Syt1-SNARE complex interaction and that the acidic residues E224, E228, D231, and E234 on the syntaxin-1 SNARE domain also contribute to binding. A wide range of studies implicating the polybasic β-strand on the C_2B domain (Dai et al., 2007; Lai et al., 2011; Malsam et al., 2012; Rickman et al., 2004; Rickman et al., 2006; Zhou et al., 2013a) agree with our findings well, but we distinguish key residues on this strand,

R322, K325, and K327 (plus K313 on the adjacent strand), as critical interaction partners on the concave face of the C_2B β-sandwich, while K324 and K326 that have side chains pointed away from the concave face do not have as prominent a role for the interaction. In addition, our data agree strongly with perturbation of spin labels measured by EPR at 21 residues on C_2AB used to map the binding interface on Syt1 for the SNARE complex without KSCN, with residues 325 and 327 showing the strongest perturbations, residue 326 showing less pronounced perturbations, and additional perturbations at the bottom of C_2B and on the Ca^{2+}-binding loops of C_2A (Lai et al., 2011) that we saw as weak binding sites in our ^{1}H-^{15}N HSQC spectra (Figure 5.1). Altogether, these results add strong support for the conclusions drawn from our study of the structures and interactions of the Syt1-SNARE complex, including the major binding modes, weaker binding sites, and validity of using KSCN to assist our experiments.

From the structural representations of the Syt1-SNARE complex we derive, a comprehensible understanding emerges of how the CpxI inhibition of neurotransmitter release is relieved by Syt1 (Giraudo et al., 2006; Schaub et al., 2006; Tang et al., 2006). The SNARE complex can simultaneously bind CpxI(26-83) and Syt1 C_2AB in solution (Xu et al., 2013) due to distinct binding sites as explained above, but steric clashes of CpxI(26-83) accessory helix with membranes makes CpxI(26-83) and Syt1 appear to compete on membranes (Figure 5.9E). Considering the putative primed state consisting of a partially assembled SNARE complex with CpxI bound, the repulsion of the negative charged membrane from the negatively charged CpxI accessory helix provides an clear explanation for the inhibition (Trimbuch et al., 2014) (Figure 5.16A). In our model, we

propose that the binding of Syt1 C_2B to the vesicle membrane upon Ca^{2+} influx causes the CpxI accessory helix to melt (Figure 5.16B), assisted by its flexibility (Chen et al., 2002). CpxI dissociation is not required by this rearrangement which is nevertheless prevented by the N- and/or C-terminal CpxI sequence (not shown in Figure 5.16) (Xu et al., 2013), allowing CpxI to still have an active role in fusion.

In our structure, the SNARE complex, upon binding Syt1, positions the C_2B domain ideally to bind the plasma membrane through the bottom R398-R399 side chains and the vesicle membrane through the upper Ca^{2+}-binding loops (Figure 5.16B). SNARE complex zippering and this action of Syt1 can occur concurrently, allowing membrane fusion and neurotransmitter release to occur quickly in sync with these events. Syt1 simultaneously binding two membranes brings them within 4 nm (Arac et al., 2006; Seven et al., 2013), which this model is based on in part and which accounts for the crucial role of R398-R399 from the C_2B domain in neurotransmitter release and SNARE-dependent lipid mixing assays (Xue et al., 2008). Several results from this study and others suggest that the interactions between the acidic regions of syntaxin-1 and SNAP-25 with the C_2B polybasic region can occur prior to Ca^{2+} influx (Kim et al., 2012; Rickman et al., 2004; Rickman et al., 2006), and the model here postulates this binding along with binding of C_2B to two membranes upon Ca^{2+} influx. The interaction is weaker without Ca^{2+} present, although co-localization probably favors the interaction and binding of R398-R399 to the plasma membrane could add further support to generate the primed state of C_2B (Figure 5.16A), ready to bridge the two membranes by binding the vesicle membrane upon Ca^{2+} influx, thereby relieving the inhibition of membrane fusion

by CpxI (Figure 5.16B). Facilitating this rearrangement may be the reason behind the dynamic nature of interaction between Syt1 C_2B and the SNARE complex.

A large amount of experimental evidence is explained by our Syt1-SNARE complex structure and the Figure 5.16 model, but testing their relevance and addressing several unresolved issues will require further research. The double mutants of polybasic residues on Syt1 C_2B have a clear correlation in our SNARE complex binding assays (Figure 5.11B) and in our Syt1 KO rescues (Figure 5.13D-F), but the R322E,K325E mutant also has correlation between Ca^{2+}-dependent phospholipid binding (Figure 5.11E,F) and the Ca^{2+}-dependent release in neurons (Figure 5.15). However, there is only partial correlation between decreased Ca^{2+}-dependent phospholipid binding and rescue of Syt1 function when looking at the mutants together (Figures 5.11E,F, and 5.13), which argues against the idea that the double mutants impair neurotransmitter release due to their effects on phospholipid binding. The fact that mutations in Syt1 often affect both phospholipid and SNARE complex binding make delineating these functions difficult, as the presence of these two factors likely influence each other and physiological binding modes may be changed by removing either component. Additional binding modes of Syt1 and the SNAREs, although less populated in solution, may also be important for function, such as residues in the SNAP-25 C-terminus that were critical for Syt1 binding in some but not all studies (Dai et al., 2007; Kim et al., 2012; Zhang et al., 2002) and the region at the bottom of the C_2B domain near R398-R399 that weakly binds the SNARE complex [(Lai et al., 2011; Zhou et al., 2013a); Figure 5.1]. Aggregation of C_2AB with the SNARE complex is contributed to by R398-R399 (Zhou et al., 2013a), and the ability

of C_2AB to bring membranes together (Arac et al., 2006) but not the ability to compete with CpxI(26-83) on membranes (Xue et al., 2008) is impaired by mutating these arginines, so we think the real target of R398-R399 *in vivo* is the membranes (Figure 5.16). The bottom of the C_2B domain was placed near the SNARE complex in single-molecule FRET studies however (Choi et al., 2010).

Ca^{2+} binding to the Syt1 C_2B domain is more important in our model than binding to the C_2A domain (Mackler and Reist, 2001), but the C_2A domain is important for normal release (Fernandez-Chacon et al., 2001; Lee et al., 2013; Shin et al., 2009). The C_2A domain emerges at the N-terminus of C_2B, opposite to the side that binds the SNARE complex in our structure (Figure 5.9E). C_2A could interact with the vesicle and/or plasma membrane in this location where it could help trigger release in cooperation with the action of C_2B. Note that C_2A-SNARE interactions have been suggested to be important for release (Lynch et al., 2007; Pang et al., 2006), but weak C_2A-SNARE interactions can contribute to C_2AB-SNARE complex aggregation (Zhou et al., 2013a), although these weak interactions may still be important functionally.

Though challenging, studies of the interactions between Syt1 and the SNARE complex on membranes or even between two membranes ideally will be necessary to resolve these remaining questions and determine the overall Syt1-SNARE complex orientation. In our model, the C_2B Ca^{2+}-binding loops face the vesicle, but they could realistically face the plasma membrane if the SNARE complex is rotated 180° about its long axis, depending on SNARE juxtamembrane regions conformation. The effect of phospholipids such as PIP_2 on the binding mode of the Syt1-SNARE complex will also

need to be examined. Despite these remaining questions, the dynamic structure of the Syt1-SNARE complex we present here is a major breakthrough showing the preferred binding mode in solution that explains much of the previously published data and serves as a guide for future efforts in this field.

Chapter 6 Future Directions

Synaptic vesicle fusion depends on the SNARE complex and synaptotagmin, and the work described in this dissertation reveals the dynamics and major interactions between these proteins. Future work will evaluate hypotheses based on the models of the Syt1-SNARE complex we present. The difficulty in this analysis comes largely because to evaluate the conformations and binding modes of the complex, membranes will need to be included, which are not often used in structural biology.

We have presented evaluation of the structures and conformations of membrane associated proteins on nanodiscs (Chapters 2, 3, and 4). This work can be considered preliminary, as the inclusion of several proteins on these membranes will be necessary to fully understand the synaptic vesicle fusion machinery. Also, synaptic vesicle fusion takes places between two membranes, both of different lipid composition, which complicates matters furthers. The synaptic vesicle and plasma membranes are even at the extremes of curvature and content, with the plasma membrane being almost completely flat and synaptic vesicles having high curvature, properties which will affect their biophysical characterization and make reconstitution more difficult. Nonetheless, nanodiscs represent a good system to study the synaptic vesicle fusion machinery by NMR, EPR, FRET, and cryo-EM. In addition, liposomes can be included in these systems, although the studies by NMR which have been presented here can only utilize liposomes under limited circumstances (see Chapter 2).

Ideally, the synaptic vesicle machinery should be studied between two

membranes that have properties of plasma membranes and synaptic vesicles. However, producing these samples is near to a technical impossibility currently as the included proteins naturally will fuse the two membranes together. We still have appropriate alternatives that can reveal much about these systems. The Syt1-SNARE complex could be realistically studied on one nanodisc or perhaps between two nanodiscs by NMR in similar studies to the ones presented here.

The models of the Syt1-SNARE complex (Chapter 5) also led to hypotheses of how these proteins may lead to fusion. One hypothesis we would like to explore is if the dynamic interaction between the Syt1-SNARE complex is a primary determinant in fusion. We hypothesize that by creating acidic to basic double mutations on the SNARE complex with complementing basic to acidic mutations we may be able to create a Syt1-SNARE complex that can interact, but lose much of its dynamics. If evoked release in neurons is retained with these mutations, it would rule out our hypothesis that dynamics of the Syt1-SNARE complex is important for synaptic vesicle fusion.

Another possibility is examining the synaptic vesicle machinery using cryo-electron microscopy (cryo-EM). Recent developments have improved the resolution even for protein complexes without symmetry (Lu et al., 2014). Although the small size of the Syt1-SNARE complex may still create difficulties for these methods, the use of nanodiscs, antibodies, or other larger synaptic proteins (e.g. Munc13) may allow for localization of these proteins in cyro-EM samples between membranes that reproduce many or most of their native properties. Direct visualization by this method may also allow for classification of ensembles into clusters to better determine the conformations

and populations of the synaptic vesicle machinery.

The research presented here explains a large amount of properties of the Ca^{2+} dependent exocytosis machinery that have been revealed over the past 20 years. These proteins are extremely difficult to study and future research will also run into problems trying to study the reconstituted system, but technical advances alongside the methods and models presented here should assist these efforts. In addition, reconstituted components that more closely resemble the entire synaptic vesicle machinery in neurons have been seen in studies recently. Using all these proteins together increases the likelihood of obtaining results that faithfully represent the full system, so thus studies in the near future will likely reveal a more complete picture of the mechanisms behind these proteins.

REFERENCES

Abascal, J.L., and Vega, C. (2005). A general purpose model for the condensed phases of water: TIP4P/2005. J Chem Phys *123*, 234505.

Arac, D., Chen, X., Khant, H.A., Ubach, J., Ludtke, S.J., Kikkawa, M., Johnson, A.E., Chiu, W., Sudhof, T.C., and Rizo, J. (2006). Close membrane-membrane proximity induced by Ca(2+)-dependent multivalent binding of synaptotagmin-1 to phospholipids. Nat Struct Mol Biol *13*, 209-217.

Arac, D., Murphy, T., and Rizo, J. (2003). Facile detection of protein-protein interactions by one-dimensional NMR spectroscopy. Biochemistry *42*, 2774-2780.

Azevedo, F.A., Carvalho, L.R., Grinberg, L.T., Farfel, J.M., Ferretti, R.E., Leite, R.E., Jacob Filho, W., Lent, R., and Herculano-Houzel, S. (2009). Equal numbers of neuronal and nonneuronal cells make the human brain an isometrically scaled-up primate brain. J Comp Neurol *513*, 532-541.

Bacaj, T., Wu, D., Yang, X., Morishita, W., Zhou, P., Xu, W., Malenka, R.C., and Sudhof, T.C. (2013). Synaptotagmin-1 and synaptotagmin-7 trigger synchronous and asynchronous phases of neurotransmitter release. Neuron *80*, 947-959.

Banerjee, S., Huber, T., and Sakmar, T.P. (2008). Rapid incorporation of functional rhodopsin into nanoscale apolipoprotein bound bilayer (NABB) particles. J Mol Biol *377*, 1067-1081.

Bashir, Q., Scanu, S., and Ubbink, M. (2011). Dynamics in electron transfer protein complexes. FEBS J *278*, 1391-1400.

Basu, J., Shen, N., Dulubova, I., Lu, J., Guan, R., Guryev, O., Grishin, N.V., Rosenmund, C., and Rizo, J. (2005). A minimal domain responsible for Munc13 activity. Nat Struct Mol Biol *12*, 1017-1018.

Battiste, J.L., and Wagner, G. (2000). Utilization of site-directed spin labeling and high-resolution heteronuclear nuclear magnetic resonance for global fold determination of large proteins with limited nuclear overhauser effect data. Biochemistry *39*, 5355-5365.

Beaudoin, G.M., 3rd, Lee, S.H., Singh, D., Yuan, Y., Ng, Y.G., Reichardt, L.F., and Arikkath, J. (2012). Culturing pyramidal neurons from the early postnatal mouse hippocampus and cortex. Nat Protoc *7*, 1741-1754.

Bennett, M.K., Calakos, N., and Scheller, R.H. (1992). Syntaxin: a synaptic protein implicated in docking of synaptic vesicles at presynaptic active zones. Science *257*, 255-259.

Best, R.B., and Mittal, J. (2010). Protein simulations with an optimized water model: cooperative helix formation and temperature-induced unfolded state collapse. J Phys Chem B *114*, 14916-14923.

Bhalla, A., Chicka, M.C., Tucker, W.C., and Chapman, E.R. (2006). Ca(2+)-synaptotagmin directly regulates t-SNARE function during reconstituted membrane fusion. Nat Struct Mol Biol *13*, 323-330.

Boswell, K.L., James, D.J., Esquibel, J.M., Bruinsma, S., Shirakawa, R., Horiuchi, H., and Martin, T.F. (2012). Munc13-4 reconstitutes calcium-dependent SNARE-mediated membrane fusion. J Cell Biol *197*, 301-312.

Bowen, M., and Brunger, A.T. (2006). Conformation of the synaptobrevin transmembrane domain. Proc Natl Acad Sci U S A *103*, 8378-8383.

Bowen, M.E., Weninger, K., Ernst, J., Chu, S., and Brunger, A.T. (2005). Single-molecule studies of synaptotagmin and complexin binding to the SNARE complex. Biophys J *89*, 690-702.

Brewer, K.D., Li, W., Horne, B.E., and Rizo, J. (2011). Reluctance to membrane binding enables accessibility of the synaptobrevin SNARE motif for SNARE complex formation. Proc Natl Acad Sci U S A *108*, 12723-12728.

Bronk, P., Deak, F., Wilson, M.C., Liu, X., Sudhof, T.C., and Kavalali, E.T. (2007). Differential effects of SNAP-25 deletion on Ca2+ -dependent and Ca2+ -independent neurotransmission. J Neurophysiol *98*, 794-806.

Brunger, A.T. (2005). Structure and function of SNARE and SNARE-interacting proteins. Q Rev Biophys *38*, 1-47.

Brunger, A.T., Weninger, K., Bowen, M., and Chu, S. (2009). Single-molecule studies of the neuronal SNARE fusion machinery. Annu Rev Biochem *78*, 903-928.

Burkhardt, P., Hattendorf, D.A., Weis, W.I., and Fasshauer, D. (2008). Munc18a controls SNARE assembly through its interaction with the syntaxin N-peptide. EMBO J *27*, 923-933.

Camilloni, C., Cavalli, A., and Vendruscolo, M. (2013). Assessment of the use of NMR chemical shifts as replica-averaged structural restraints in molecular dynamics simulations to characterize the dynamics of proteins. J Phys Chem B *117*, 1838-1843.

Camilloni, C., Robustelli, P., De Simone, A., Cavalli, A., and Vendruscolo, M. (2012). Characterization of the conformational equilibrium between the two major substates of RNase A using NMR chemical shifts. J Am Chem Soc *134*, 3968-3971.

Camilloni, C., and Vendruscolo, M. (2014). Statistical mechanics of the denatured state of a protein using replica-averaged metadynamics. J Am Chem Soc *136*, 8982-8991.

Card, P.B., Erbel, P.J., and Gardner, K.H. (2005). Structural basis of ARNT PAS-B dimerization: use of a common beta-sheet interface for hetero- and homodimerization. J Mol Biol *353*, 664-677.

Carr, C.M., and Rizo, J. (2010). At the junction of SNARE and SM protein function. Curr Opin Cell Biol *22*, 488-495.

Catterall, W.A. (2011). Voltage-gated calcium channels. Cold Spring Harb Perspect Biol *3*, a003947.

Cavalli, A., Camilloni, C., and Vendruscolo, M. (2013). Molecular dynamics simulations with replica-averaged structural restraints generate structural ensembles according to the maximum entropy principle. J Chem Phys *138*, 094112.

Chapman, E.R. (2008). How does synaptotagmin trigger neurotransmitter release? Annu Rev Biochem *77*, 615-641.

Chapman, E.R., and Davis, A.F. (1998). Direct interaction of a Ca2+-binding loop of synaptotagmin with lipid bilayers. J Biol Chem *273*, 13995-14001.

Chapman, E.R., Hanson, P.I., An, S., and Jahn, R. (1995). Ca2+ regulates the interaction between synaptotagmin and syntaxin 1. J Biol Chem *270*, 23667-23671.

Chen, X., Arac, D., Wang, T.M., Gilpin, C.J., Zimmerberg, J., and Rizo, J. (2006). SNARE-mediated lipid mixing depends on the physical state of the vesicles. Biophys J *90*, 2062-2074.

Chen, X., Lu, J., Dulubova, I., and Rizo, J. (2008). NMR analysis of the closed conformation of syntaxin-1. J Biomol NMR *41*, 43-54.

Chen, X., Tang, J., Sudhof, T.C., and Rizo, J. (2005). Are neuronal SNARE proteins Ca2+ sensors? J Mol Biol *347*, 145-158.

Chen, X., Tomchick, D.R., Kovrigin, E., Arac, D., Machius, M., Sudhof, T.C., and Rizo, J. (2002). Three-dimensional structure of the complexin/SNARE complex. Neuron *33*, 397-409.

Chernomordik, L.V., and Kozlov, M.M. (2003). Protein-lipid interplay in fusion and fission of biological membranes. Annu Rev Biochem *72*, 175-207.

Chicka, M.C., Hui, E., Liu, H., and Chapman, E.R. (2008). Synaptotagmin arrests the SNARE complex before triggering fast, efficient membrane fusion in response to Ca2+. Nat Struct Mol Biol *15*, 827-835.

Choi, U.B., Strop, P., Vrljic, M., Chu, S., Brunger, A.T., and Weninger, K.R. (2010). Single-molecule FRET-derived model of the synaptotagmin 1-SNARE fusion complex. Nat Struct Mol Biol *17*, 318-324.

Clore, G.M., and Iwahara, J. (2009). Theory, practice, and applications of paramagnetic relaxation enhancement for the characterization of transient low-population states of biological macromolecules and their complexes. Chem Rev *109*, 4108-4139.

Cohen, F.S., and Melikyan, G.B. (2004). The energetics of membrane fusion from binding, through hemifusion, pore formation, and pore enlargement. J Membr Biol *199*, 1-14.

Dai, H., Shen, N., Arac, D., and Rizo, J. (2007). A quaternary SNARE-synaptotagmin-Ca2+-phospholipid complex in neurotransmitter release. J Mol Biol *367*, 848-863.

Damer, C.K., and Creutz, C.E. (1994). Synergistic membrane interactions of the two C2 domains of synaptotagmin. J Biol Chem *269*, 31115-31123.

de la Cruz, L., Nguyen, T.H., Ozawa, K., Shin, J., Graham, B., Huber, T., and Otting, G. (2011). Binding of low molecular weight inhibitors promotes large conformational changes in the dengue virus NS2B-NS3 protease: fold analysis by pseudocontact shifts. J Am Chem Soc *133*, 19205-19215.

De Simone, A., Montalvao, R.W., and Vendruscolo, M. (2011). Determination of Conformational Equilibria in Proteins Using Residual Dipolar Couplings. J Chem Theory Comput *7*, 4189-4195.

Delaglio, F., Grzesiek, S., Vuister, G.W., Zhu, G., Pfeifer, J., and Bax, A. (1995). NMRPipe: a multidimensional spectral processing system based on UNIX pipes. J Biomol NMR *6*, 277-293.

Denisov, I.G., Grinkova, Y.V., Lazarides, A.A., and Sligar, S.G. (2004). Directed self-assembly of monodisperse phospholipid bilayer Nanodiscs with controlled size. J Am Chem Soc *126*, 3477-3487.

Dietrich, D., Kirschstein, T., Kukley, M., Pereverzev, A., von der Brelie, C., Schneider, T., and Beck, H. (2003). Functional specialization of presynaptic Cav2.3 Ca2+ channels. Neuron *39*, 483-496.

Do, T.N., Carloni, P., Varani, G., and Bussi, G. (2013). RNA/Peptide Binding Driven by Electrostatics-Insight from Bidirectional Pulling Simulations. J Chem Theory Comput *9*, 1720-1730.

Dulubova, I., Khvotchev, M., Liu, S., Huryeva, I., Sudhof, T.C., and Rizo, J. (2007). Munc18-1 binds directly to the neuronal SNARE complex. Proc Natl Acad Sci U S A *104*, 2697-2702.

Dulubova, I., Sugita, S., Hill, S., Hosaka, M., Fernandez, I., Sudhof, T.C., and Rizo, J. (1999). A conformational switch in syntaxin during exocytosis: role of munc18. EMBO J *18*, 4372-4382.

Ellena, J.F., Liang, B., Wiktor, M., Stein, A., Cafiso, D.S., Jahn, R., and Tamm, L.K. (2009). Dynamic structure of lipid-bound synaptobrevin suggests a nucleation-propagation mechanism for trans-SNARE complex formation. Proc Natl Acad Sci U S A *106*, 20306-20311.

Farrow, N.A., Muhandiram, R., Singer, A.U., Pascal, S.M., Kay, C.M., Gish, G., Shoelson, S.E., Pawson, T., Forman-Kay, J.D., and Kay, L.E. (1994). Backbone dynamics of a free and phosphopeptide-complexed Src homology 2 domain studied by 15N NMR relaxation. Biochemistry *33*, 5984-6003.

Fasshauer, D., and Margittai, M. (2004). A transient N-terminal interaction of SNAP-25 and syntaxin nucleates SNARE assembly. J Biol Chem *279*, 7613-7621.

Fasshauer, D., Otto, H., Eliason, W.K., Jahn, R., and Brunger, A.T. (1997). Structural changes are associated with soluble N-ethylmaleimide-sensitive fusion protein attachment protein receptor complex formation. J Biol Chem *272*, 28036-28041.

Fasshauer, D., Sutton, R.B., Brunger, A.T., and Jahn, R. (1998). Conserved structural features of the synaptic fusion complex: SNARE proteins reclassified as Q- and R-SNAREs. Proc Natl Acad Sci U S A *95*, 15781-15786.

Fernandez-Chacon, R., Konigstorfer, A., Gerber, S.H., Garcia, J., Matos, M.F., Stevens, C.F., Brose, N., Rizo, J., Rosenmund, C., and Sudhof, T.C. (2001). Synaptotagmin I functions as a calcium regulator of release probability. Nature *410*, 41-49.

Fernandez, I., Arac, D., Ubach, J., Gerber, S.H., Shin, O., Gao, Y., Anderson, R.G., Sudhof, T.C., and Rizo, J. (2001). Three-dimensional structure of the synaptotagmin 1 C2B-domain: synaptotagmin 1 as a phospholipid binding machine. Neuron *32*, 1057-1069.

Fernandez, I., Ubach, J., Dulubova, I., Zhang, X., Sudhof, T.C., and Rizo, J. (1998). Three-dimensional structure of an evolutionarily conserved N-terminal domain of syntaxin 1A. Cell *94*, 841-849.

Fiebig, K.M., Rice, L.M., Pollock, E., and Brunger, A.T. (1999). Folding intermediates of SNARE complex assembly. Nat Struct Biol *6*, 117-123.

Fu, B., Sahakyan, A.B., Camilloni, C., Tartaglia, G.G., Paci, E., Caflisch, A., Vendruscolo, M., and Cavalli, A. (2014). ALMOST: an all atom molecular simulation toolkit for protein structure determination. J Comput Chem *35*, 1101-1105.

Fujiwara, T., Mishima, T., Kofuji, T., Chiba, T., Tanaka, K., Yamamoto, A., and Akagawa, K. (2006). Analysis of knock-out mice to determine the role of HPC-1/syntaxin 1A in expressing synaptic plasticity. J Neurosci *26*, 5767-5776.

Fukuda, M., Aruga, J., Niinobe, M., Aimoto, S., and Mikoshiba, K. (1994). Inositol-1,3,4,5-tetrakisphosphate binding to C2B domain of IP4BP/synaptotagmin II. J Biol Chem *269*, 29206-29211.

Fykse, E.M., and Fonnum, F. (1996). Amino acid neurotransmission: dynamics of vesicular uptake. Neurochem Res *21*, 1053-1060.

Galli, T., and Haucke, V. (2004). Cycling of synaptic vesicles: how far? How fast! Sci STKE *2004*, re19.

Gao, Y., Zorman, S., Gundersen, G., Xi, Z., Ma, L., Sirinakis, G., Rothman, J.E., and Zhang, Y. (2012). Single reconstituted neuronal SNARE complexes zipper in three distinct stages. Science *337*, 1340-1343.

Gelis, I., Bonvin, A.M., Keramisanou, D., Koukaki, M., Gouridis, G., Karamanou, S., Economou, A., and Kalodimos, C.G. (2007). Structural basis for signal-sequence recognition by the translocase motor SecA as determined by NMR. Cell *131*, 756-769.

Geppert, M., Goda, Y., Hammer, R.E., Li, C., Rosahl, T.W., Stevens, C.F., and Sudhof, T.C. (1994). Synaptotagmin I: a major Ca2+ sensor for transmitter release at a central synapse. Cell *79*, 717-727.

Gerona, R.R., Larsen, E.C., Kowalchyk, J.A., and Martin, T.F. (2000). The C terminus of SNAP25 is essential for Ca(2+)-dependent binding of synaptotagmin to SNARE complexes. J Biol Chem *275*, 6328-6336.

Giralt, E., Rizo, J., and Pedroso, E. (1984). Application of Gel-Phase C-13-Nmr to Monitor Solid-Phase Peptide-Synthesis. Tetrahedron *40*, 4141-4152.

Giraudo, C.G., Eng, W.S., Melia, T.J., and Rothman, J.E. (2006). A clamping mechanism involved in SNARE-dependent exocytosis. Science *313*, 676-680.

Giraudo, C.G., Garcia-Diaz, A., Eng, W.S., Chen, Y., Hendrickson, W.A., Melia, T.J., and Rothman, J.E. (2009). Alternative zippering as an on-off switch for SNARE-mediated fusion. Science *323*, 512-516.

Gluck, J.M., Wittlich, M., Feuerstein, S., Hoffmann, S., Willbold, D., and Koenig, B.W. (2009). Integral membrane proteins in nanodiscs can be studied by solution NMR spectroscopy. J Am Chem Soc *131*, 12060-12061.

Goto, N.K., Gardner, K.H., Mueller, G.A., Willis, R.C., and Kay, L.E. (1999). A robust and cost-effective method for the production of Val, Leu, Ile (delta 1) methyl-protonated 15N-, 13C-, 2H-labeled proteins. J Biomol NMR *13*, 369-374.

Graham, B., Loh, C.T., Swarbrick, J.D., Ung, P., Shin, J., Yagi, H., Jia, X., Chhabra, S., Barlow, N., Pintacuda, G., *et al.* (2011). DOTA-amide lanthanide tag for reliable generation of pseudocontact shifts in protein NMR spectra. Bioconjug Chem *22*, 2118-2125.

Guan, K.L., and Dixon, J.E. (1991). Eukaryotic proteins expressed in Escherichia coli: an improved thrombin cleavage and purification procedure of fusion proteins with glutathione S-transferase. Anal Biochem *192*, 262-267.

Guan, R., Dai, H., and Rizo, J. (2008). Binding of the Munc13-1 MUN domain to membrane-anchored SNARE complexes. Biochemistry *47*, 1474-1481.

Guo, T., Gong, L.C., and Sui, S.F. (2010). An electrostatically preferred lateral orientation of SNARE complex suggests novel mechanisms for driving membrane fusion. PLoS One *5*, e8900.

Hagn, F., Etzkorn, M., Raschle, T., and Wagner, G. (2013). Optimized phospholipid bilayer nanodiscs facilitate high-resolution structure determination of membrane proteins. J Am Chem Soc *135*, 1919-1925.

Hanson, P.I., Roth, R., Morisaki, H., Jahn, R., and Heuser, J.E. (1997). Structure and conformational changes in NSF and its membrane receptor complexes visualized by quick-freeze/deep-etch electron microscopy. Cell *90*, 523-535.

Haussinger, D., Huang, J.R., and Grzesiek, S. (2009). DOTA-M8: An extremely rigid, high-affinity lanthanide chelating tag for PCS NMR spectroscopy. J Am Chem Soc *131*, 14761-14767.

Hazzard, J., Sudhof, T.C., and Rizo, J. (1999). NMR analysis of the structure of synaptobrevin and of its interaction with syntaxin. J Biomol NMR *14*, 203-207.

Herculano-Houzel, S. (2012). The remarkable, yet not extraordinary, human brain as a scaled-up primate brain and its associated cost. Proc Natl Acad Sci U S A *109 Suppl 1*, 10661-10668.

Herrick, D.Z., Kuo, W., Huang, H., Schwieters, C.D., Ellena, J.F., and Cafiso, D.S. (2009). Solution and membrane-bound conformations of the tandem C2A and C2B domains of synaptotagmin 1: Evidence for bilayer bridging. J Mol Biol *390*, 913-923.

Herrick, D.Z., Sterbling, S., Rasch, K.A., Hinderliter, A., and Cafiso, D.S. (2006). Position of synaptotagmin I at the membrane interface: cooperative interactions of tandem C2 domains. Biochemistry *45*, 9668-9674.

Huntwork, S., and Littleton, J.T. (2007). A complexin fusion clamp regulates spontaneous neurotransmitter release and synaptic growth. Nat Neurosci *10*, 1235-1237.

Jahn, R., and Fasshauer, D. (2012). Molecular machines governing exocytosis of synaptic vesicles. Nature *490*, 201-207.

Jahn, R., and Scheller, R.H. (2006). SNAREs--engines for membrane fusion. Nat Rev Mol Cell Biol *7*, 631-643.

Johnson, B.A., and Blevins, R.A. (1994). NMR View: A computer program for the visualization and analysis of NMR data. J Biomol NMR *4*, 603-614.

Kesavan, J., Borisovska, M., and Bruns, D. (2007). v-SNARE actions during Ca(2+)-triggered exocytosis. Cell *131*, 351-363.

Kim, J.Y., Choi, B.K., Choi, M.G., Kim, S.A., Lai, Y., Shin, Y.K., and Lee, N.K. (2012). Solution single-vesicle assay reveals PIP2-mediated sequential actions of synaptotagmin-1 on SNAREs. EMBO J *31*, 2144-2155.

Klenchin, V.A., and Martin, T.F. (2000). Priming in exocytosis: attaining fusion-competence after vesicle docking. Biochimie *82*, 399-407.

Kohlhoff, K.J., Robustelli, P., Cavalli, A., Salvatella, X., and Vendruscolo, M. (2009). Fast and accurate predictions of protein NMR chemical shifts from interatomic distances. J Am Chem Soc *131*, 13894-13895.

Krishnakumar, S.S., Radoff, D.T., Kummel, D., Giraudo, C.G., Li, F., Khandan, L., Baguley, S.W., Coleman, J., Reinisch, K.M., Pincet, F., *et al.* (2011). A conformational switch in complexin is required for synaptotagmin to trigger synaptic fusion. Nat Struct Mol Biol *18*, 934-940.

Kuzmin, P.I., Zimmerberg, J., Chizmadzhev, Y.A., and Cohen, F.S. (2001). A quantitative model for membrane fusion based on low-energy intermediates. Proc Natl Acad Sci U S A *98*, 7235-7240.

Kweon, D.H., Kim, C.S., and Shin, Y.K. (2003). Regulation of neuronal SNARE assembly by the membrane. Nat Struct Biol *10*, 440-447.

Lai, A.L., Huang, H., Herrick, D.Z., Epp, N., and Cafiso, D.S. (2011). Synaptotagmin 1 and SNAREs form a complex that is structurally heterogeneous. J Mol Biol *405*, 696-706.

Landry, S.J., and Gierasch, L.M. (1991). The chaperonin GroEL binds a polypeptide in an alpha-helical conformation. Biochemistry *30*, 7359-7362.

Lee, H.K., Yang, Y., Su, Z., Hyeon, C., Lee, T.S., Lee, H.W., Kweon, D.H., Shin, Y.K., and Yoon, T.Y. (2010). Dynamic Ca2+-dependent stimulation of vesicle fusion by membrane-anchored synaptotagmin 1. Science *328*, 760-763.

Lee, J., Guan, Z., Akbergenova, Y., and Littleton, J.T. (2013). Genetic analysis of synaptotagmin C2 domain specificity in regulating spontaneous and evoked neurotransmitter release. J Neurosci *33*, 187-200.

Li, C., Ullrich, B., Zhang, J.Z., Anderson, R.G., Brose, N., and Sudhof, T.C. (1995). Ca(2+)-dependent and -independent activities of neural and non-neural synaptotagmins. Nature *375*, 594-599.

Li, F., Pincet, F., Perez, E., Eng, W.S., Melia, T.J., Rothman, J.E., and Tareste, D. (2007). Energetics and dynamics of SNAREpin folding across lipid bilayers. Nat Struct Mol Biol *14*, 890-896.

Liang, B., Dawidowski, D., Ellena, J.F., Tamm, L.K., and Cafiso, D.S. (2014). The SNARE motif of synaptobrevin exhibits an aqueous-interfacial partitioning that is modulated by membrane curvature. Biochemistry *53*, 1485-1494.

Lu, P., Bai, X.C., Ma, D., Xie, T., Yan, C., Sun, L., Yang, G., Zhao, Y., Zhou, R., Scheres, S.H., *et al.* (2014). Three-dimensional structure of human gamma-secretase. Nature *512*, 166-170.

Lu, X., Zhang, F., McNew, J.A., and Shin, Y.K. (2005). Membrane fusion induced by neuronal SNAREs transits through hemifusion. J Biol Chem *280*, 30538-30541.

Lynch, K.L., Gerona, R.R., Larsen, E.C., Marcia, R.F., Mitchell, J.C., and Martin, T.F. (2007). Synaptotagmin C2A loop 2 mediates Ca2+-dependent SNARE interactions essential for Ca2+-triggered vesicle exocytosis. Mol Biol Cell *18*, 4957-4968.

Ma, C., Li, W., Xu, Y., and Rizo, J. (2011). Munc13 mediates the transition from the closed syntaxin-Munc18 complex to the SNARE complex. Nat Struct Mol Biol *18*, 542-549.

Ma, C., Su, L., Seven, A.B., Xu, Y., and Rizo, J. (2013). Reconstitution of the vital functions of Munc18 and Munc13 in neurotransmitter release. Science *339*, 421-425.

MacKerell, A.D., Bashford, D., Bellott, M., Dunbrack, R.L., Evanseck, J.D., Field, M.J., Fischer, S., Gao, J., Guo, H., Ha, S., *et al.* (1998). All-atom empirical potential for molecular modeling and dynamics studies of proteins. J Phys Chem B *102*, 3586-3616.

Mackler, J.M., Drummond, J.A., Loewen, C.A., Robinson, I.M., and Reist, N.E. (2002). The C(2)B Ca(2+)-binding motif of synaptotagmin is required for synaptic transmission in vivo. Nature *418*, 340-344.

Mackler, J.M., and Reist, N.E. (2001). Mutations in the second C2 domain of synaptotagmin disrupt synaptic transmission at Drosophila neuromuscular junctions. J Comp Neurol *436*, 4-16.

Malsam, J., Parisotto, D., Bharat, T.A., Scheutzow, A., Krause, J.M., Briggs, J.A., and Sollner, T.H. (2012). Complexin arrests a pool of docked vesicles for fast Ca2+-dependent release. EMBO J *31*, 3270-3281.

Martens, S., Kozlov, M.M., and McMahon, H.T. (2007). How synaptotagmin promotes membrane fusion. Science *316*, 1205-1208.

Maximov, A., Pang, Z.P., Tervo, D.G., and Sudhof, T.C. (2007). Monitoring synaptic transmission in primary neuronal cultures using local extracellular stimulation. J Neurosci Methods *161*, 75-87.

Maximov, A., Tang, J., Yang, X., Pang, Z.P., and Sudhof, T.C. (2009). Complexin controls the force transfer from SNARE complexes to membranes in fusion. Science *323*, 516-521.

McNew, J.A., Weber, T., Engelman, D.M., Sollner, T.H., and Rothman, J.E. (1999). The length of the flexible SNAREpin juxtamembrane region is a critical determinant of SNARE-dependent fusion. Mol Cell *4*, 415-421.

Meinrenken, C.J., Borst, J.G., and Sakmann, B. (2002). Calcium secretion coupling at calyx of held governed by nonuniform channel-vesicle topography. J Neurosci *22*, 1648-1667.

Mishima, T., Fujiwara, T., Sanada, M., Kofuji, T., Kanai-Azuma, M., and Akagawa, K. (2014). Syntaxin 1B, but not syntaxin 1A, is necessary for the regulation of synaptic vesicle exocytosis and of the readily releasable pool at central synapses. PLoS One *9*, e90004.

Misura, K.M., Scheller, R.H., and Weis, W.I. (2000). Three-dimensional structure of the neuronal-Sec1-syntaxin 1a complex. Nature *404*, 355-362.

Misura, K.M., Scheller, R.H., and Weis, W.I. (2001). Self-association of the H3 region of syntaxin 1A. Implications for intermediates in SNARE complex assembly. J Biol Chem *276*, 13273-13282.

Mittermaier, A.K., and Kay, L.E. (2009). Observing biological dynamics at atomic resolution using NMR. Trends Biochem Sci *34*, 601-611.

Mohrmann, R., de Wit, H., Verhage, M., Neher, E., and Sorensen, J.B. (2010). Fast vesicle fusion in living cells requires at least three SNARE complexes. Science *330*, 502-505.

Muhandiram, D.R., and Kay, L.E. (1994). Gradient-Enhanced Triple-Resonance 3-Dimensional Nmr Experiments with Improved Sensitivity. J Magn Reson Ser B *103*, 203-216.

Nicholson, K.L., Munson, M., Miller, R.B., Filip, T.J., Fairman, R., and Hughson, F.M. (1998). Regulation of SNARE complex assembly by an N-terminal domain of the t-SNARE Sso1p. Nat Struct Biol *5*, 793-802.

Nishiki, T., and Augustine, G.J. (2004). Dual roles of the C2B domain of synaptotagmin I in synchronizing Ca2+-dependent neurotransmitter release. J Neurosci *24*, 8542-8550.

Otting, G. (2010). Protein NMR using paramagnetic ions. Annu Rev Biophys *39*, 387-405.

Pang, Z.P., Cao, P., Xu, W., and Sudhof, T.C. (2010). Calmodulin controls synaptic strength via presynaptic activation of calmodulin kinase II. J Neurosci *30*, 4132-4142.

Pang, Z.P., Shin, O.H., Meyer, A.C., Rosenmund, C., and Sudhof, T.C. (2006). A gain-of-function mutation in synaptotagmin-1 reveals a critical role of Ca2+-dependent soluble N-ethylmaleimide-sensitive factor attachment protein receptor complex binding in synaptic exocytosis. J Neurosci *26*, 12556-12565.

Parisotto, D., Malsam, J., Scheutzow, A., Krause, J.M., and Sollner, T.H. (2012). SNAREpin assembly by Munc18-1 requires previous vesicle docking by synaptotagmin 1. J Biol Chem *287*, 31041-31049.

Peters, F., Maestre-Martinez, M., Leonov, A., Kovacic, L., Becker, S., Boelens, R., and Griesinger, C. (2011). Cys-Ph-TAHA: a lanthanide binding tag for RDC and PCS enhanced protein NMR. J Biomol NMR *51*, 329-337.

Phillips, J.C., Braun, R., Wang, W., Gumbart, J., Tajkhorshid, E., Villa, E., Chipot, C., Skeel, R.D., Kale, L., and Schulten, K. (2005). Scalable molecular dynamics with NAMD. J Comput Chem *26*, 1781-1802.

Piana, S., and Laio, A. (2007). A bias-exchange approach to protein folding. J Phys Chem B *111*, 4553-4559.

Pobbati, A.V., Stein, A., and Fasshauer, D. (2006). N- to C-terminal SNARE complex assembly promotes rapid membrane fusion. Science *313*, 673-676.

Poirier, M.A., Xiao, W., Macosko, J.C., Chan, C., Shin, Y.K., and Bennett, M.K. (1998). The synaptic SNARE complex is a parallel four-stranded helical bundle. Nat Struct Biol *5*, 765-769.

Pronk, S., Pall, S., Schulz, R., Larsson, P., Bjelkmar, P., Apostolov, R., Shirts, M.R., Smith, J.C., Kasson, P.M., van der Spoel, D., *et al.* (2013). GROMACS 4.5: a high-throughput and highly parallel open source molecular simulation toolkit. Bioinformatics *29*, 845-854.

Radhakrishnan, A., Stein, A., Jahn, R., and Fasshauer, D. (2009). The Ca2+ affinity of synaptotagmin 1 is markedly increased by a specific interaction of its C2B domain with phosphatidylinositol 4,5-bisphosphate. J Biol Chem *284*, 25749-25760.

Raschle, T., Hiller, S., Yu, T.Y., Rice, A.J., Walz, T., and Wagner, G. (2009). Structural and functional characterization of the integral membrane protein VDAC-1 in lipid bilayer nanodiscs. J Am Chem Soc *131*, 17777-17779.

Reim, K., Mansour, M., Varoqueaux, F., McMahon, H.T., Sudhof, T.C., Brose, N., and Rosenmund, C. (2001). Complexins regulate a late step in Ca2+-dependent neurotransmitter release. Cell *104*, 71-81.

Rhee, J.S., Li, L.Y., Shin, O.H., Rah, J.C., Rizo, J., Sudhof, T.C., and Rosenmund, C. (2005). Augmenting neurotransmitter release by enhancing the apparent Ca2+ affinity of synaptotagmin 1. Proc Natl Acad Sci U S A *102*, 18664-18669.

Ribrault, C., Sekimoto, K., and Triller, A. (2011). From the stochasticity of molecular processes to the variability of synaptic transmission. Nat Rev Neurosci *12*, 375-387.

Richens, J.L., Lunt, E.A., Sanger, D., McKenzie, G., and O'Shea, P. (2009). Avoiding nonspecific interactions in studies of the plasma proteome: practical solutions to prevention of nonspecific interactions for label-free detection of low-abundance plasma proteins. J Proteome Res *8*, 5103-5110.

Rickman, C., Archer, D.A., Meunier, F.A., Craxton, M., Fukuda, M., Burgoyne, R.D., and Davletov, B. (2004). Synaptotagmin interaction with the syntaxin/SNAP-25 dimer is mediated by an evolutionarily conserved motif and is sensitive to inositol hexakisphosphate. J Biol Chem *279*, 12574-12579.

Rickman, C., Jimenez, J.L., Graham, M.E., Archer, D.A., Soloviev, M., Burgoyne, R.D., and Davletov, B. (2006). Conserved prefusion protein assembly in regulated exocytosis. Mol Biol Cell *17*, 283-294.

Rigaud, J.L., Pitard, B., and Levy, D. (1995). Reconstitution of membrane proteins into liposomes: application to energy-transducing membrane proteins. Biochim Biophys Acta *1231*, 223-246.

Rizo, J., Chen, X., and Arac, D. (2006). Unraveling the mechanisms of synaptotagmin and SNARE function in neurotransmitter release. Trends Cell Biol *16*, 339-350.

Rizo, J., and Rosenmund, C. (2008). Synaptic vesicle fusion. Nat Struct Mol Biol *15*, 665-674.

Rizo, J., and Sudhof, T.C. (2012). The membrane fusion enigma: SNAREs, Sec1/Munc18 proteins, and their accomplices--guilty as charged? Annu Rev Cell Dev Biol *28*, 279-308.

Robinson, I.M., Ranjan, R., and Schwarz, T.L. (2002). Synaptotagmins I and IV promote transmitter release independently of Ca(2+) binding in the C(2)A domain. Nature *418*, 336-340.

Roux, B., and Weare, J. (2013). On the statistical equivalence of restrained-ensemble simulations with the maximum entropy method. J Chem Phys *138*, 084107.

Ruschak, A.M., and Kay, L.E. (2010). Methyl groups as probes of supra-molecular structure, dynamics and function. J Biomol NMR *46*, 75-87.

Sabatini, B.L., and Regehr, W.G. (1996). Timing of neurotransmission at fast synapses in the mammalian brain. Nature *384*, 170-172.

Satzler, K., Sohl, L.F., Bollmann, J.H., Borst, J.G., Frotscher, M., Sakmann, B., and Lubke, J.H. (2002). Three-dimensional reconstruction of a calyx of Held and its postsynaptic principal neuron in the medial nucleus of the trapezoid body. J Neurosci *22*, 10567-10579.

Schaub, J.R., Lu, X., Doneske, B., Shin, Y.K., and McNew, J.A. (2006). Hemifusion arrest by complexin is relieved by Ca2+-synaptotagmin I. Nat Struct Mol Biol *13*, 748-750.

Schikorski, T., and Stevens, C.F. (2001). Morphological correlates of functionally defined synaptic vesicle populations. Nat Neurosci *4*, 391-395.

Schilder, J., Lohr, F., Schwalbe, H., and Ubbink, M. (2014). The cytochrome c peroxidase and cytochrome c encounter complex: the other side of the story. FEBS Lett *588*, 1873-1878.

Schmitz, C., and Bonvin, A.M. (2011). Protein-protein HADDocking using exclusively pseudocontact shifts. J Biomol NMR *50*, 263-266.

Schmitz, C., Stanton-Cook, M.J., Su, X.C., Otting, G., and Huber, T. (2008). Numbat: an interactive software tool for fitting Deltachi-tensors to molecular coordinates using pseudocontact shifts. J Biomol NMR *41*, 179-189.

Schoch, S., Deak, F., Konigstorfer, A., Mozhayeva, M., Sara, Y., Sudhof, T.C., and Kavalali, E.T. (2001). SNARE function analyzed in synaptobrevin/VAMP knockout mice. Science *294*, 1117-1122.

Seven, A.B., Brewer, K.D., Shi, L., Jiang, Q.X., and Rizo, J. (2013). Prevalent mechanism of membrane bridging by synaptotagmin-1. Proc Natl Acad Sci U S A *110*, E3243-3252.

Shao, X., Fernandez, I., Sudhof, T.C., and Rizo, J. (1998). Solution structures of the Ca2+-free and Ca2+-bound C2A domain of synaptotagmin I: does Ca2+ induce a conformational change? Biochemistry *37*, 16106-16115.

Shen, J., Tareste, D.C., Paumet, F., Rothman, J.E., and Melia, T.J. (2007). Selective activation of cognate SNAREpins by Sec1/Munc18 proteins. Cell *128*, 183-195.

Sheng, Z.H., Rettig, J., Takahashi, M., and Catterall, W.A. (1994). Identification of a syntaxin-binding site on N-type calcium channels. Neuron *13*, 1303-1313.

Shenkarev, Z.O., Lyukmanova, E.N., Solozhenkin, O.I., Gagnidze, I.E., Nekrasova, O.V., Chupin, V.V., Tagaev, A.A., Yakimenko, Z.A., Ovchinnikova, T.V., Kirpichnikov, M.P., *et al.* (2009). Lipid-protein nanodiscs: possible application in

high-resolution NMR investigations of membrane proteins and membrane-active peptides. Biochemistry (Mosc) *74*, 756-765.

Shi, L., Shen, Q.T., Kiel, A., Wang, J., Wang, H.W., Melia, T.J., Rothman, J.E., and Pincet, F. (2012). SNARE proteins: one to fuse and three to keep the nascent fusion pore open. Science *335*, 1355-1359.

Shin, O.H., Xu, J., Rizo, J., and Sudhof, T.C. (2009). Differential but convergent functions of Ca2+ binding to synaptotagmin-1 C2 domains mediate neurotransmitter release. Proc Natl Acad Sci U S A *106*, 16469-16474.

Shishmarev, D., and Otting, G. (2013). How reliable are pseudocontact shifts induced in proteins and ligands by mobile paramagnetic metal tags? A modelling study. J Biomol NMR *56*, 203-216.

Slepnev, V.I., and De Camilli, P. (2000). Accessory factors in clathrin-dependent synaptic vesicle endocytosis. Nat Rev Neurosci *1*, 161-172.

Snead, D., Wragg, R.T., Dittman, J.S., and Eliezer, D. (2014). Membrane curvature sensing by the C-terminal domain of complexin. Nat Commun *5*, 4955.

Sorensen, J.B., Wiederhold, K., Muller, E.M., Milosevic, I., Nagy, G., de Groot, B.L., Grubmuller, H., and Fasshauer, D. (2006). Sequential N- to C-terminal SNARE complex assembly drives priming and fusion of secretory vesicles. EMBO J *25*, 955-966.

Stadler, H., and Tsukita, S. (1984). Synaptic vesicles contain an ATP-dependent proton pump and show 'knob-like' protrusions on their surface. EMBO J *3*, 3333-3337.

Stein, A., Weber, G., Wahl, M.C., and Jahn, R. (2009). Helical extension of the neuronal SNARE complex into the membrane. Nature *460*, 525-528.

Su, X.C., Liang, H., Loscha, K.V., and Otting, G. (2009). [Ln(DPA)(3)](3-) is a convenient paramagnetic shift reagent for protein NMR studies. J Am Chem Soc *131*, 10352-10353.

Sudhof, T.C. (2004). The synaptic vesicle cycle. Annu Rev Neurosci *27*, 509-547.

Sudhof, T.C., and Rothman, J.E. (2009). Membrane fusion: grappling with SNARE and SM proteins. Science *323*, 474-477.

Sutton, R.B., Davletov, B.A., Berghuis, A.M., Sudhof, T.C., and Sprang, S.R. (1995). Structure of the first C2 domain of synaptotagmin I: a novel Ca2+/phospholipid-binding fold. Cell *80*, 929-938.

Sutton, R.B., Ernst, J.A., and Brunger, A.T. (1999). Crystal structure of the cytosolic C2A-C2B domains of synaptotagmin III. Implications for Ca(+2)-independent snare complex interaction. J Cell Biol *147*, 589-598.

Sutton, R.B., Fasshauer, D., Jahn, R., and Brunger, A.T. (1998). Crystal structure of a SNARE complex involved in synaptic exocytosis at 2.4 A resolution. Nature *395*, 347-353.

Takamori, S., Holt, M., Stenius, K., Lemke, E.A., Gronborg, M., Riedel, D., Urlaub, H., Schenck, S., Brugger, B., Ringler, P., *et al.* (2006). Molecular anatomy of a trafficking organelle. Cell *127*, 831-846.

Tang, J., Maximov, A., Shin, O.H., Dai, H., Rizo, J., and Sudhof, T.C. (2006). A complexin/synaptotagmin 1 switch controls fast synaptic vesicle exocytosis. Cell *126*, 1175-1187.

Thayer, S.A., Usachev, Y.M., and Pottorf, W.J. (2002). Modulating Ca2+ clearance from neurons. Front Biosci *7*, d1255-1279.

Tribello, G.A., Bonomi, M., Branduardi, D., Camilloni, C., and Bussi, G. (2014). PLUMED 2: New feathers for an old bird. Computer Physics Communications *185*, 604-613.

Trimbuch, T., Xu, J., Flaherty, D., Tomchick, D.R., Rizo, J., and Rosenmund, C. (2014). Re-examining how complexin inhibits neurotransmitter release. Elife *3*, e02391.

Ubach, J., Lao, Y., Fernandez, I., Arac, D., Sudhof, T.C., and Rizo, J. (2001). The C2B domain of synaptotagmin I is a Ca2+-binding module. Biochemistry *40*, 5854-5860.

Ubach, J., Zhang, X., Shao, X., Sudhof, T.C., and Rizo, J. (1998). Ca2+ binding to synaptotagmin: how many Ca2+ ions bind to the tip of a C2-domain? EMBO J *17*, 3921-3930.

van den Bogaart, G., Holt, M.G., Bunt, G., Riedel, D., Wouters, F.S., and Jahn, R. (2010). One SNARE complex is sufficient for membrane fusion. Nat Struct Mol Biol *17*, 358-364.

Varadi, M., Kosol, S., Lebrun, P., Valentini, E., Blackledge, M., Dunker, A.K., Felli, I.C., Forman-Kay, J.D., Kriwacki, R.W., Pierattelli, R., *et al.* (2014). pE-DB: a database of structural ensembles of intrinsically disordered and of unfolded proteins. Nucleic Acids Res *42*, D326-335.

Vrljic, M., Strop, P., Ernst, J.A., Sutton, R.B., Chu, S., and Brunger, A.T. (2010). Molecular mechanism of the synaptotagmin-SNARE interaction in Ca2+-triggered vesicle fusion. Nat Struct Mol Biol *17*, 325-331.

Walter, A.M., Wiederhold, K., Bruns, D., Fasshauer, D., and Sorensen, J.B. (2010). Synaptobrevin N-terminally bound to syntaxin-SNAP-25 defines the primed vesicle state in regulated exocytosis. J Cell Biol *188*, 401-413.

Weber, T., Zemelman, B.V., McNew, J.A., Westermann, B., Gmachl, M., Parlati, F., Sollner, T.H., and Rothman, J.E. (1998). SNAREpins: minimal machinery for membrane fusion. Cell *92*, 759-772.

Weninger, K., Bowen, M.E., Choi, U.B., Chu, S., and Brunger, A.T. (2008). Accessory proteins stabilize the acceptor complex for synaptobrevin, the 1:1 syntaxin/SNAP-25 complex. Structure *16*, 308-320.

Wickner, W., and Schekman, R. (2008). Membrane fusion. Nat Struct Mol Biol *15*, 658-664.

Xu, J., Bacaj, T., Zhou, A., Tomchick, D.R., Sudhof, T.C., and Rizo, J. (2014). Structure and Ca(2)(+)-binding properties of the tandem C(2) domains of E-Syt2. Structure *22*, 269-280.

Xu, J., Brewer, K.D., Perez-Castillejos, R., and Rizo, J. (2013). Subtle Interplay between synaptotagmin and complexin binding to the SNARE complex. J Mol Biol *425*, 3461-3475.

Xu, J., Mashimo, T., and Sudhof, T.C. (2007). Synaptotagmin-1, -2, and -9: Ca(2+) sensors for fast release that specify distinct presynaptic properties in subsets of neurons. Neuron *54*, 567-581.

Xu, J., Pang, Z.P., Shin, O.H., and Sudhof, T.C. (2009). Synaptotagmin-1 functions as a Ca2+ sensor for spontaneous release. Nat Neurosci *12*, 759-766.

Xu, Y., Seven, A.B., Su, L., Jiang, Q.X., and Rizo, J. (2011). Membrane bridging and hemifusion by denaturated Munc18. PLoS One *6*, e22012.

Xu, Y., Su, L., and Rizo, J. (2010). Binding of Munc18-1 to synaptobrevin and to the SNARE four-helix bundle. Biochemistry *49*, 1568-1576.

Xue, M., Craig, T.K., Xu, J., Chao, H.T., Rizo, J., and Rosenmund, C. (2010). Binding of the complexin N terminus to the SNARE complex potentiates synaptic-vesicle fusogenicity. Nat Struct Mol Biol *17*, 568-575.

Xue, M., Ma, C., Craig, T.K., Rosenmund, C., and Rizo, J. (2008). The Janus-faced nature of the C(2)B domain is fundamental for synaptotagmin-1 function. Nat Struct Mol Biol *15*, 1160-1168.

Xue, M., Reim, K., Chen, X., Chao, H.T., Deng, H., Rizo, J., Brose, N., and Rosenmund, C. (2007). Distinct domains of complexin I differentially regulate neurotransmitter release. Nat Struct Mol Biol *14*, 949-958.

Yoon, T.Y., Okumus, B., Zhang, F., Shin, Y.K., and Ha, T. (2006). Multiple intermediates in SNARE-induced membrane fusion. Proc Natl Acad Sci U S A *103*, 19731-19736.

Zhang, X., Kim-Miller, M.J., Fukuda, M., Kowalchyk, J.A., and Martin, T.F. (2002). Ca2+-dependent synaptotagmin binding to SNAP-25 is essential for Ca2+-triggered exocytosis. Neuron *34*, 599-611.

Zhang, X., Rizo, J., and Sudhof, T.C. (1998). Mechanism of phospholipid binding by the C2A-domain of synaptotagmin I. Biochemistry *37*, 12395-12403.

Zhang, Y., and Cremer, P.S. (2006). Interactions between macromolecules and ions: The Hofmeister series. Curr Opin Chem Biol *10*, 658-663.

Zhou, A., Brewer, K.D., and Rizo, J. (2013a). Analysis of SNARE complex/synaptotagmin-1 interactions by one-dimensional NMR spectroscopy. Biochemistry *52*, 3446-3456.

Zhou, P., Bacaj, T., Yang, X., Pang, Z.P., and Sudhof, T.C. (2013b). Lipid-anchored SNAREs lacking transmembrane regions fully support membrane fusion during neurotransmitter release. Neuron *80*, 470-483.